ON THE CHARACTERIZATION OF ENGINEERED ELASTOMERS AT HIGH STRAIN RATES

MUHAMMAD SALMAN CHAUDHRY

A THESIS SUBMITTED TO THE FACULTY OF GRADUATE STUDEIS IN
PARTIAL FULLFILLMENT OF THE REQUIREMENTS FOR THE DEGREE OF
MASTER OF SCIENCE

GRADUATE PROGRAM IN EARTH AND SPACE SCIENCE
YORK UNIVERSITY
TORONTO, ONTARIO

August 2016

Abstract

The main objective of this research was to develop a methodology for the characterization and modelling of elastomers that were subject to high-strain rate. Four aspects of the problem were accordingly examined. The first aspect of the study was dedicated to the comparison of constitutive equations to numerically model elastomers. The second aspect revolved around the testing of elastomers under dynamic loading. For this purpose, a Kolsky Bar was designed and constructed to test soft, flexible materials. The third aspect of the work dealt with the numerical modelling of the developed testing apparatus. Finite element methodology was used to optimize the testing parameters and validate the modified Kolsky Bar apparatus. Finally, the methodology developed to characterize the response of elastomers under high-strain rate loadings was employed to study two unique engineering materials. The developed approach should help engineers and designers in developing new systems in dynamic application with elastomer.

Acknowledgements

I extend my appreciation and gratitude to Dr. A. Czekanski for his expert advice, technical guidance and financial assistance throughout the course of my research. I also wish to acknowledge the comprehensive assistance of Dr. G. Zhu, Dr. G. Vukovich and Dr. M. Al-Dojayli. I would also like to pay special thanks to the members of the Innovative Design and Engineering Analysis Laboratory for their friendship and help during the undertaking of the current study.

The financial support of the Natural Sciences and Engineering Research Council of Canada (NSERC), Quanser and York University is gratefully acknowledged.

Finally, I would like to thank my maa, dad and friends (Ali Shahid, Sadoon Butt) for their continual and unconditional support and encouragement throughout my educational endeavours.

Table of Contents

List of Tables

List of Figures

Notations

Area of the bar’s cross section,	A_b
Ares of the sample cross section,	A_s
Bulk modulus,	K_0
Cauchy stress,	σ
Critical damping,	ξ
Density,	ρ
Diameter of bar,	D_b
Diameter of sample,	D_s
Elastic volume ratio,	J^{el}
Elastic wave speed in metallic bar,	C_b
Engineering strain,	ε
Gruneisen gamma,	Γ_0
Hydrostatic pressure,	p
Internal energy per unit volume,	E_m
Invariant of Cauchy-green deformation tensor,	I_i
Length of bar,	L_b
Length of specimen,	L_s
Material parameters,	C_{ij}
Principal stretches,	λ_i
Rate of strain,	$\dot{\varepsilon}$
Shear modulus,	μ_0
Strain energy density function,	Ψ
Velocity.	V
Yield stress,	$\bar{\sigma}$

Chapter 1 Introduction and Justification

Summary: In this chapter we define the problem, justify the undertaking of the study and outline the method of approach adopted in achieving the set objectives. Furthermore, we provide a summary of the layout of the thesis.

1.1 Mechanical Response of Elastomers

Elastomers, also known as engineered rubbers, are categorized as soft materials having the ability to withstand high elastic deformations by absorbing and dissipating energy. They are attributed to the development of a broad range of new applications in automotive, biological and aerospace industries and the global revenue is forecasted to rise well above US$56 billion by 2020 [1]. The damping property of elastomers makes them a remarkable choice to be used in dynamic applications such as shock absorbers, engine mounts and automobile tires. Fig 1.1 illustrates several dynamic applications of elastomers.

To guarantee reliability, integrity and safety of new engineering applications, the understating of the material's response under all regimes of strain rate is critical. For example, when conducting crashworthiness simulations, engineers are required to determine the response of the material subjected to strain rates experienced in the collision event. Moreover, experimental characterization provides critical data needed to implement constitutive material models in finite element simulations.

The mechanical response of elastomers is a result of highly twisted, coiled and randomly oriented molecular chains. Under a tensile load, these chains are untwisted and partially straightened, returning to their original configuration upon removal of the load. Due to this behaviour of molecular crosslinks on the microscopic level, elastomers exhibit highly non-linear stress-strain behaviour at the macroscopic level, with an ability to undergo deformations of up to 100 to 700 percent. The behaviour of elastomer is a result of a complex connection between the time of loading and its associated deformation mechanism which is far from being understood, especially under short time dynamics. For such dynamic applications in the automobile industry, elastomers are engineered to enhance energy absorption properties to design components like bumpers, air bags and shock absorbers. In a collision, a vehicle can experience strain rates of 100 to 10,000 s^{-1}. Reported mechanical properties in books are obtained by quasi-static testing, which are insufficient to guarantee a products reliability under impact.

Therefore, the objective of this thesis is to bridge the gap for designers by developing and conducting a comprehensive research program to study the behaviour of elastomers under quasi-static and dynamic loading of strain rates up to 10,000 s^{-1}. This would help to better understand the response of elastomeric components that are to be designed for a multi-body application.

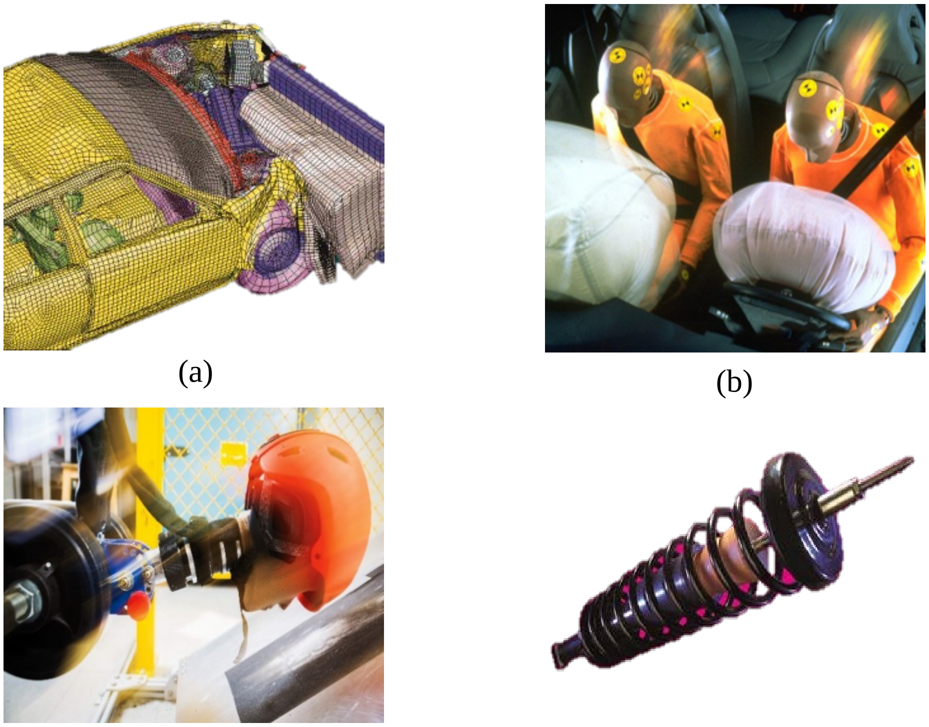

(a) (b) (c) (d)

Fig. 1.1 : Examples of dynamic applications of elastomers: (a) vehicle crashworthiness for frontal impact into a soft offset barrier [2], (b) anthropomorphic test device in simulated vehicle impact [3], (c) head protection gear [4], and (d) polyurethane elastomer in automotive shock absorbers [5].

1.2 Justification of the Study

Ensuring the integrity of elastomer engineering, the application is greatly dependent upon how well the response behaviour of this class of material is understood under various loading constraints. Very often the testing and characterization at varying levels and environments require different test setups, which is a very time consuming and expensive process. However, when designing for dynamic applications, neglecting the strain rate effect on the response and performance of elastomers can result as failure of components before completing expected duty cycle.

Elastomers are modelled as hyper elastic materials that require multi-axial modes of deformation data to generate material parameters. Static constitutive equations used to simulate the behaviour of elastomers do not accurately predict the material's response under impact. The material needs to be tested at various rates of interest to generate parameters for strain rate sensitive constitutive models.

Typically, quasi-static tests are carried out in a commercial load frame with a closed-loop arrangement and controllable loading conditions. However, high strain rates of loading experienced in collision related events cannot be generated using commercially available testing equipment hence specialized instruments are required.

Such testing apparatus that is able to achieve moderate to high strain rates was developed by Kolsky [6]. In this apparatus, the deformation can be observed with sensors like strain gauges, making it a controllable and qualitative method of testing. However, a Kolsky bar should be carefully designed as it is in an open loop arrangement, and the specimen response cannot be ignored, especially when testing softer, low impedance materials. For this purpose, no set standards have been developed. Moreover, to satisfy valid testing conditions of the apparatus, some modifications need to be made and the specimen geometry needs to be optimized for elastomer testing.

1.3 Research Objectives

This thesis is therefore devoted to the development, implementation and application of a comprehensive methodology for testing and modelling elastomers at moderate to intermediate and high strain rates. Primarily, our current efforts were devoted to:

(i) Implementing and conducting a performance comparison study of quasi-static analytical constitutive models,

(ii) Developing high strain rate testing equipment for elastomers and conducting quasi-static and dynamic testing at different strain rates to provide input data for material characterization,

(iii) Validating the experimental design and selecting appropriate testing parameters for the developed high strain rate testing equipment using finite element analysis, and

(iv) Applying the developed methodology to understand the effect of strain rate on the mechanical performance of newly engineered elastomers fabricated from modern manufacturing techniques.

1.4 Method of Approach

Fig. 1.2 shows a scheme of the approach adopted to achieve the above stated objectives. The testing apparatus (called the Kolsky bar) was designed and developed based upon the elastomer's mechanical properties. We employed finite element analysis (FEA) to (i) verify and *calibrate the testing apparatus,* (ii) investigate the *pulse shaping technique* in Kolsky apparatus, and (iii) analyse the *specimen geometry effect* on the accurate testing procedure of the material. High strain rate response measured from the testing procedure was then used to compare the performance of various *constitutive models* available in commercial FEA packages. The most important aspect of this part of study was to analyse and compare the performance of material models when there is limited test data. Based on this approach, the response of elastomers was characterized and subjected to quasi-static and high strain rates of loading. The test data constitutive model parameters were evaluated using curve fitting and then modelled in finite element methodology (FEM). Last but not least, the outcomes of the presented testing methodology were applied to evaluate the response of engineered elastomeric Nano-composites. In another application, the strain rate effect on the mechanical performance of elastomers fabricated from fused deposition modelling technique in 3-D printing was evaluated and analysed.

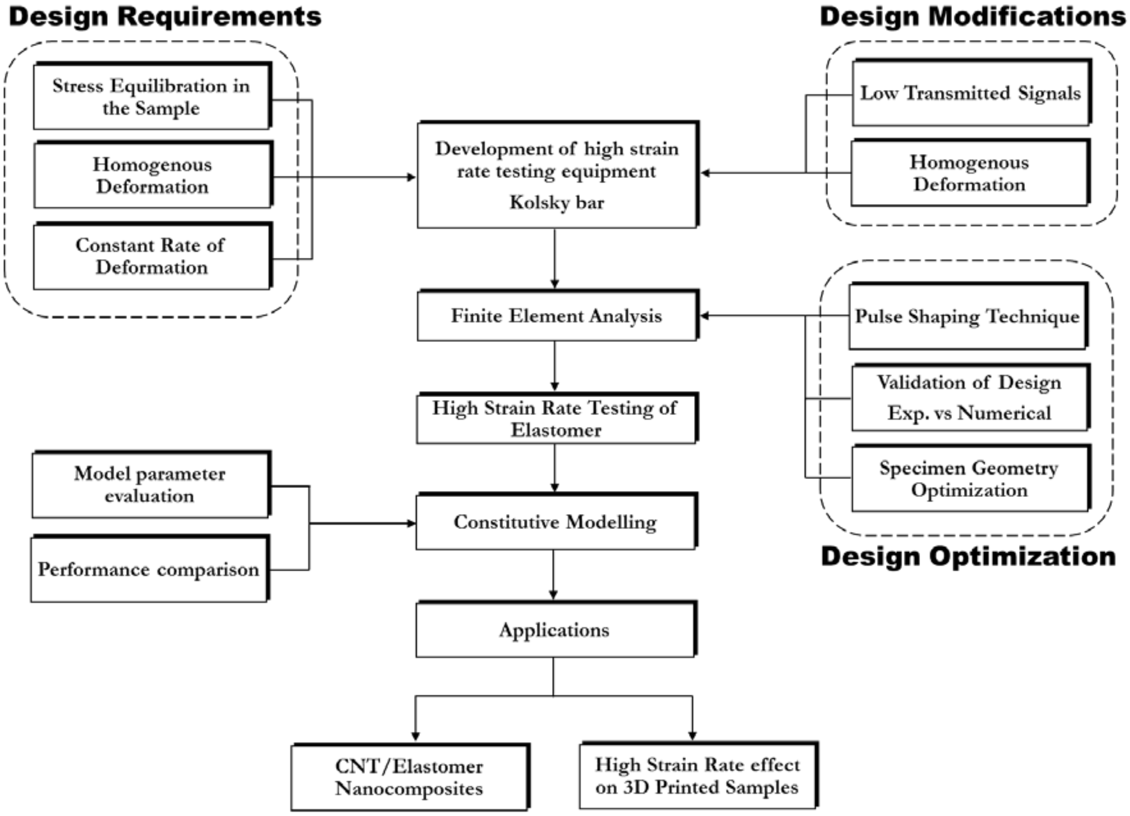

Fig. 1.2 A schematic of method of the approach.

1.5 Layout of Thesis

This thesis is divided into seven chapters in total. Following this brief introduction of the topic, **Chapter 2** provides a critical review of the relevant work to high strain rate characterization of elastomers addressing the following: static and dynamic constitutive models, conventional high strain rate testing methods and critical testing assumptions and limitations. **Chapter 3** summarises the main quasi-static constitutive models available in commercial FEA software and implementation of strain rate dependant models to capture the effect of rate of loading. In **Chapter 4**, we address the major limitations and challenges that must be overcome when testing low impedance materials such as elastomers in a valid Kolsky bar experiment. Furthermore, a modified version of a Kolsky bar to test elastomers is presented in this chapter. In **Chapter 5**, we address the numerical modelling technique that can be used to model and calibrate the developed high strain rate testing apparatus. This Chapter also provides a detailed account of the approach adopted to optimize the specimen geometry selection and analyse the pulse shaping techniques. In **Chapter 6**, the outcomes of the presented methodology are applied to various case studies relating to the development of the newly engineered elastomeric components for high strain rate applications. In **Chapter 7**, we conclude the work and identify the original contribution of the thesis, and outline suggestions for related future work.

Chapter 2 Literature Review

Summary: This literature review is divided into three main sections. The first section deals with the traditional hyperelastic constitutive models. The second section is devoted to the relevant literature related to the finite element analysis (FEA) approach. The third section covers the review of the conventional method and related limitations and requirements needed to address the characterisation of elastomers at high strain rates.

2.1 Mechanical Characterization of Elastomer Behaviour

2.1.1 Elastomer as Hyperelastic Material

Soft and flexible polymers such as elastomers exhibit a highly non-linear stress strain behaviour, with extension values ranging from 700% to 1000%. The typical elastomers are virtually incompressible or nearly incompressible in nature. Unlike elastic materials, Hooke's law cannot be used and the values for Young's modulus cannot be assigned when describing the response rate of this polymer. The differences between an elastic response and the highly non-linear stress strain characteristic exhibited by elastomers are represented in Fig. 2.1.

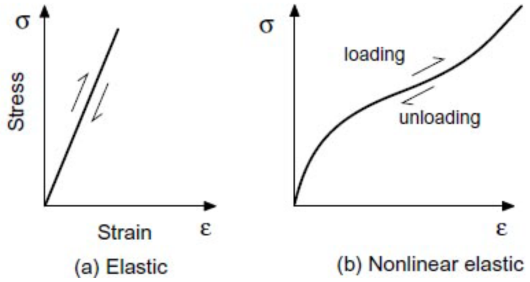

(a) Elastic (b) Nonlinear elastic

Fig. 2.1 Typical elastic and nonlinear elastic stress strain curves.

Models of hyperelastic materials are used to analyse the ability of elastomers to experience large elastic strains from small forces without losing their original properties. Similar to elastomers, hyperelastic materials exhibit nonlinear loading and deformation patterns. Focus is directed towards the development of theoretical models to predict the stress strain relationship for hyperelastic materials, which can be divided into two broad categories.

On one hand, the phenomenological approach utilizes continuum mechanics to provide a characterizing framework for elastomer behaviour without taking the microscopic structure into account. On the other hand, the statistical mechanical approach utilizes kinetic theory to derive the response from an idealized model of the elastomer structure. This approach assumes the unstrained structure of the elastomer to be highly amorphous and, thus, high in entropy. During deformation, the elastic forces within the material arise due to the change in entropy. However, this approach is used for the assumed statistical distribution of the length and structure of molecular chains, and appears to be adequate only for moderate strains (up to 50%) [7].

In literature, much attention seems to be given to the development of phenomenological models, which are the focus of this study. In this approach, the structure of the elastomer is assumed to be composed of long molecular chains orientated together randomly in an unformed state. During deformation, the molecular chains orientate in the direction of the applied stretch. The strain energy stored during deformation is assumed to be isotropic during the process and is fundamental to the characterization of elastomers [8].

The constitutive equations for the hyperelastic model are derived from strain energy functions, which are expressed either as a function of strain invariants I_1, I_2, I_3, or in terms of the principal stretches $\lambda_1, \lambda_2, \lambda_3$ of the strain tensor. The strain energy potential defines the strain energy stored in each unit of reference volume as a function of strain at that point in the material. One of the very first and simplest models, the two-parameter phenomenological model was proposed by Mooney (1940), [9] is based on the assumption of a linear relationship between stress and strain during simple shear deformation. In 1944, Treloar [10] gave a demonstration of hyperelastic stress strain behaviour using the statistical mechanics treatments of rubber elasticity, known as the Neo-Hookean model. Based on the one-dimensional theory of long crosslinked molecules, it relates to the geometric softening of rubber due to large deformations. However, this model does not consider the progressive hardening of the material close to failure. In 1948, Rivlin modified the Mooney model to obtain a strain energy function, represented by the sum of the first and second deviatoric principal invariants. The model was known as the Mooney-Rivlin model [11] [12]. Yeoh (1993) proposed a strain energy function of a third-degree polynomial of the first invariant of the right Cauchy-Green tensor [13].

The stretch-based phenomenological model developed by Ogden (1972) expresses the strain energy function in terms of principal stretches for incompressible materials [14]. This model has shown excellent compatibility with Treloar's experimental test data on natural rubber up to high strains. However, the parameter identification is complicated and the application of the model is more computationally extensive [15]. Another stretch ratio-based model is Arruda-Boyce, which is developed from a representative volume element comprising a three-dimensional array of long-chained molecules [16].

For a specific material, the coefficients of the strain energy functions are empirically determined by conducting static (i) uniaxial extension and compression, (ii) equi-biaxial extension, and (iii) planar tension test data. However, the performance of these constitutive models largely depend on the number of different types of test data available and on the working strain regime. Therefore, Chapter 3 deals with the comparison of the available constitutive models as it is much needed to ensure the model does not fail at the desired strains and is compatible with the test data.

2.2 Mechanical Testing of Elastomers at High Strain Rates

2.2.1 Background

In dynamic applications, elastomeric specimens are subjected to loading at varying rates, and the material responds accordingly. The hyperelastic material models discussed above do not consider the strain rate dependency of elastomers. Strain rates up to 10,000 s^{-1} are experienced in impact events, such as automobile crash. To ensure the reliability and quality of the product in high-rate loading applications, there is a need to characterize the material undergoing dynamic loading.

In strain rate regimes between 100 /s and 10,000 /s, the most commonly used testing apparatus for dynamically characterizing materials is the Kolsky Bar. In compression, this apparatus is widely known as the Split Hopkinson pressure bar (SHPB), named after John Hopkinson (1849 - 1898) and his son, Bertram Hopkinson (1849 - 1898), known for demonstrating the transmission of stress waves in iron wires [17]. They conducted plate impact experiments to measure the pressure-time curves by a detonation or a bullet impact. Davies (1948) [18] studied this technique critically and discussed the dispersion of stress waves through long rods. In 1949, Kolsky modified the SHPB by adding an elastic bar on both sides (incident or input bar and reflected or output bar), and measured stress strain responses of materials under impact-loading conditions [19]. Kolsky also analysed the importance of radial inertia in the specimen during deformation, which is susceptible when the strain rate is changed very rapidly [20]. The transmission of stress waves was recorded using a condenser microphone. Later, a strain-gauging technique was introduced for this purpose [21]. Krafft et al (1954) modified the Kolsky bar design to generate the loading through an accelerated projectile launch [21]. Since then, this technique has been modified and extended to incorporate tension, torsion and bend-testing of materials at high strain rates. The technique has been reviewed by Follansbee (1995) [22], Nemat-Nasser (1991) [23], Gray et al (2000) [24], and Field et al (2004) [25].

This experiment has been commonly used to test materials such as metals [6], ceramics [26], foams [27], composites [28], and smart materials [29]. However, when building this apparatus to test softer, low-impedance materials such as elastomers, some modifications in the conventional Kolsky bar are required.

2.2.2 Conventional Kolsky Bar

A general Kolsky setup includes a sample sandwiched between two elastic, axially aligned bars, the incident and the transmission bars, as shown in Fig. 2.2. Although there is no standard design, most researchers use an apparatus that includes the following components [7]:

- Two long cylindrical elastic bars (incident and transmission bars),
- A striker-launching mechanism (usually a gas gun),
- Force/strain measuring sensors,
- Bearing and base setup for the axial alignment of the bars, and
- A data acquisition system.

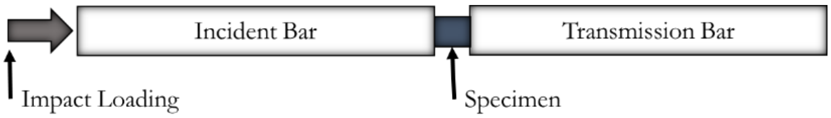

Fig. 2.2 Illustration of Kolsky bar design.

The general Kolsky setup is modified in different ways to enable the testing of a wide variety of materials. A compressive elastic stress wave is generated when the striker bar impacts the incident bar. This stress wave travels through the incident bar. Upon reaching the incident bar and the specimen interface, part of the wave is reflected and the other part is transmitted through the specimen into the transmission bar (see Fig. 2.3). Pulse profiles for the incident, transmitted and reflected waves are recorded as a function of time in both bars by strain gauges. The pulse profiles are further analysed to determine the dynamic stress strain response of the specimen [6].

The traditional choice for the bar materials is a high-strength structural material such as steel (200 *GPa*), aluminium (70-90 *GPa*) or nickel alloy (~170 *GPa*). These high-strength materials are used because the maximum yield strength of the bar determines the maximum attainable stress. Some researchers have selected low strength materials for bars such as magnesium (45 *GPa*) or polymers (<20 *GPa*) [11] [12] [13]. Low-strength bars result in a high signal-to-noise ratio and are used for high-resolution dynamic testing.

Ideally, the striker bar should be of the same diameter and material as the incident and transmission bars [6]. The impacting velocity and the length of the striker dictate the loading time of the pulse. In order to ensure a uniform response, the loading time has to be greater than the time taken for the specimen to reach stress equilibrium [11]. Under a state of equilibrated stress, the amplitude of the reflected wave is directly proportional to the maximum achievable strain rate. Similarly, the amplitude of the transmitted pulse is directly proportional to the stress developed within the specimen [6].

One assumption made by Kolsky in determining the stress strain relation is the uniform state of equilibrated stress. This can be asserted if both faces of the specimen experience equal amounts of loading. Using this assumption, we can conclude that:

$$\varepsilon_r + \varepsilon_i = \varepsilon_t \tag{2.1}$$

where ε_i, ε_r, ε_t, are the incident, reflected and transmitted strain pulses respectively, as recorded from the strain gages. Based on the assumption in relation (1), the stress and strain response of the specimen can then be calculated by:

$$\sigma_s = \frac{A_b}{A_s} E_b \varepsilon_t \tag{2.2}$$

$$\dot{\varepsilon} = -2\frac{C_b}{L_s}\varepsilon_r \tag{2.3}$$

$$\varepsilon(t) = -2\frac{C_b}{L_s}\int_0^t \varepsilon_r \, dt \tag{2.4}$$

where, $\dot{\varepsilon}$, ε and σ_s are the strain rate, strain and stress experienced by the specimen respectively.

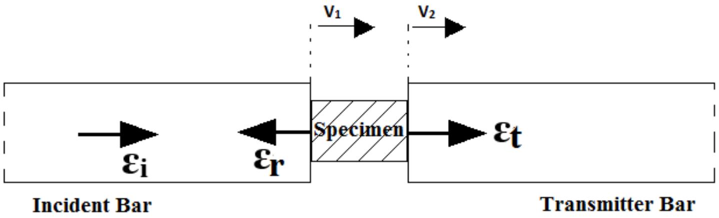

Fig. 2.3 Reflection and transmission of the incident waves.

2.2.3 Testing Conditions in a Kolsky Bar

To properly measure the deformation characteristics of a material, a specimen should undergo uniform deformation in a well-controlled environment, generally through a closed-loop feedback system. In an open-loop system like the Kolsky bar, the testing conditions depend on the specimen’s response. Therefore, the process of loading the specimen and the related testing conditions need to be carefully examined throughout the loading and unloading procedure. Furthermore, the assumptions made in data reduction schemes are challenging to satisfy in an experimental setup and thus require extra effort.

One-Dimensional Planar Elastic Wave Propagation

In a Kolsky bar design, the elastic wave propagation theory is used for data reduction schemes. The bars carrying the load are linearly elastic, and the surface strain and the stress inside the bars follow a linear relation. To facilitate one-dimensional wave propagation, the incident and transmission bars need to be sufficiently long. At impact, the amplitude of the generated pulse has a radial dependence, being maximum at centre and minimum at the surface. As the stress wave propagates, the radial stress averages out uniformly over the cross section of the bars, but with significant oscillations [30]. Therefore, the strain measured closer to the bar ends differs from the actual strain in the bar. Ideally, the strain gauges should be located at a distance equal to at least 10 times the diameter of the bar away from the ends [31]. Moreover, the bars should have a length-to-diameter ratio of at least 20.

The elastic wave transmitting over long bars may be considered as one-dimensional in nature when dealing with axial quantities. However, as the bar material is free to move in radial directions, the actual stress is still two-dimensional in nature. The acceleration of the material in radial directions causes extra inertia-induced stress in the axial direction. This acceleration-induced inertia in axial and radial directions results in wave dispersion in the form of high-frequency oscillation in the recorded signals. The effect of wave dispersion becomes greater as the bar diameter increases. In the axial direction, this effect is accumulated as the propagated distance increases. Pochhammer (1876) and Chree (1889) conducted an extensive study of wave dispersion in long, cylindrical bars [32] [33]. Their solution to the equation of motion for a sinusoidal wave propagating in an infinitely long cylinder revealed that the velocity of the elastic wave decreases with decreasing wave length.

The loading pulse generated in a Kolsky bar experiment consists of a spectrum of frequencies, with each component transmitting its own velocity of propagation. As the travelling distance of the wave increases, components with higher frequency lag behind those with low frequency, resulting in a distorted wave form. This effect of wave dispersion can be analytically modelled and corrected (Gorham 1983 & Gong et al 1990) [34] [35]. Follansbee and Frantz (1983) used a Fourier transform methodology to numerically correct the signal for the effect of dispersion [36]. The effect of wave dispersion can be minimized by using a physical filter. This piece of material is attached between the striker and the incident bars. Upon impact, the material plastically deforms and filters out high-frequency components. This technique is referred to as a pulse-shaping technique. Numerical corrections are not needed when a pulse shaper is used. The pulse-shaping technique is discussed in detail in Chapter 4.

Interfacial Frictional the Effects

A smaller-sized specimen is used in a Kolsky bar due to homogenous stress distribution. The frictional effect between the specimen and the bar interface may lead to a significant increase in the specimen's measured strength. This three-dimensional state of stress limits the lateral expansion of the specimen and leads to an overestimation of stress. For instance, a specimen bar interface with a 0.05 coefficient of friction increases the measured strength by 25% [37]. Lubrication of the specimen bar interface is required to minimize the frictional effects on the measured response of the specimen. Commonly used lubricants include high-vacuum grease, petroleum jelly [38], polytetrafluoroethylene (PTFE) [39] and vegetable oil [40].

Inertial Effects in Specimen

In Kolsky bar experiments, the intrinsic response of the material is determined by vigorously deforming the specimen at a desired rate. When the specimen is accelerated from a state of rest to this desired state, the response of the material is accompanied by an inertial effect in the axial direction. Due to Poisson's ratio, the acceleration in the axial direction is accompanied by inertia in the radial direction. This radial inertia exerts extra stress on the specimen, which is quite significant for volumetric and incompressible materials. This acceleration-induced inertial effect can be a challenge, particularly when characterizing soft materials like elastomers. It is reported that a specimen length-to-diameter ratio of $\sqrt{3}/4$ and a constant strain rate of loading should eliminate the underlying effects of this inertia [41]. A closed-form solution for the extra axial stress due to radial inertia for linear elastic materials at low rates of deformation was presented by Forrestal et al [42]. They found that the extra axial stress is distributed parabolically with a maximum at centre and zero at the surface of specimen. Later, Warren and Forrestal [43] extended this analysis to materials undergoing large elastic-plastic deformations and presented a solution for the average extra axial stress produced by the radial inertia:

$$\bar{\sigma} = \frac{3\rho r^2}{16(1-\varepsilon)^3}\dot{\varepsilon}^2 + \frac{\rho r^2}{8(1-\varepsilon)^2}\ddot{\varepsilon} \tag{2.5}$$

Where, r is the radius of the specimen, ε is the engineering strain, and $\dot{\varepsilon}$ is the engineering strain rate. It can noted from Eq. (2.5) that the extra, inertia-related stress depends on the specimen's density, radius, strain and strain rate, and can be eliminated by providing a constant strain rate of deformation to the sample.

Constant Strain Rate of Deformation

In a Kolsky bar testing, the aim is to obtain a family of stress-strain curves as a function of desired strain rates. Ensuring a constant rate of deformation in a Kolsky bar apparatus minimizes the inertial effects in the specimen, thus validating some required testing conditions.

Unlike the closed loop testing system (such as commercial load frames), where the loading is controlled through feedback, the Kolsky bar does not allow for real-time control and loading adjustment. In an ideal situation, the stress applied to the specimen should increase progressively in a linear form to provide a constant rate of deformation. Such open-loop control over the testing conditions of the specimen is an iterative process and is an integral part of the Kolsky-bar experimental design.

Pulse Shaping Technique

A constant rate of deformation and stress equilibrium are the two key working conditions in a valid Kolsky bar experiment. Most commonly, these requirements are met by using a pulse-shaping technique, which allows for controlled loading by modifying a rectangular incident pulse. This was achieved by Duffy et al [44] and Christensen [45] by impacting a conical striker instead of a cylindrical one in order to produce a ramp-based loading profile. A controlled variation in input profile can be achieved by an appropriate geometry selection of the striker. The challenge in employing this technique is the fabrication of the striker bar, which is an expensive and time-consuming process.

Ellwood et al (1982) proposed a three-bar pulse-shaping technique, in which an extra bar and specimen are stacked between the incident and the striker bars. The loading of the actual specimen is determined by the response of the extra specimen. Parry et al [46] replaced the extra third bar (the same material as the incident and the transmitted bars) with a bar of lower strength to reduce wave dispersion. Bragov and Lomounov [47] modified this technique by omitting the third bar and impacting the striker directly on to the extra specimen. The elastic-plastic response of the specimen was used to load the actual sample for testing.

Later, this technique evolved into the commonly used version of the pulse-shaping technique, in which a small piece of material (known as the pulse shaper) is attached between the striker and the incident bars. The appropriate selection of material and the geometry of the pulse shaper results in an input loading with a constant rate of deformation. The most common examples of materials for a pulse shaper include copper, aluminium, rubber, polymer, and paper. Fig. 2.4 illustrates the profile of the generated input pulse by utilizing different kinds of pulse shapers.

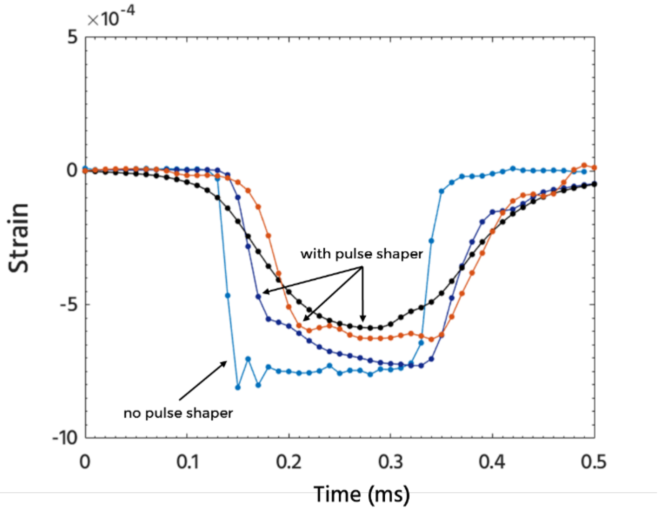

Fig. 2.4 Various Incident pulses produced by different pulse shapping designs [48].

Chapter 3 Analytical Modelling of Elastomers

Summary: In this chapter, we review the commonly implemented hyperelastic constitutive models in commercial finite element software. Performance models in finite elements were evaluated in terms of reproducibility and stability.

The response of elastomers can be described as being hyperelastic in nature, which means they have the ability to deform non-linearly when undergoing large strains. The constitutive models for elastomers can be classified as phenomenological and micro-mechanical. In the phenomenological approach, the macroscopic nature of the material is considered as a continuum. This method of deriving the constitutive relation is mainly concerned with fitting mathematical models to the experimental deformation data. A variety of hyperelastic material models will be presented in the following sections. The formulations presented are implemented in finite element analysis to analyse and validate the simulations with the experimental data.

3.1 Theory of Hyperelasticity

The isotropic elastic properties of a hyperelastic material model may be described in terms of the strain energy density function, which defines the strain energy stored in the material per unit volume. We start by defining the strain energy density function, which comprises energy stored due to volumetric changes $'\Psi_{\mathrm{vol}}'$ and elastic energy of deviatoric deformation $'\,\Psi_{\mathrm{dev}}'$:

$$\Psi = \Psi_{\mathrm{dev}}(I_1, I_2, I_3) + \Psi_{\mathrm{vol}}(J) \tag{3.1}$$

where, Ψ is the strain energy density function; I_1, I_2 and I_3 are the Cauchy-green deformation tensor invariants; and *J* is the determinant of the deformation tensor. The first, second and third invariants of the deformation tensor are expressed in terms of stretches in principal directions, λ_1, λ_2, and λ_3.

$$I_1 = {\lambda_1}^2 + {\lambda_2}^2 + {\lambda_3}^2 \tag{3.2a}$$

$$I_2 = {\lambda_1}^2{\lambda_2}^2 + {\lambda_2}^2{\lambda_3}^2 + {\lambda_3}^2{\lambda_1}^2 \tag{3.2b}$$

$$I_3 = {\lambda_1}^2{\lambda_2}^2{\lambda_3}^2 \tag{3.2c}$$

For isotropic incompressible elastomers, the generalized constitutive law is given by [11]:

$$\sigma = -pI + 2\left(\frac{\partial\Psi}{\partial I_1} + I_1\frac{\partial\Psi}{\partial I_2}\right)B - 2\frac{\partial\Psi}{\partial I_2}B^2 \tag{3.2d}$$

where p is the hydrostatic pressure (also known as the "Lagrange Multiplier") and is derived from the equilibrium equation $\nabla\sigma = 0$ and from imposed boundary conditions.

Polynomial form

The form of the polynomial strain energy potential is [49]:

$$\Psi_{PO} = \sum_{i+j=1}^{N} C_{ij}\,(I_1 - 3)^i\,(I_2 - 3)^j + \sum_{i=1}^{N}\frac{1}{D_i}\,(J^{el} - 1)^{2i} \tag{3.3a}$$

where N is the order of the polynomial; C_{ij} and D_i are temperature-dependant parameters; and J^{el} is the elastic volume ratio. The third invariant, I_3, is assumed to be zero, considering the incompressibility of the material in this model. The first term of Eq. (3.3a) represents the deviatoric part of the stored energy density resulting from shearing deformation. The second term of this equation represents the volumetric component of the stored energy density. The parameters are determined by conducting experimental tests. The shear modulus and the bulk modulus are given by:

$$\mu_0 = 2(C_{10} + C_{01}) \tag{3.3b}$$

$$K_0 = \frac{2}{D_{10}} \tag{3.3c}$$

Reduced Polynomial

The form of the reduced polynomial strain energy potential is given by [49]:

$$\Psi_{PO} = \sum_{i=1}^{N} C_{i0}\,(I_1 - 3)^i + \sum_{i=1}^{N}\frac{1}{D_i}\,(J^{el} - 1)^{2i} \tag{3.4a}$$

where C_{i0} and D_i are temperature-dependant parameters, and J^{el} is the elastic volume ratio. The shear modulus and the bulk modulus are given by:

$$\mu_0 = 2C_{10} \tag{3.4b}$$

$$K_0 = \frac{2}{D_{10}} \tag{3.4c}$$

Mooney-Rivlin

The Mooney-Rivlin strain energy potential with two parameters, including finite compressibility, is expressed in its general form as [9]. It is considered to be a pioneering model and is expressed as a linear first-order polynomial of first and second invariants of the Cauchy-green deformation tensor:

$$\Psi_{MR} = C_{10}\,(I_1 - 3) + C_{01}\,(I_2 - 3) + \frac{1}{D_1}\,(J^{el} - 1)^2 \tag{3.5a}$$

where C_{10}, C_{01} and D_1 are temperature-dependent material parameters, and J^{el} is the elastic volume ratio. The initial shear modulus and the bulk modulus in this case are given by:

$$\mu_0 = 2(C_{10} + C_{01}) \tag{3.5b}$$

$$K_0 = \frac{2}{D_{10}} \tag{3.5c}$$

Neo-Hookean

The simplest formulation of a hyperelastic model is the so-called Neo-Hookean material. It can be observed that Reduced Polynomial for *n = 1* is identical to the Neo-Hookean model [50]:

$$\Psi_{NH} = C_{10}\,(I_1 - 3) + \frac{1}{D_1}\,(J^{el} - 1)^2 \tag{3.6a}$$

where C_{10} and D_1 are temperature-dependant material parameters, and J^{el} is the elastic volume ratio. This model is expressed only in terms of the first invariant of the Cauchy-green deformation tensor. The shear modulus 'μ_0' and the bulk modulus 'K_0' for the Neo-Hookean model are given by the following relations:

$$\mu_0 = 2C_{10} \tag{3.6b}$$

$$K_0 = \frac{2}{D_{10}} \tag{3.6c}$$

Ogden

Ogden proposed a hyperelastic constitutive model for elastomers that are incompressible in nature when experiencing large deformations [14]. In contrast to polynomial forms, where the strain energy potential function is described in terms of invariants of the deformation tensors, Ogden's model is expressed in terms of stretches in principal directions. The form of this model is given below:

$$\Psi_{OG} = \sum_{i=1}^{N} \frac{2\mu_i}{\alpha_i^2} \left(\lambda_1^{-\alpha_i} + \lambda_2^{-\alpha_i} + \lambda_3^{-\alpha_i} - 3\right) + \sum_{i=1}^{N} \frac{1}{D_i} \left(J^{el} - 1\right)^{2i} \tag{3.7a}$$

where N is the order of the Ogden function; μ_i, α_i and D_i are temperature-dependant parameters; and J^{el} is the elastic volume ratio. The initial shear modulus and the bulk modulus are given by:

$$\mu_0 = 2\sum_{i=1}^{N} \mu_i \tag{3.8b}$$

$$K_0 = \frac{2}{D_1} \tag{3.7c}$$

Particular choices of μ_i and α_i in Ogden's model result in the Mooney-Rivlin and the Neo-Hookean forms.

Yeoh

This model is a special form of the reduced polynomial with three-term expansion (n = 0 and m = 3). The Yeoh form of the strain energy potential depends only on the first invariant of the deformation tensor (I_1) [13]. It is one of the most widely implemented models in FE packages, and has proven to be robust and easy to use. The constitutive relation for this model is given below:

$$\begin{aligned}\Psi_{YH} = \; & C_{10}\,(I_1 - \;3) + \;C_{20}\,(I_1 - \;3)^2 + C_{30}\,(I_1 - \;3)^3 \\ & + \frac{1}{D_1}\,(J^{el} - 1)^2 \; + \frac{1}{D_1}\,(J^{el} - 1)^4 \; + \frac{1}{D_1}\,(J^{el} - 1)^6\end{aligned} \tag{3.8a}$$

where C_{i0} and D_i are temperature-dependant parameters, and J^{el} is the elastic volume ratio. The shear modulus and the bulk modulus are given by:

$$\mu_0 = 2C_{10} \tag{3.8b}$$

$$K_0 = \frac{2}{D_{10}} \tag{3.8c}$$

Van der Waals form

The Van Der Waal's form of the strain energy potential is given by [51]:

$$\begin{aligned}\Psi_{vw} = \; & \mu\left\{-(\lambda_m^2 - 3)[\ln(10 - \eta) + \;\eta] - \frac{2}{3}a\left(\frac{\tilde{I} - 3}{2}\right)^{\frac{2}{3}}\right\} \\ & + \frac{1}{D}\left(\frac{J_{el}^2 - 1}{2} - \ln(J_{el})\right)\end{aligned} \tag{3.9a}$$

where $\tilde{I} = (1 - \;\beta)I_1 + \;\beta I_2$ and $\eta = \sqrt{\frac{\tilde{I}-3}{\lambda_m^2-3}}$; μ is the initial shear modulus; λ_m is the locking stretch; a is the global interaction parameter; β is an invariant mixture parameter; and D dictates the compressibility. The initial shear modulus and the bulk modulus are given by the following relation:

$$\mu_0 = \mu \tag{3.9b}$$

$$K_0 = \frac{2}{D_0} \tag{3.9c}$$

Arruda-Boyce

Arruda-Boyce deduced a constitutive model for the large stretch behaviour of rubber-like elastic materials [49]. The model is based on the 8-chain representation of the volume structure of the material. The represented volume element consists of a cube with 8 chains attached from the edges to the centre. The form of the Arruda-Boyce strain energy potential is given by:

$$\Psi = \mu\left\{\frac{1}{2}(I_1 - 3) + \frac{1}{20\lambda_m^2}(I_1^2 - 9) + \frac{11}{1050\lambda_m^4}(I_1^3 - 27) + \frac{19}{7000\lambda_m^6}(I_1^4 - 81) + \frac{519}{673750\lambda_m^8}(I_1^5 - 243)\right\} + \frac{1}{D}\left(\frac{J_{el}^2 - 1}{2} - \ln(J_{el})\right) \tag{3.10a}$$

where D and μ are temperature-dependant material constants; λ_m is the number of rigid links composing a single chain and is typically equal to 7; and J^{el} is the elastic volume ratio. The initial shear modulus is linked to μ with the following relation:

$$\mu_0 = \mu(1 + \frac{3}{5\lambda_m^2} + \frac{99}{175\lambda_m^4} + \frac{513}{875\lambda_m^6} + \frac{42039}{67375\lambda_m^8}) \tag{3.10b}$$

The initial bulk modulus is related to D with the expression:

$$K_0 = \frac{2}{D} \tag{3.10c}$$

3.2 Modelling of Elastomers

3.2.1 Mechanical Testing

In order for the design simulations to be accurate, it is necessary for the material parameters to be determined from testing conducted under appropriate conditions. The model coefficients must be derived from test data extracted at temperature and strain rates of interest. The combination of test data required to calculate the deviatoric coefficients includes:

1. Uniaxial Tension
2. Planar Tension
3. Equibiaxial Tension
4. Volumetric Compression

Uniaxial Tension

Under uniaxial tension, the sample achieves a state of pure tensile strain as the length in the direction of loading is greater than the width of the sample (see Fig. 3.1a). This test determines the properties of the material under plane stress. The uniaxial deformation mode is characterized in terms of the principal stretches, λ_i, as:

$$\lambda_i = \lambda_U, \qquad \lambda_2 = \lambda_3 = \frac{1}{\sqrt{\lambda_U}} \tag{3.11a}$$

where λ_U is the imposed displacement boundary condition. The nominal strain is defined as:

$$\varepsilon_U = \lambda_U - 1 \tag{3.11b}$$

Uniaxial nominal stress, σ_{uni}, can be derived by applying the principal of virtual work:

$$\delta\Psi = \sigma_U \delta\lambda_U \tag{3.11c}$$

$$\sigma_{Uniaxial} = \frac{\partial\Psi}{\partial\lambda_U} = 2(1 - {\lambda_U}^{-3})(\lambda_U \frac{\partial\Psi}{\partial I_1} + \frac{\partial\Psi}{\partial I_2}) \tag{3.11d}$$

Planar Tension

In planar tension, the specimen experiences a state of stress equal to the pure shear test. The test is similar to uniaxial tension and is conducted on a specimen with a width at least 4 times longer than the length in loading direction (see Fig. 3.1b). The planar mode of deformation can also be characterized in terms of principal stretches as:

$$\lambda_1 = \lambda_P, \qquad \lambda_2 = 1, \qquad \lambda_3 = 1/\lambda_P \tag{3.12a}$$

where λ_P stretches in the loading direction for the planar tension test. The nominal strain in this case can be defined as $\varepsilon_P = \lambda_P - 1$. When dealing with the logarithmic strain for this mode of deformation, the test is equal to a pure shear state in the specimen at an angle of 45^0 to the loading direction. Again, nominal planar stress can be derived from the principal of virtual work as:

$$\delta\Psi = \sigma_P \delta\lambda_P \tag{3.12b}$$

$$\sigma_{Planar} = \frac{\partial\Psi}{\partial\lambda_P} = 2(\lambda_P - {\lambda_P}^{-3})(\frac{\partial\Psi}{\partial I_1} + \frac{\partial\Psi}{\partial I_2}) \tag{3.12c}$$

Equibiaxial Tension

In equibiaxial tension, the sample is deformed under equal tensile stresses along two orthogonal directions. This equal state of biaxial stress can also be achieved by stretching a circular disk in radial directions, as illustrated in Fig. 3.1c. For incompressible or nearly incompressible materials, equal biaxial extension of a specimen creates a state of strain that is equal to simple compression. The equibiaxial deformation mode is characterized in terms of principal stretches as:

$$\lambda_1 = \lambda_2 = \lambda_B, \qquad \lambda_3 = 1/{\lambda_B}^2 \tag{3.13a}$$

where λ_B is the stretch in two perpendicular loading directions. In a circular sample, this is the stretch in the radial direction. The principal of virtual work can be used to derive the expression for nominal stress for equibiaxial deformation:

$$\delta\Psi = 2\sigma_B \delta\lambda_B \tag{3.14a}$$

$$\sigma_{Biaxial} = \frac{1}{2}\frac{\partial\Psi}{\partial\lambda_B} = 2(\lambda_B - \lambda_B^{-5})(\frac{\partial\Psi}{\partial I_1} + \lambda_B^2 \frac{\partial\Psi}{\partial I_2}) \tag{3.15a}$$

Volumetric Compression

This test is carried out to analyse the compressibility of materials. Loading is applied in the direction perpendicular to cylinders cross section, while displacements in the radial direction are limited (see Fig. 3.1d). The pressure experienced in the cross-sectional area is measured with respect to the volumetric change in the sample. The bulk modulus is the initial slope of the stress strain response measured under volumetric compression.

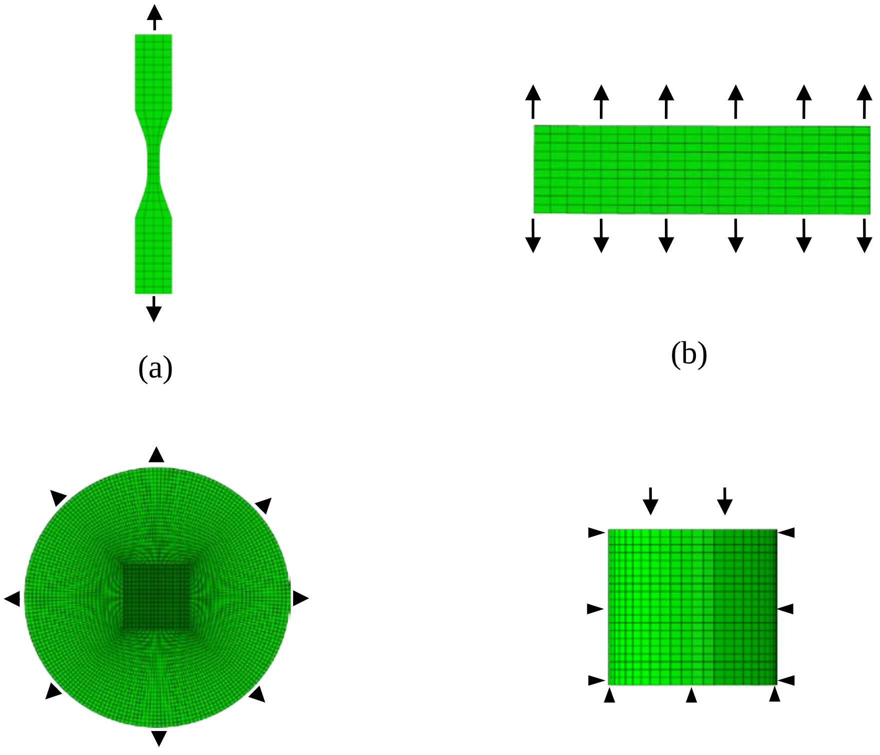

(a) (b) (c) (d)

Fig. 3.1 Modes of deformation, (a) uniaxial tension, (b) planar tension, (c) equibiaxial tension, and (d) volumteric compression.

3.2.2 Finite Element Modelling of Elastomers

The validation of hyperelastic models with elastomers in experimental data has been performed by simulating the elastomers under (i) uniaxial tension, (ii) planar tension, and (iii) equibiaxial tension using finite element analysis. To model uniaxial tension, an ASTM D638 Type-V specimen (Fig. 3.1a) is constrained ($U_x = U_y = U_z = 0$), while displacement is applied to the nodes at the other end. For planar tension, a sample with a width of 150 *mm* and a length of 30 *mm* is constrained at one end, and displacement is applied to the nodes at the other end. For the biaxial sample, a cylindrical disc with a radius of 31.75 *mm* is loaded in radial direction using cylindrical boundary conditions. Similarly, in the volumetric sample, the displacement of nodes in the radial direction is restricted. The bottom of the sample is fixed, and loading is applied on the opposite end.

Experimental tests are modelled in Abaqus explicit with a total step time of 1 second. Ramp type loading is applied in the form of nodal displacement. The geometries of the samples are meshed with three-dimensional continuum 8-node elements (C3D8). Because the bulk modulus of the elastomers is higher than the shear modulus, simulations are prone to various errors; for example, strain locking and large changes in stress due to small changes in displacement. These errors can be avoided by using elements with reduced integration formulation. To validate the model and to evaluate the model parameter, experimental data published by Treolar [50] is used. Using this experimental data, model parameters for the reduced polynomial (N = 3) are calculated and then used to model the response of the samples. The experimental vs. FEM stress strain response for uniaxial tension, planar tension, equibiaxial tension, and volumetric compression are illustrated in Fig. 3.2 to Fig. 3.5. Since, in Abaqus, the output stress is the Cauchy or true stress which is the stress determined by the instantaneous load acting on the instantaneous cross section. For post-processing and validation with experimental results, nominal/engineering stresses are required. For this, reaction forces from the nodes are extracted and divided by the cross-sectional area to evaluate the nominal stress.

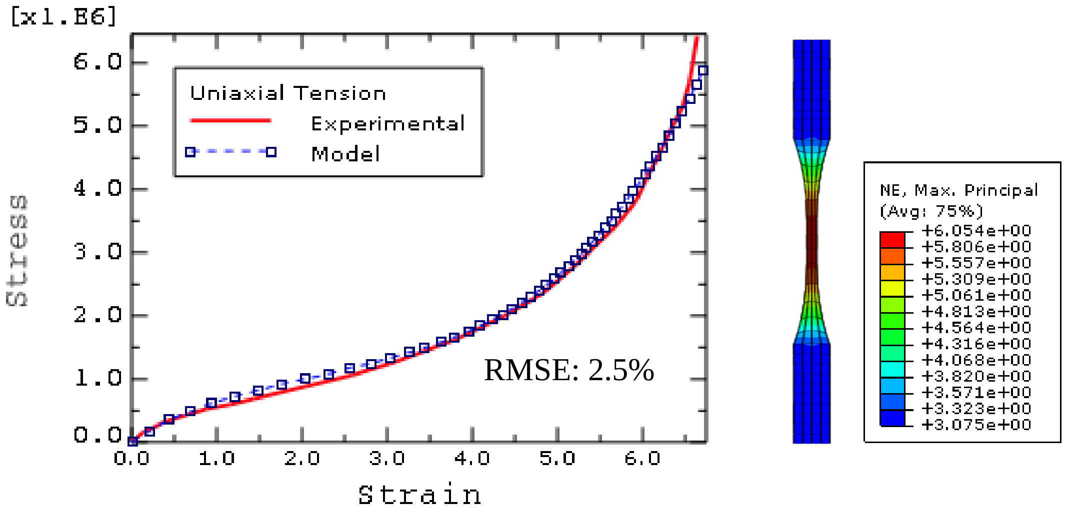

Fig. 3.2 Uniaxial tension stress (N/m^2) vs strain, FEA model vs experimental.

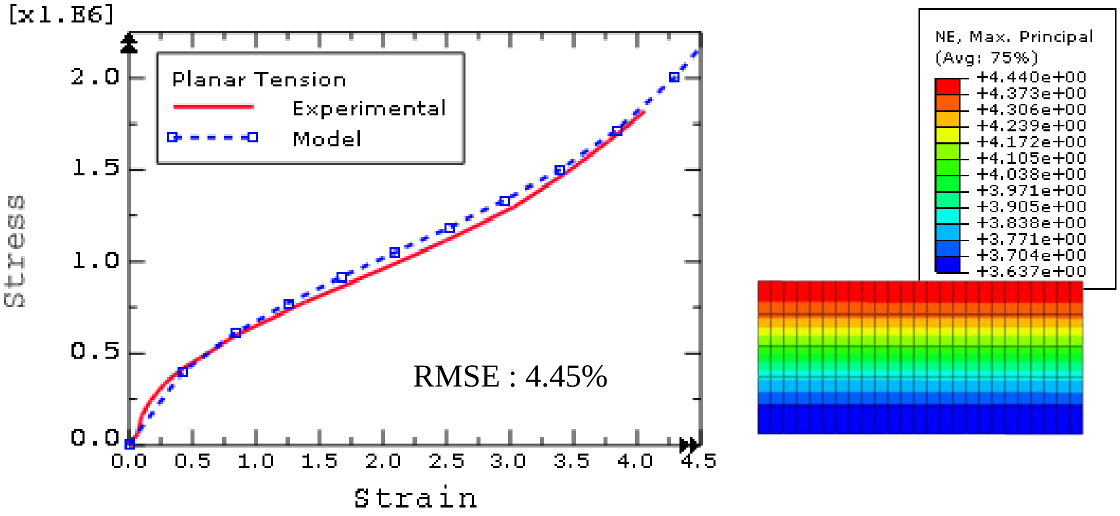

Fig. 3.3 Planar tension stress (N/m^2) vs strain, FEA vs experimental.

For strain calculation Abaqus outputs nominal/engineering (the amount that a material deforms per unit length in a tensile test) and true strain (the natural log of the quotient of current length over the original length). To evaluate the strain, elemental nominal strain is outputted from the model.

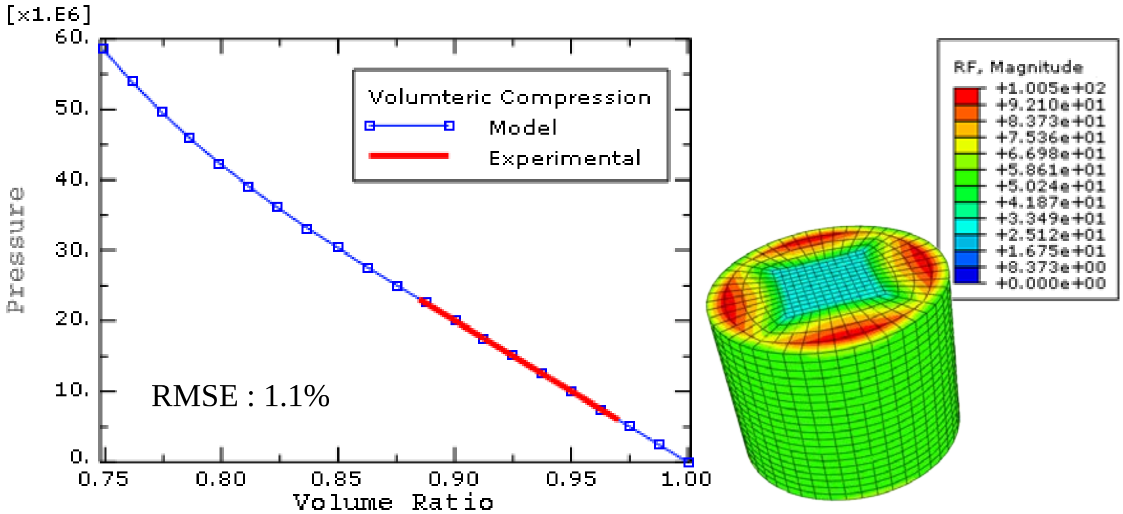

Fig. 3.4 Volumetric compression pressure (Pa) vs volume ratio (V/V_o) FEA vs experimental.

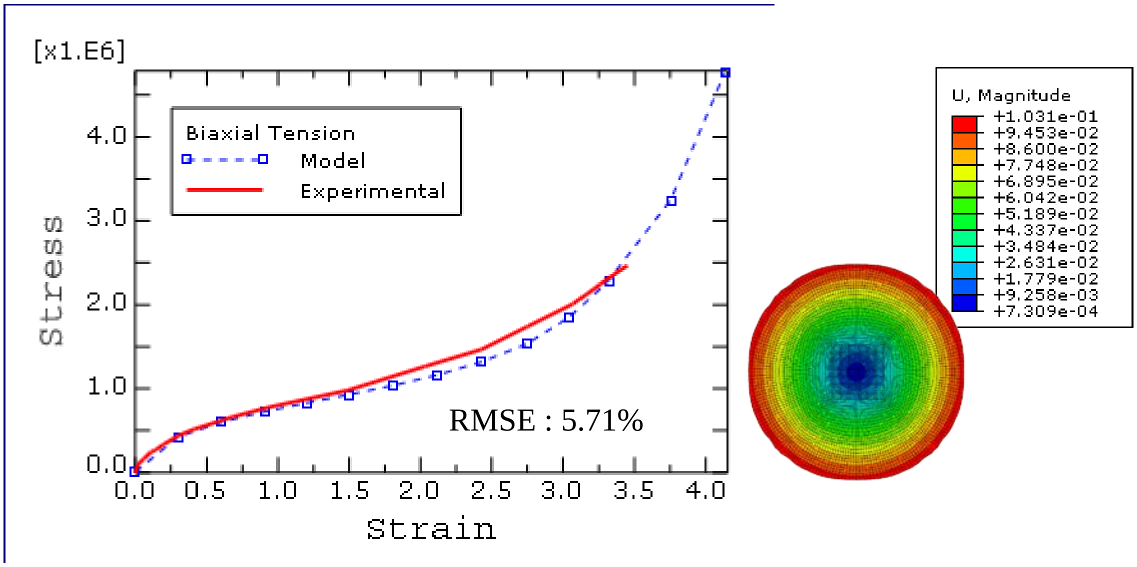

Fig. 3.5 Biaxial tension stress (N/m^2) vs strain, FEA vs experimental

3.2.3 Hyperelastic Models: Comparison and Performance Study

The successful modelling and design of elastomer materials depend on the selection of an appropriate strain energy function and the accurate determination of coefficients in the function. A suitable hyperelastic material model is chosen based on the application of specific loading conditions and the available experimental test data for the material under investigation. An efficiently performing hyperelastic material model should have the following qualities [51]:

- Should be able to exactly reproduce and predict the entire non-linear S-shaped stress and strain response as illustrated in Fig. 2.1,
- Should handle a change in deformation mode well, that is, it should not only predict deformation in response to one type of tension (such as uniaxial tension), but should also satisfactorily predict the deformation in response to other type of loadings such as planar tension, biaxial tension and volumetric compression,
- Should require a small number of material parameters, that is, it should require minimum testing to evaluate the parameters, and
- Should have a simple mathematical formulation to render numerical implementation possible.

To be able to accurately model the response of a non-linear hyperelastic specimen under investigation, the values for the material constant must be determined. This is done by performing uniaxial tension, biaxial tension, planar tension and volumetric compression tests. These modes of deformation are illustrated in Fig. 3.1. The material constants are evaluated using a curve-fitting technique, such as the ‘least squares method’. Upon the evaluation of model parameters, the simulated stress-strain curve can be compared to the experimental data for various hyperelastic models.

Comparison is made in terms of (i) how well the predicted curves approximate experimental data, (ii) the accuracy of the calculated curves, in case limited test data is available, and (iii) the stability in terms of the Drucker Stability Criterion [52]. For this purpose, experimental data describing the characteristics of rubber, published by Treloar (1944) [50] is used to calculate the material model. Two cases were analysed:

i) For the first case, model parameters were evaluated using experimental test data for the modes of deformation data listed in Fig. 3.1.
ii) For the second case, model parameters were evaluated using experimental test data for uniaxial tension only.

For each case, the following material models were analysed:

- Polynomial form N = 2
- Reduced polynomial N = 1 (Neo-Hookean)
- Reduced Polynomial N = 3 (Yeoh)
- Ogden N = 1 & N = 3
- Arruda-Boyce
- Van der Waals’ form

Case 1: Using three modes of deformation data

For this case, all three types of data are used to fit the constitutive equation. It was noted that the Mooney-Rivlin (polynomial form with N = 1) gives a good fit in the initial strain regime, but is unable to reproduce the strain stiffening and deviates at high strains. A higher-order polynomial form (with N = 2) provides a closer correlation than N = 1 at all strain levels. This behaviour is evident from Fig. 3.6 to Fig. 3.8.

Similarly, for the two cases of reduced polynomial, Yeoh, the three-term reduced polynomial function, provides a more accurate representation of the test data as compared to Neo-Hookean, the one-term function. Also, the Yeoh model was found to be stable over all strain regimes. It can be seen from the results in Fig. 3.9 to Fig. 3.11 that Neo-Hookean linearly depends on the first invariant only and fails to reproduce the upturn due to strain stiffening.

The Arruda-Boyce model provides a reasonable fit with a slight overestimation of stresses and a less steep upturn in the mid strain region for the uniaxial case. The Van der Waals provides a better fit than the Arruda-Boyce, with high accuracy across all strain regions.

However, the Ogden model (of orders 2 and 3) provides very close fits, with order three (N = 3) showing the best correlation as compared to the rest.

Using only limited data gives different results. This is described in the second case scenario.

Case 2: Using only uniaxial tension data

A completely different conclusion is reached when only limited test data is available. Since only limited test data was considered for this case, all the models performed well in predicting the uniaxial tension response for the unit cube, except for the Polynomial(N = 1) and the Neo-Hookean forms. The Polynomial (N = 1) form also exhibited a lot of instability in predicting the uniaxial and planar tension (Fig.3.9 and Fig. 3.10).

The Ogden model exhibits large differences, especially in the case of planar and biaxial extensions. Ogden (N = 3) diverges significantly at mid strains, and Ogden (N = 2) performs well in predicting higher strains.

The Yeoh model gives a good third-order approximation for all modes of deformation without exhibiting any instabilities. This model even provides a reasonable fit for the modes of deformation for which test data was not taken into account.

When using only uniaxial data to derive the material coefficients for the hyperelastic material models taken into account, the Arruda-Boyce and the Van der Waals models provide the best fit as compared to the rest. Similar observations have been reported by Kaliske and Rotherth [53].

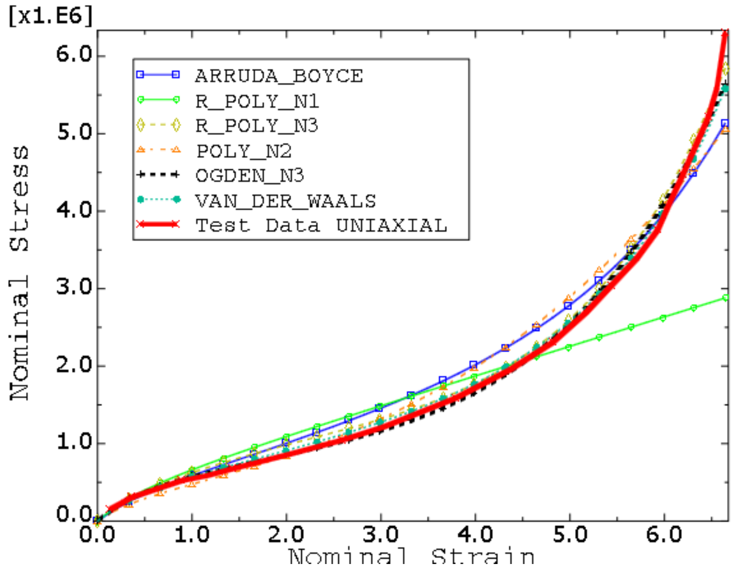

Fig. 3.6 Case 1: Uniaxial tension stress (N/m^2) vs. strain results.

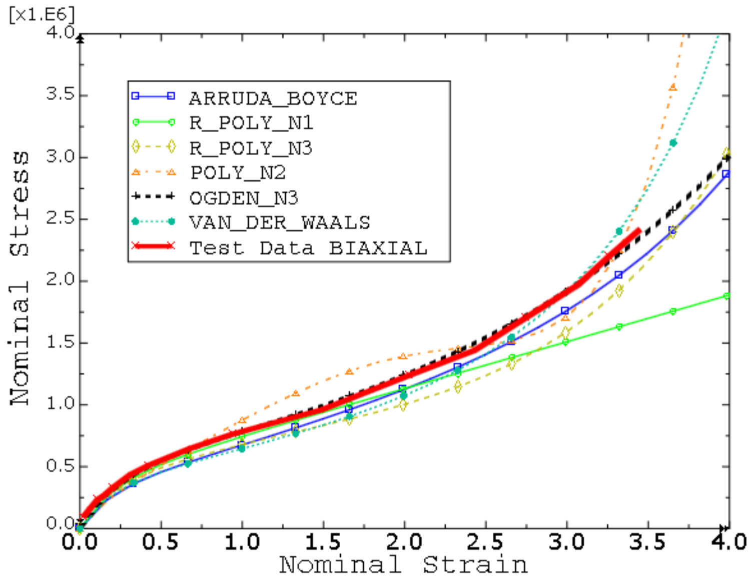

Fig. 3.7 Case 1: Planar tension stress (N/m^2) vs. strain results.

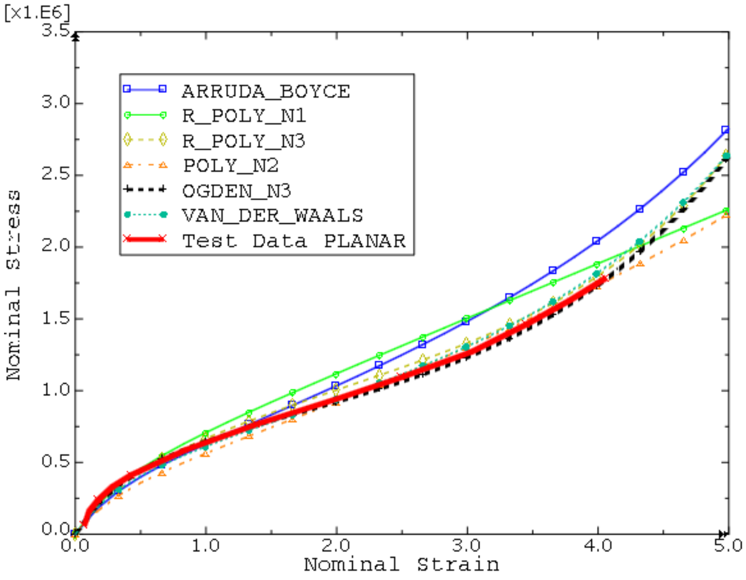

Fig. 3.8 Case 1: Biaxial tension stress (N/m^2) vs. strain results.

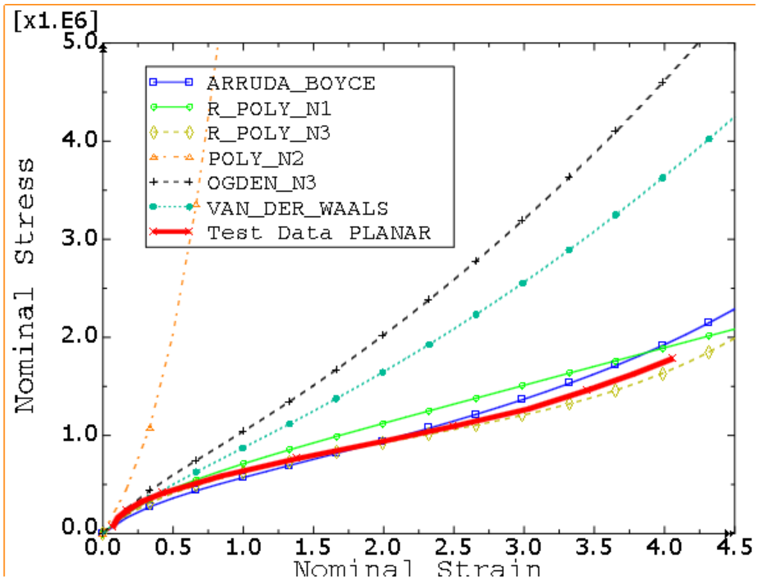

Fig. 3.9 Case 2: Uniaxial tension stress (N/m^2) vs. strain results

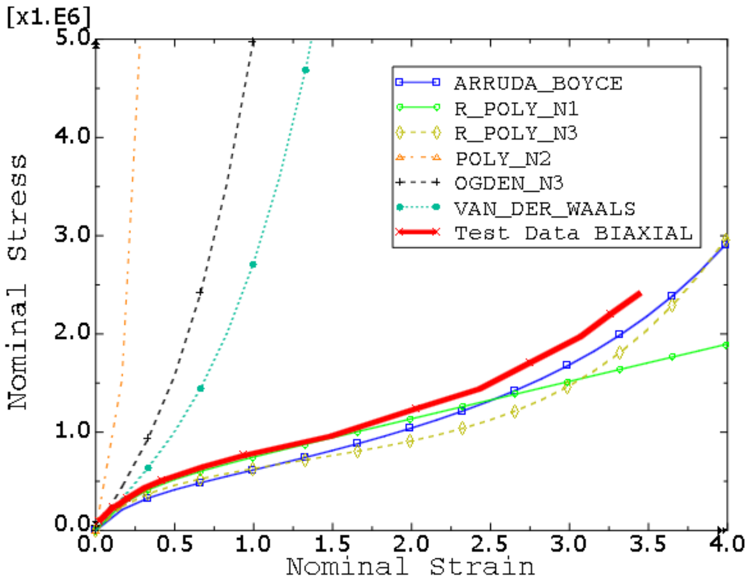

Fig. 3.10 Case 2: Biaxial tension stress (N/m^2) vs. strain results.

.

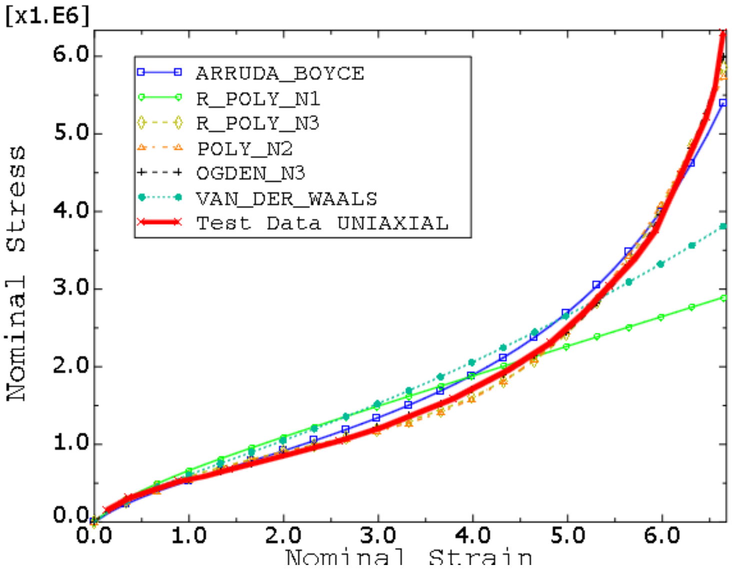

Fig. 3.11 Case 2: Planar tension stress (N/m^2) vs. strain results.

Model	*Parameter*								
Polynomial N=1 (Mooney-Rivlin)	C_{10}	C_{01}	D_1						
	218739.33	1189.38	9.96E-09						
Polynomial N=2	C_{10}	C_{20}	C_{01}	C_{11}	C_{02}	D_1	D_2		
	115773.67	2269.30	34742.30	-1778.01	85.21	9.92E-09	-4.43E-09		
Reduced Polynomial N=1 (Neo-Hookean)	C_{10}	C_{01}	D_1						
	192433.15	0	9.97E-09						
Reduced Polynomial N=3 (Yeoh)	C_{10}	C_{20}	C_{30}	D_1	D_2	$D3$			
	186938.93	-1410.59	38.786	9.90E-09	-1.39E-08	4.78E-10			
Ogden N=1	μ_1	α_1	D_1						
	348479.25	2.16	9.96E-09						
Ogden N=3	μ_1	μ_2	μ_3	α_1	α_2	α_3	D_1	D_2	D_3
	371711.66	643.63	17239.2368	1.54	5.85	-1.829	9.90E-09	-1.39E-08	4.78E-10
Arudda-Boyce	μ	μ_0	μ_m	D					
	328334.44	335781.94	5.23	1.04E-08					
Van der Waals	μ	λ_m	A	β	D				
	362942.99	10.8010712	0.23	9.72E-03	1.04E-08				

Table 3.1 Material parameters for various hyperelastic models.

Chapter 4 Numerical Modelling of a Kolsky Bar

Summary: In this chapter, we present a comprehensive methodology to numerically model the working of the Kolsky bar developed for high strain rate testing of elastomers. A finite element analysis is conducted to validate the experimental design and to select appropriate testing parameters for the Kolsky bar.

4.1 Finite Element Model of a Kolsky Bar

The numerical simulations to validate the modified Kolsky design have been performed using the Abaqus/Explicit package, which makes use of the explicit dynamic integration method, also known as the forward Euler or central difference algorithm [52]. Abaqus/Explicit has the advantage of solving very high-speed dynamic problems with a robust contact algorithm, avoiding any additional degrees of freedom.

The explicit dynamics procedure makes use of wave propagation to reach a bounded solution. Converging to a solution depends upon the time increment 'Δt' of each step, which has to be less than the minimum time increment. If $\Delta t > \Delta t_{min}$, the solution is unstable and oscillations will be observed in the solution. The stability limit for each time increment can be defined in terms of the highest eigenvalue in the model 'ω_{max}' and the critical damping 'ξ' in the highest mode, as given by:

$$\Delta t \leq \frac{2}{\omega_{max}}\left(\sqrt{1+\ \xi^2}-\ \xi\right) \tag{4.1}$$

The concept of a stable time increment can be thought of as the time required for the wave to propagate over the length of the smallest-sized element 'L_e' with the speed 'c'. The stable time increment can be expressed as [52]:

$$\Delta t = \frac{L_e}{c} \tag{4.2}$$

Decreasing the stable time increment increases the computational cost. It can be noted from Eq. 4.2 that increasing the wave speed 'c' and decreasing the element size 'L_e' can reduce the time increment. Therefore, the computational time for solving the model can be greatly increased by (i) decreasing the element size, (ii) decreasing material compressibility, (iii) increasing material stiffness, and (iv) decreasing material density. For the case of modelling the Kolsky bar, material stiffness and density cannot be changed as the particular choice of material depends on the design constraint imposed when testing soft materials as discussed in [54]. However, the stable time increment can be increased by using a fine mesh.

Another technique used to reduce the computational time was to reduce the symmetry of the model, considering only 1/16th part of it as shown in Fig. 4.1. The whole model was meshed using three-dimensional continuum elements with reduced integration (C3D8R). The mesh was refined by sectioning the whole model and using a 6-node wedge shape around the axis and 8-node, hex-shaped elements for the rest of the model. Next, each bar was partitioned into three sections, two smaller sections around the impacting interfaces and a third one comprising the rest, as shown in Fig. 4.1a. The two smaller sections were finely meshed with an element size of (1 *mm*) and the third section with two cases of element lengths (fine = 10 *mm* and coarse = 100 *mm*). It was discovered that sectioning the length of the bar with a coarse mesh gave reasonable results with fewer high-frequency components. This is because, to fully capture a wave, the minimum required length of an element is equal to one-tenth of the wavelength. Moreover, using a very small stable time increment induces high frequency oscillations in the signal due to the reflection of stress wave at elemental boundaries as it propagates through the material. The incident, transmission and striker bars are modelled as an isotropic elastic material with a Young Modulus of 70 *GPa* and a density of $2700\ kg/m^3$. The pulse shaper and the specimen were meshed using the same combination of hex and wedge elements. The constitutive models used for the pulse shaper and the elastomeric specimen are discussed in the next sections.

Constitutive Model Parameters

The elastomer specimen is modelled as a hyperelastic material, and the constitutive model used to describe the material's response is the strain energy function given by Ogden [14] of order three, Eq. 4.3. The coefficients of the strain energy function are calculated by Abaqus through the curve-fitting of uniaxial, biaxial, planar and volumetric compression experimental data for natural rubber. The model parameters calculated are summarized in Table 4.1.

$$U = \sum_{i=1}^{N} \frac{2\mu_i}{\alpha_i^2} \left(\bar{\lambda}_1^{\alpha^i} + \bar{\lambda}_2^{\alpha^i} + \bar{\lambda}_3^{\alpha^i} - 3 \right)^i + \sum_{i=1}^{N} D_i (J^{el} - 1)^{2i} \tag{4.3}$$

where, U is the strain energy density function, N is the order of polynomial, $\bar{\lambda}_i$ are the principal stretches, J^{el} is the elastic volume ratio stretches, and μ_i , α^i and D_i are the temperature-dependent material parameters.

The pulse shaper was modelled as an elastic-plastic material, with its volumetric response defined by the equation of state and its deviatoric response by the linear elastic shear and the Johnson-Cook model [52]. The input parameters used to define these material models are summarized in Table 1. The equation of state used is the linear Hugoniot form 'U_s-U_p' and is given in Eq. 4.4 [52], while the strain rate dependent relation used in Abaqus for the Johnson-Cook model is given by Eq. 4.5. The strain rate dependent plastic model predicts the stress flow to plastically deform the material absorbing the high-frequency components.

$$\bar{\sigma} = \left[A + B(\dot{\bar{\varepsilon}}^{pl})^n\right] \left[1 + C \ln\left(\frac{\dot{\bar{\varepsilon}}^{pl}}{\dot{\varepsilon}_0}\right)\right] \left[1 - \hat{\theta}^m\right] \tag{4.4}$$

where $\bar{\sigma}$ is the yield stress at non-zero strain rate, $\dot{\bar{\varepsilon}}^{pl}$ is the equivalent plastic strain rate, and A, B, C, n, m, and $\dot{\varepsilon}_0$ are material parameters measured at or below the transition temperature.

$$p = \rho_0 {c_0}^2 \eta \frac{\rho_0 {c_0}^2 \eta}{(1 - s\eta)^2} \left(1 - \frac{\Gamma_0 \eta}{2}\right) + \Gamma_0 \rho_0 E_m \tag{4.5}$$

where, $\rho_0 {c_0}^2$ is equivalent to elastic bulk modulus at small nominal strains, $\eta = 1 - \rho_0/\rho$ is the nominal volumetric compressive strain, ρ_0 is the reference density, Γ_0 is the material constant (also known as Gruneisen gamma), and E_m is the internal energy per unit mass.

Model	**Parameters**					
	$\boldsymbol{A}$	$\boldsymbol{B}$	$\boldsymbol{C}$	$\boldsymbol{n}$	$\boldsymbol{m}$	$\dot{\boldsymbol{\varepsilon}}_{\boldsymbol{0}}$
J-C	92x10^{6}	292x10^{6}	0.025	0.31	1.09	1
	$\boldsymbol{c_o}$		$\boldsymbol{s}$		$\boldsymbol{\Gamma_0}$	
U$_s$-U$_p$	3933		1.5		1.99	
	$\boldsymbol{\mu_i}$		$\boldsymbol{\alpha^i}$		$\boldsymbol{D_i}$	
Ogden	μ_1: 365227.2		α^1: 1.544		D_1: 1.00x10^{-8}	
	μ_2: 643.74		α^2: 5.846		D_2:-1.41x10^{-8}	
	μ_3: 16712.2		α^3: -1.834		$D_3$4.87x10^{-10}	

Table 4.1 Johnson-Cook and Equation of State input parameters for pulse shaper and Ogden parameters for specimen.

Loading and Boundary Conditions

Boundary conditions were imposed on the entire model, radially limiting the motion of the nodes. The end of the transmission bar was not fixed. After the reflection from the free end, the direction of the propagating wave was reversed. However, it should be noted that the displacement value of the nodes is doubled around the reflecting boundary, so the strain/stress history should be extracted some distance from the free end. One can choose to limit the end surface of the transmitter bar in a longitudinal axis, but it does not have any effect other than the change in direction.

Loading is applied by a predefined velocity field in the longitudinal axis over the striker. Values of velocity used in this study range from 1 *m/s* to 40 *m/s*. Other loading conditions such as (i) the pressure load and (ii) the initial velocity boundary condition were also applied to analyse the compatibility between them. It was noted that, when applying the initial velocity boundary condition using an instantaneous amplitude as defined by Abaqus, the pulse shaper element can be critically deformed due to the acceleration-induced inertia. In the case where this condition is used, the amplitude should be changed to a step amplitude.

Surface properties for the interacting interfaces were defined in contact pairs, using the Abaqus surface-to-surface interaction. The penalty contact algorithm is used to model the contact interaction. One advantage of penalty contact is that it enables a balanced master-slave approach for contact between rigid and deformable bodies.

The modelling of very high-speed dynamic events can be improved by introducing damping associated with volumetric changes in the form of bulk viscosity components. The bulk viscosity is defined for the whole model within the definition of each step. Values for elements can be changed using a scale factor in the element definition. The values used for linear (Q1 = 1.5) and quadratic (Q2 = 1) bulk viscosity are based on the suggestion made in reference [55]. The analysis was conducted with an explicit step size of 1 *ms*. The NL Geom option was used in the step definition to account for geometric nonlinearity in large deformation analysis. The elemental stress and strain values were extracted from the middle of the incident and the transmission bars.

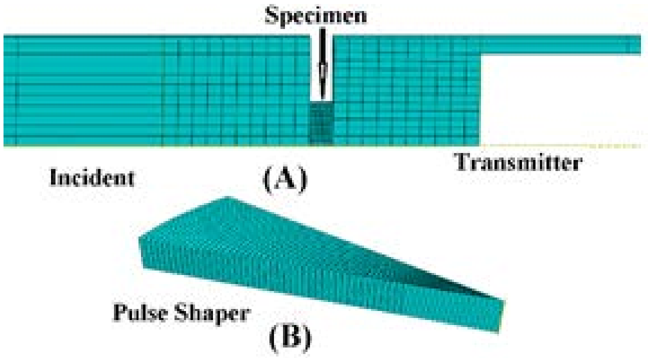

Fig. 4.1 (a) Incident, transmitter and specimen mesh; (b) Pulse-shaper mesh illustration.

4.2 Finite Element Analysis

4.2.1 Effect of Mesh

In order to capture a wave of interest, the length of at least 10 elements should be equal to the wavelength of the expected wave propagating through the bars. To study the effect of mesh size on the generated results, elements with two different aspect ratios were modelled. In the fine mesh case, an element size of 10 *mm* x 1*mm* x 1*mm* was used, whereas for the coarse mesh, an element size of 100 *mm* x 1 *mm* x 1*mm* was used. Fig. 4.2 shows the effect of mesh size on the generated pulse. A Finer mesh resulted in fewer oscillations in the recorded incident wave while increasing the computational time.

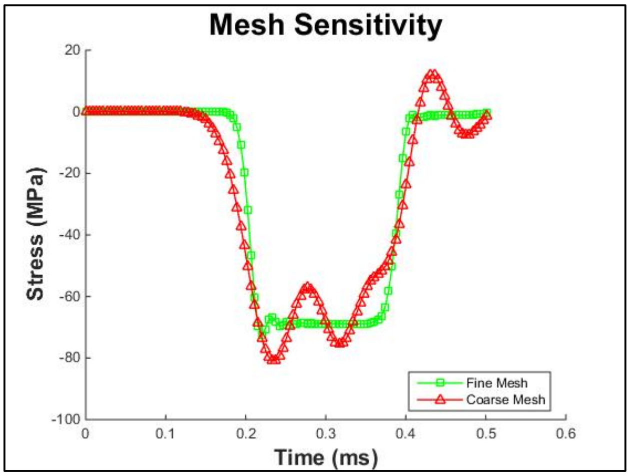

Fig. 4.2 Incident loading pulse for different mesh size.

4.2.2 Shape of Striker

Fig. 4.3 illustrates the effect of using a regular cylindrical and tapered striker with different taper lengths. The striker bar was tapered to a point with dimensions of 1*cm*, 5*cm* and 10*cm* from the side opposite to the incident bar. The purpose of this analysis was to investigate whether tapering a striker from one side would have any effect on the rise time. It can be concluded from Fig. 4.3 that tapering the striker did not have any effect on the rise time of the loading pulse. Furthermore, oscillations in the signal increased with the decrease in taper length. Increasing the taper length also decreased the time period of the loading pulse.

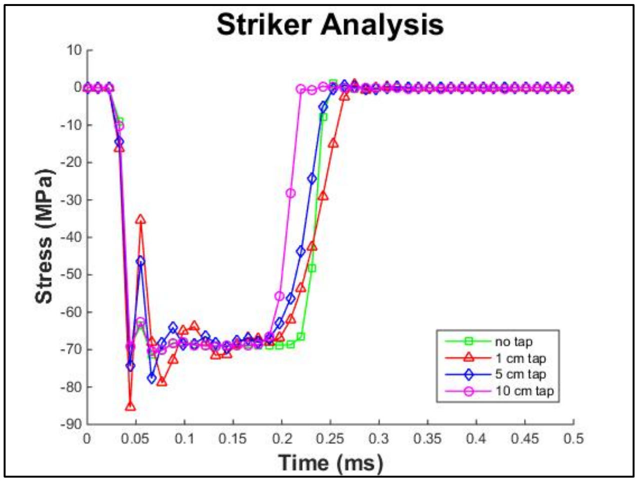

Fig. 4.3 Incident pulse generated as a result of using a striker with different tap length.

4.2.3 Pulse Shaper

This section presents the analysis made on pulse shapers placed between the striker and the incident bar to (i) reduce the wave dispersion by physically filtering out the high-frequency components in the generated pulse through elastic-plastic deformation, and (ii) to facilitate stress equilibrium by increasing the rise time of the loading pulse. By using a pulse-shaper, various profiles of loading pulses can be generated to characterize materials like elastomers, with characteristics affected by the loading shape of the pulse. The profile of the incident wave generated through the pulse shaping technique is dependent on the geometry and material of the pulse-shaper as well as on the impact velocity of the striker. Such an example is shown in Fig. 4.4, which illustrates experimental results for different profiles of incident pulses by utilizing various materials widely used for this purpose.

To characterize this effect, a scalar measure of plastic strain is taken into consideration for various pulse shaper geometries. This indicates that total plastic deformation is taking place in the pulse shaper upon the impact of the striker. Fig. 4.5 shows the resultant plastic strains for different diameter-to-thickness (D/T) ratios of the pulse shaper, keeping D constant at 20 *mm*. In this case, the impacting velocity of the striker was set at 10 *m/s* and 30 *m/s*.

Similarly, Fig. 4.6 illustrates the resultant plastic strain in the pulse shaper when impacted at 10 *m/s*, keeping the thickness constant at 1 *mm*. In both cases, the amount of plastic deformation taking place in the pulse shaper increases as the difference between the diameter and thickness of the pulse shaper becomes larger. Furthermore, decreasing the thickness while keeping the diameter constant increases the rate of plastic deformation taking place in the pulse shaper. Similarly, increasing the diameter with constant thickness decreases the equivalent plastic strain attained by the pulse shaper component.

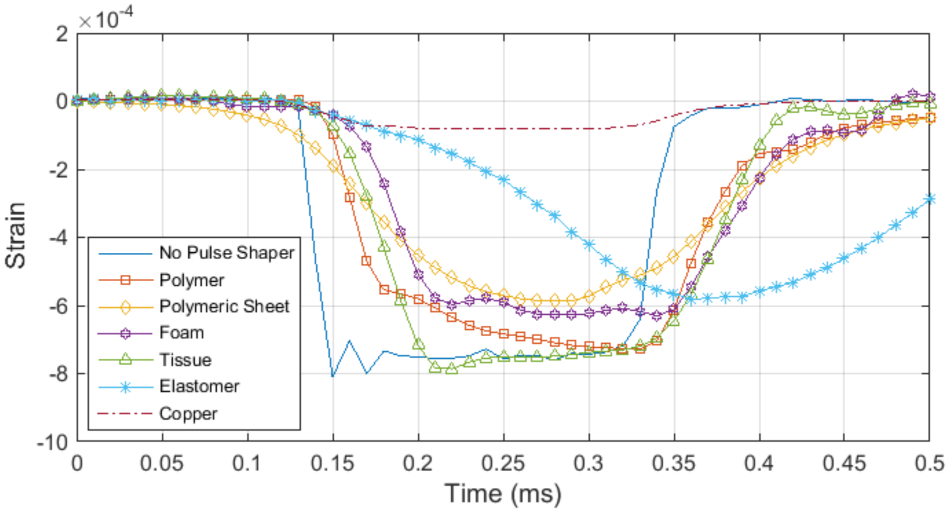

Fig. 4.4 A comparison of pulse profiles generated by different kinds of materials acting as pulse shapers.

To analyse the effect of velocity, a copper pulse shaper with a diameter of 20 *mm* and thickness of 2 *mm* was impacted with velocities ranging from 15 m/s to 100 m/s. The results are illustrated in Fig. 4.7. Fig. 4.8 shows the generated shaped pulse in the incident bar for different striking velocities. The shaped pulse can be generalized into four regions—the initial elastic response of the pulse shaper, followed by the effect of plastic deformation taking place, then the rigid response of the pulse shaper and, lastly, the unloading of the pulse shaper. As the impacting velocity is increased, one notices the increase in amplitude and the rise time of the incident pulse due to plastic deformation in the pulse shaper. When designing a pulse shaper, the velocity corresponding to the initiation of the yield point of the pulse shaper geometry must be determined.

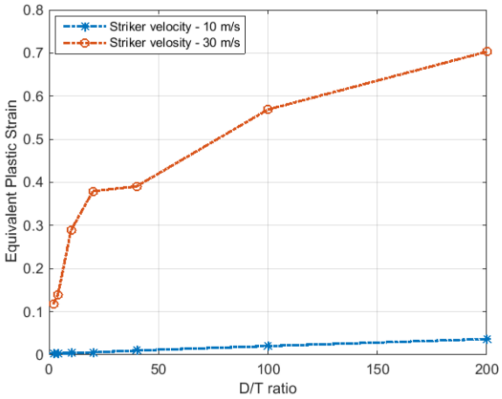

Fig. 4.5 Measure of equivalent plastic strain in pulse shaper for various D/T ratios of pulse shaper, keeping D constant (20mm) at striking velocity of 10 *m/s* and *30 m/s*.

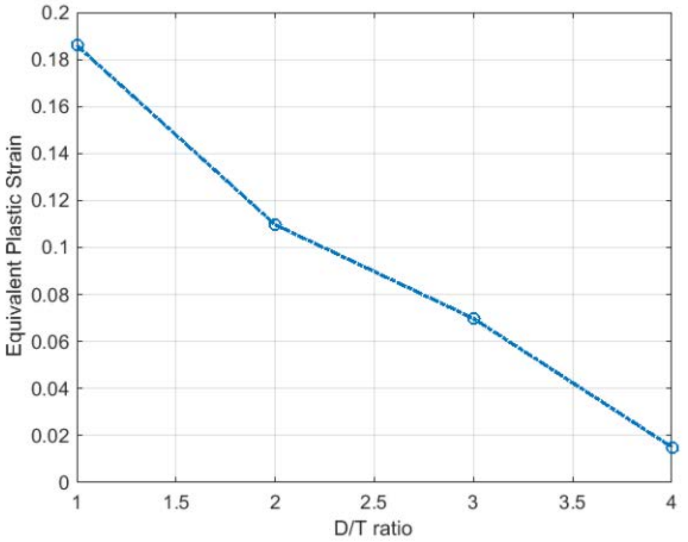

Fig. 4.6 Measure of equivalent plastic strain in pulse shaper for various D/T ratios of pulse shaper, keeping T constant (1*mm*) at a striking velocity of 10 *m/s*.

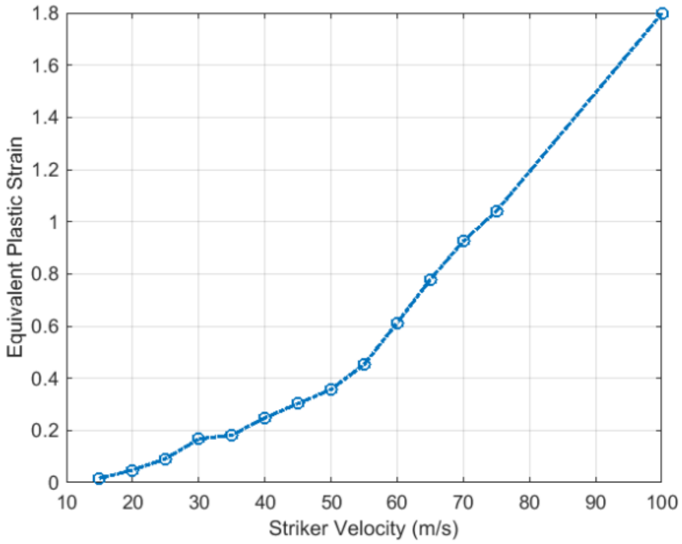

Fig. 4.7 Measure of equivalent plastic strain in pulse shaper at various striking velocities using a copper pulse shaper of diameter 20 *mm* and thickness 1 *mm.*

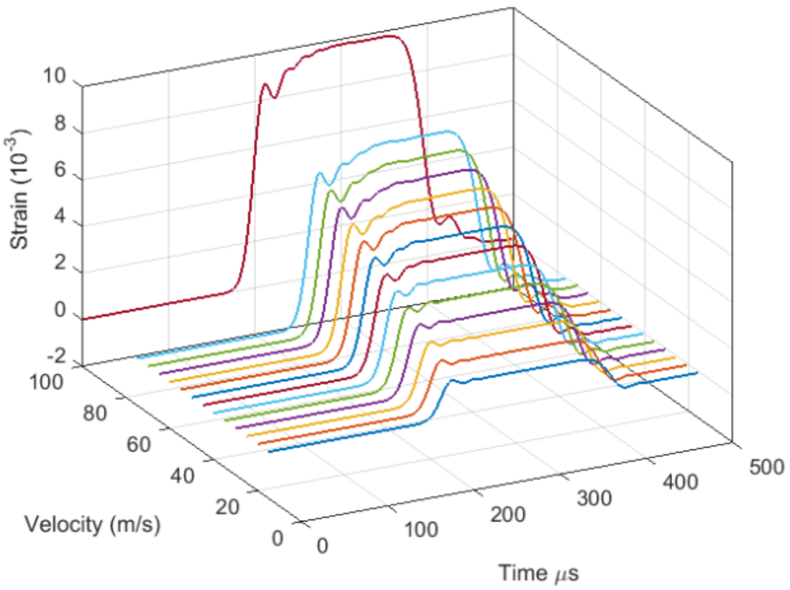

Fig. 4.8 Resultant incident pulses generated from various striking velocities using a pulse shaper of diameter 20 *mm* and thickness 1 *mm*.

Dimensional Analysis

Copper is the most popular choice for the pulse shaping technique, as it is able to generate a loading pulse with an extended rise time and a constant state of stress for most of the loading process. In the previous sections, we described the methodology to model the behaviour of an annealed copper disc (CU11000) when used as the pulse shaper. Fig. 4.9 shows the experimental results and the FEM validation of the pulses generated through a copper disc (thickness of 1.5 *mm* and diameter of 20 *mm*) when impacted at different velocities. It is worth noting that the generated pulses are different both in amplitude and in shape due to the strain rate dependent plastic deformation in copper.

Another challenge is to determine the optimal geometry of the pulse shaper and to analyze the effects of varying geometry sizes on the generated pulse. For this purpose, different geometry sizes were analyzed experimentally. First, the diameter was kept constant and the model was tested with varying thicknesses of the pulse shaper. Fig. 4.10a shows the resultant incident pulse for a copper pulse shaper with varying thicknesses and a diamter of 20 *mm*. Then, the thickness was kept constant at 0.635 *mm*, and different cases were analyzed by varying the diameter (see Fig. 4.10b). It can be noted from Fig. 4.10a that increasing the thickness of the pulse shaper results in a longer rise time and an increased pulse duration. Moreover, the pulse shaper thickness also affects the region of plastic deformation, which is evident when the thickness is increased from 0.635 *mm* to 1.5 *mm*. Similarly, Fig. 4.10b shows that decreasing the diamter results in an increased rise time and a longer duration of the incident pulse with an early start region of plastic deformation. Fig. 4.11 illustrates the FEA results for the stress history of the incident pulse generated by using a hybrid elastomer/copper pulse shaper. The resultant pulse exhibits extended and similar rise and fall times, reaching a constant stress amplitude.

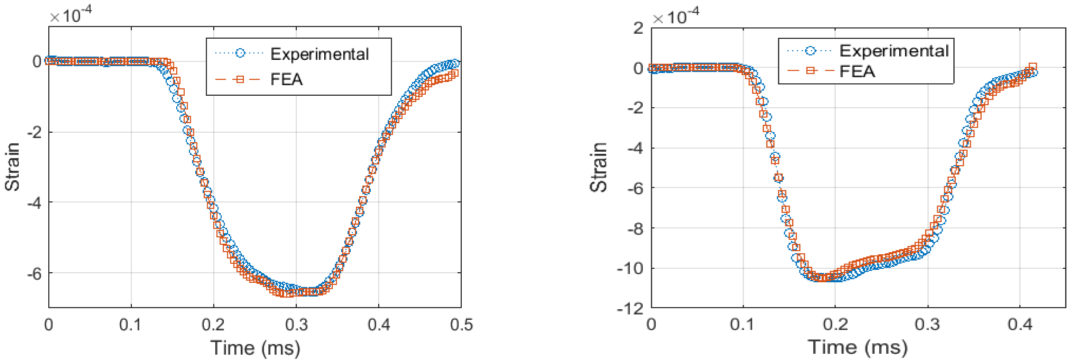

(a) (b)

Fig. 4.9 Experimental and FEM results for the incident pulse generated by a copper pulse shaper under different impact velocities. (a) 6.6 *m/s*; (b) 11.0 *m/s*.

The experimental and numerical results show that the incident pulse shape depends upon the material, the geomtery of the pulse shaper, and the striking velocity of the striker. By optimizing these parameters, an incident pulse suitable for testing elastomers can be generated in a Kolsky bar apparatus. The criteria for an accepabtable pulse shaper are a homogenous stress distribution and a constant rate of deformatiom. Any pulse shaper design is acceptable as long as it fullfills these criteria.

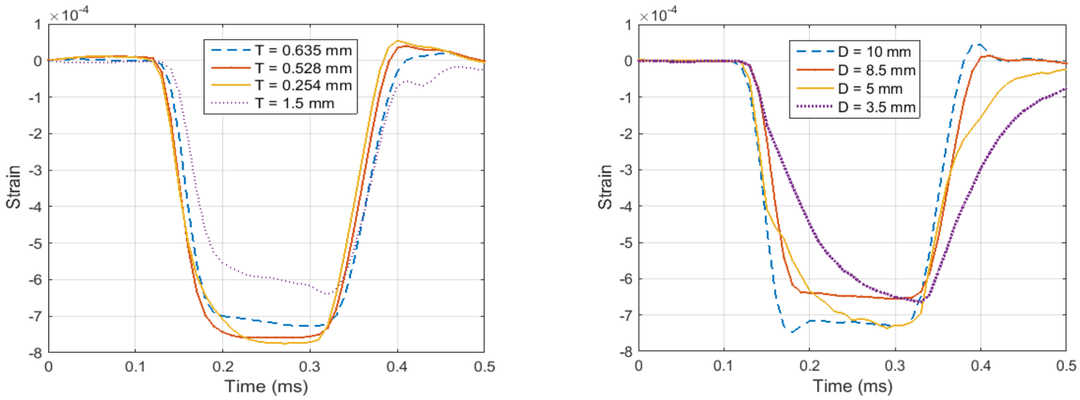

(a) (b)

Fig. 4.10 (a) Incident pulses generated from pulse shapers of various thicknesses with a striking velocity of 7.5 *m/s*; (b) Incident pulses generated from pulse shapers of various diameters with a striking velocity of 7.5 *m/s*.

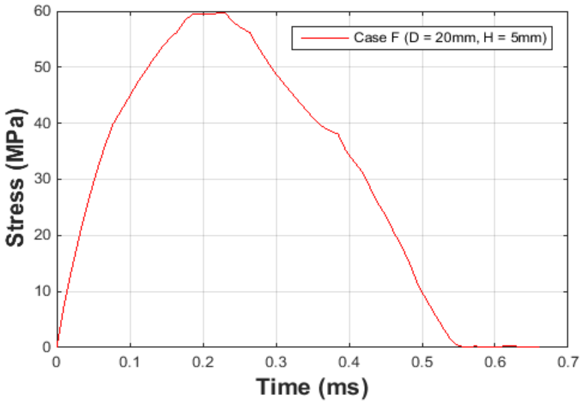

Fig. 4.11 Hybrid copper and elastomeric pulse shaper.

4.2.4 Misalignment Effects

In this section, we study two different kinds of misalignment in the Kolsky bar apparatus. The results are very susceptible to noise if the bars are misaligned. This can produce an inaccurate representation of the sample response. When testing elastomeric samples, a very small amplitude of the loading wave is transmitted to the transmitter bar because of low impedance. If the bars are not properly aligned, this can result in noise in the recorded signal, which can overshadow the sample response. To study this effect, we consider two types of misalignment that are commonly present in the bar system.

The angular difference '*θ*' arises because the incident and the striker bars are not parallel during impact. Secondly, there is a central offset between the striker and the incident bar. Fig. 4.12 shows the variation in the incident pulse when the striker impacts the incident bar at an angle. Similarly, Fig. 4.13 shows the generated incident pulse when the striker hits the incident bar at a delta offset from the neutral axis. The study shows that non-parallel faces of impacting surfaces result in a greater degree of wave dispersion. In this case, the wave is propagated in axial, radial and flexural modes. For the values of θ taken into account, the largest deviation in the expected incident pulse was seen at 10^0. From Fig. 4.12, it can also be noted that the deviation from a perfect incident wave is seen when the value of θ increases by more than 0.5 degrees. Therefore, one can set the limit of *θ* to be no more than 0.5^0 when setting up the Kolsky bar experiment. For the case of axial offset, the maximum limit can be set at 0.5 *mm*. Offsets greater than this value can result in deviation from the expected incident pulse.

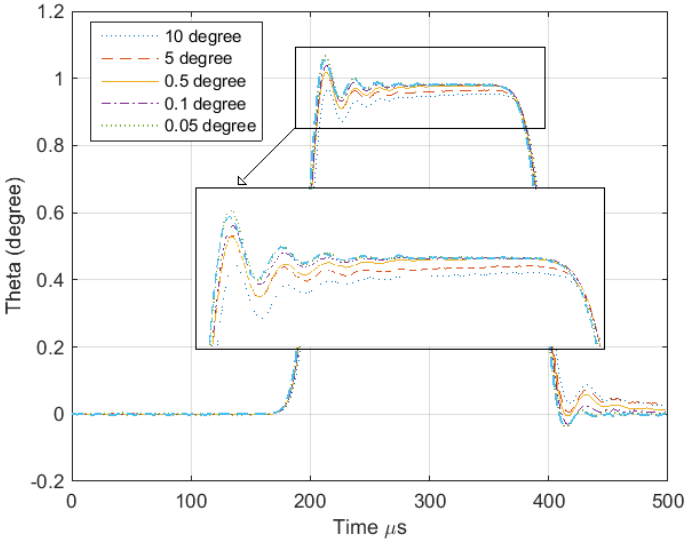

Fig. 4.12 Resultant incident pulse for a non-parallel impacting surface of the incident bar with the striker bar.

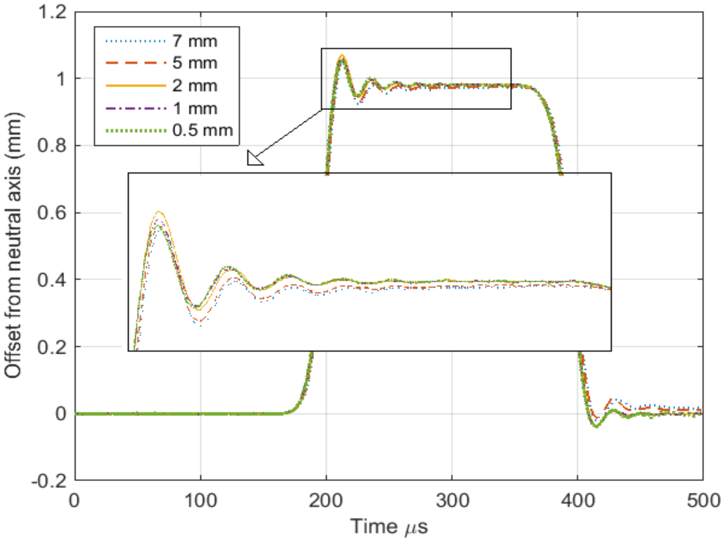

Fig. 4.13 Resultant incident pulse as a result of offset between the incident and the striker bars.

4.2.5 Specimen Geometry Optimization

When conducting Kolsky bar experiments to test elastomers, the most challenging part is to facilitate homogenous deformation in the specimen. The assumption of uniform deformation is not satisfied because of the low speed of elastic waves in elastomers. As a result, a point-wise deformation cannot represent the average deformation of the specimen in the thickness direction. Fig. 4.14 illustrates non-homogenous deformation as the compressive elastic wave travels through the specimen at different points during the loading. The specimen has the same diameter as the bars (20 *mm*), with a thickness of 20 *mm*. At the very beginning of the loading (t = 210 μs), the elastic wave enters the specimen from the right side, and deformation only takes place in the portion in contact with the incident bar. As the time is increased, the deformation moves towards the transmitter/specimen interface (t = 590 μs). The specimen does not attain a state of averaged stress at any time during the loading. This non-uniformity of stress is attributed to axial inertia encountered in impact loadings. The axial inertia also results in radial inertia due to Poisson's effect. This phenomenon is visible in the case of non-uniform deformation captured with a high speed camera and correlated with FE results, as illustrated in Fig. 4.14.

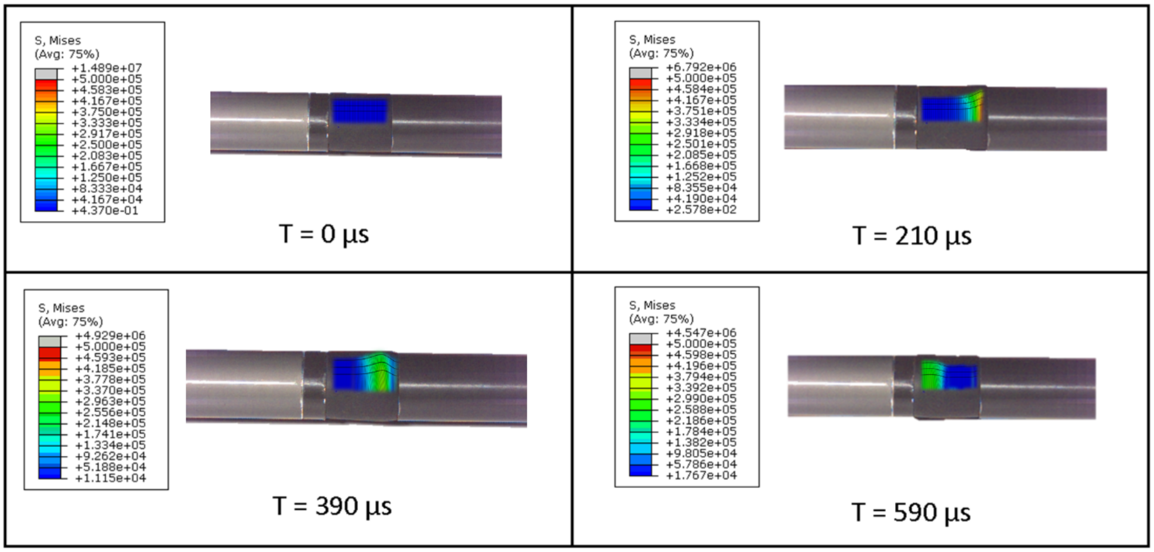

Fig. 4.14 Deformation of a specimen with a thickness of 20 *mm* during the loading, captured through a high speed camera at a frame rate of 100,000 *fps*.

As discussed in the previous sections, the specimen geometry needs to be optimized to ensure homogenous stress distribution in the specimen. To optimize the specimen geometry, several FEA simulations were performed on test specimens with varying diameters and thicknesses. In order to quantify the stress distribution in the test specimen, Eq. 5.20 was used to calculate the ratio *R* which is the ratio of the difference between the stress from either end and the mean stress in the specimen. A Ratio *R* of less than 0.05 is sufficient to consider the specimen in an equilibrated state of stress. *R(t)* was calculated for specimens of various geometries and sizes. At first, the thickness was kept consistent, and various values of the diameter, ranging from 5 *mm* to 20 *mm*, were taken into account. Fig. 4.15 illustrates that the variation in ratio *R* varies throughout the loading time for the specimen with different diameters and a thickness of 1.6 *mm*. It can be noted that all the cases show non-homogenous stress distribution in the initial part of the loading, until the elastic wave travels several times inside the specimen and, eventually, the specimen reaches a state of homogenous stress. It was also inferred from the figure that the specimen with a diameter value of 5 *mm* showed a very high value of *R* in the later part of the loading. It can thus be concluded that achieving equilibrated stress is not dependent on the diameter of the specimen, but very small values less than 8 *mm* can result in non-homogenous stress in the later part of the loading. Therefore, when testing elastomers, a specimen diameter of more than 5 *mm* should be considered.

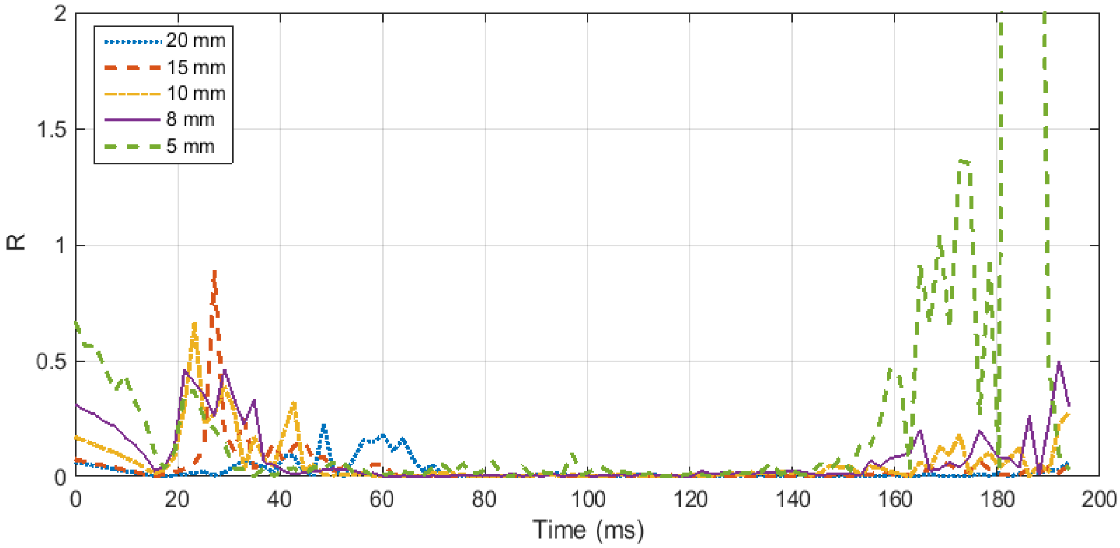

Fig. 4.15 Ratio ‘R’ for specimen thickness of 1.6 *mm* and diameter ranging from 5 *mm* to 20 *mm.*

Next, the same ratio, *R(t)*, was calculated, taking a constant diameter and different thickness values of the specimen into account. For this, different thicknesses ranging from 1 *mm* to 20 *mm* were considered. From the results illustrated in Fig. 4.16, it can be noted that all specimens with a thickness greater than 5 *mm* stay in a non-homogenous state of stress throughout the loading time. Fig. 4.14 shows the deformation of a 20 *mm*-thick specimen during the loading. It can be clearly seen from the stress distribution at different time points during the loading that the specimen fails to achieve a uniform state of stress. This non-uniform state of stress is attributed to the inertial and radial inertia generated. Only the specimens with a thickness equal to or less than 5 *mm* achieved a state of ideal loading. As the thickness of the specimen is decreased, the time-to-equilibrium ratio is decreased and the specimen becomes closer to stress equilibrium with a reduced specimen. However, a very thin specimen may result in interfacial friction.

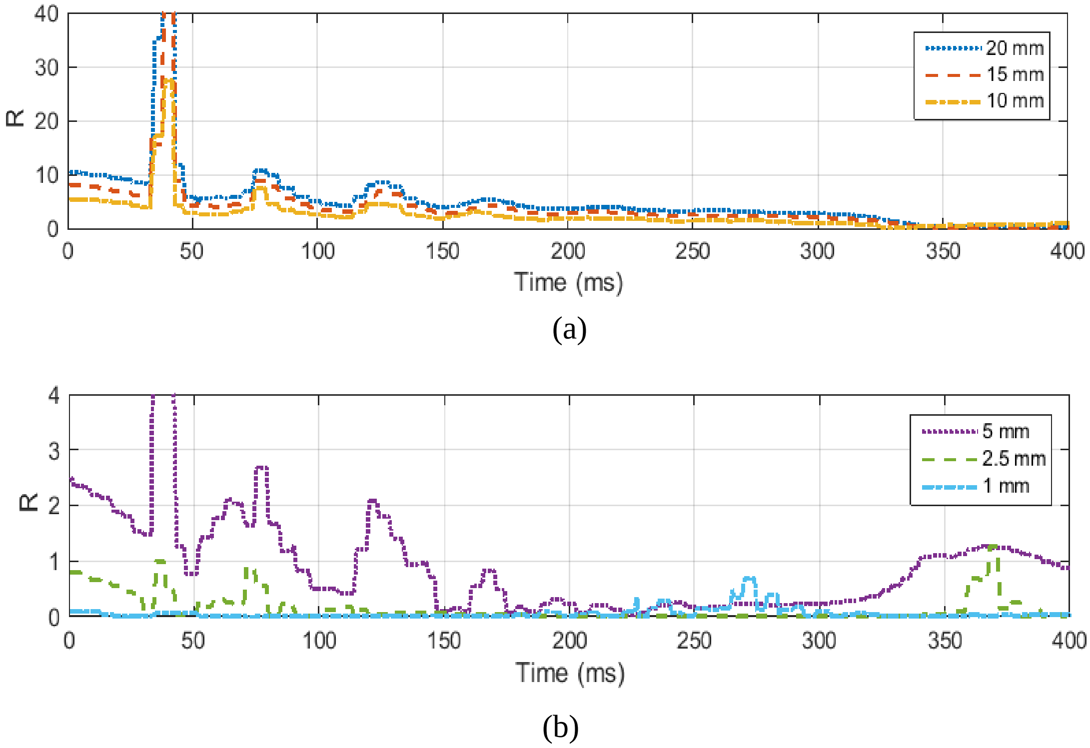

Fig. 4.16 (a) Ratio ‘R’ for specimen diameter 20 *mm* and thickness 20 *mm*, 15 *mm* and 10 *mm*; (b) Ratio ‘R’ for specimen diameter 20 *mm* and thickness 5 *mm*, 2.5 *mm* and 1 *mm*.

Chapter 5 Mechanical Testing of Elastomers

Summary: In this chapter, we describe the mechanical testing procedure used to evaluate the response of elastomers in quasi-static and dynamic strain rate environments. Design considerations and modifications required for the Kolsky bar for testing elastomer material have been discussed in detail. Furthermore, the Kolsky bar design that has been developed as per the requirements is presented.

5.1 Quasi-Static Material Testing

This section describes the standard test performed under quasi-static conditions for uniaxial, biaxial, planar and compression tests. Experimental test data is needed to evaluate the material's parameters which can then be used to model the elastomer's response undergoing multi-axial modes of deformation. For accurate prediction of the material's behaviour, it is necessary that all samples are fabricated from the same batch of materials and tested under constant conditions and rate of loading. The samples were fabricated from sheets of natural rubber and tested using a MTS electromechanical load frame (MTS Criterion 43).

Uniaxial tension tests are carried out on dumbbell specimens (Type V) as specified in ASTM D638 standard under room temperature and pressure. Loading is applied at a constant strain rate of 0.5 */s*. Load and displacement values are then used to calculate the uniaxial stress strain response. Fig. 5.1 illustrates the stress strain response and a sample during a uniaxial test.

Planar tension tests are carried out also at a constant strain rate of 0.5 */s*, on planar type samples with a grip separation of 30 mm and a width of 150 mm. This provides a W/L ratio of 5. It is known that stress strain curves for planar tension are not influenced by aspect ratios ranging between 4 and 10 [55]. Therefore, before testing, the planar sample was first bonded with the fixture plates as a primary source of reinforcement and a secondary reinforcement was applied using nuts and bolts in case the bonding failed. See Fig. 5.2 for the response of a sample under planar type loading.

Simple compression tests are carried out in accordance with test method A as specified in the ASTM D575 standard (standard test methods for rubber properties in compression). A cylindrical sample with a diameter of 28.9 *mm* and a thickness of 12 *mm* is compressed at a strain rate of 0.5 *mm/s* (see Fig. 5.3). Biaxial tension test were conducted at a local material testing facility and the stress-strain results are illustrated in Fig. 5.4. Before commencing the test, it was ensured that the sample and fixture contact surfaces are well lubricated to minimize frictional effects, which may result in non-homogenous deformation of the sample. Displacement and load values are extracted to calculate the stress-strain curves.

Quasi-static tests are conducted at low strain rates and constant speeds. The material’s response under such conditions may not be a true simulation of actual impact conditions because in short-time dynamic events, loading is applied at high rates. Elastomers, being sensitive to the rate of loading applied, respond differently at low and high strain rates. To target dynamic applications, material parameters should be specifically evaluated from the testing conducted under similar conditions and high loading rates. Hence, specialized testing apparatus able to generate such high rates of loading is needed. However, there are no set standards pertaining to material testing at high loading rates. In the next section, we present a design of a Kolsky compression bar testing apparatus developed to test elastomers at high strain rates.

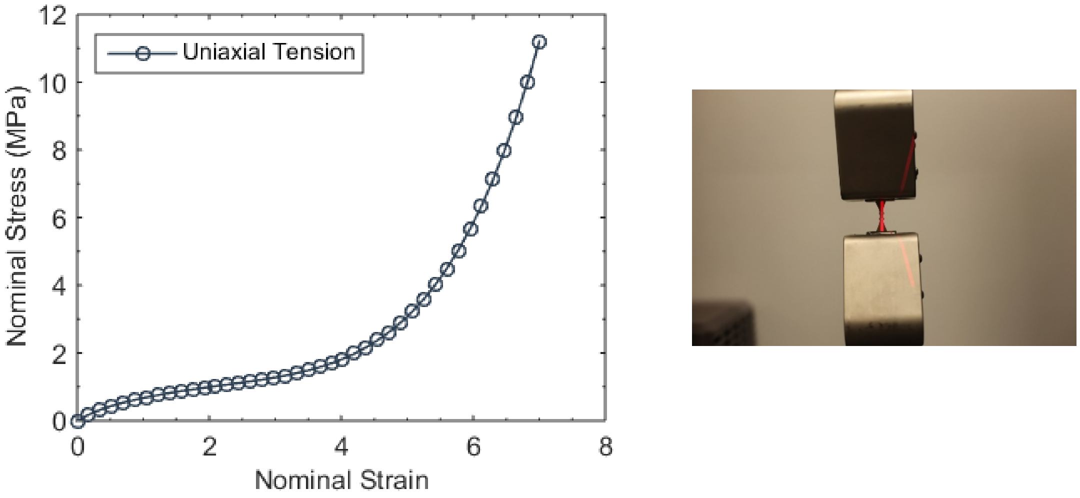

Fig. 5.1 (Left) Stress strain repsonse for uniaxial tension test conducted at test rate of 0.5 /s. (Right) Uniaxial sample during test.

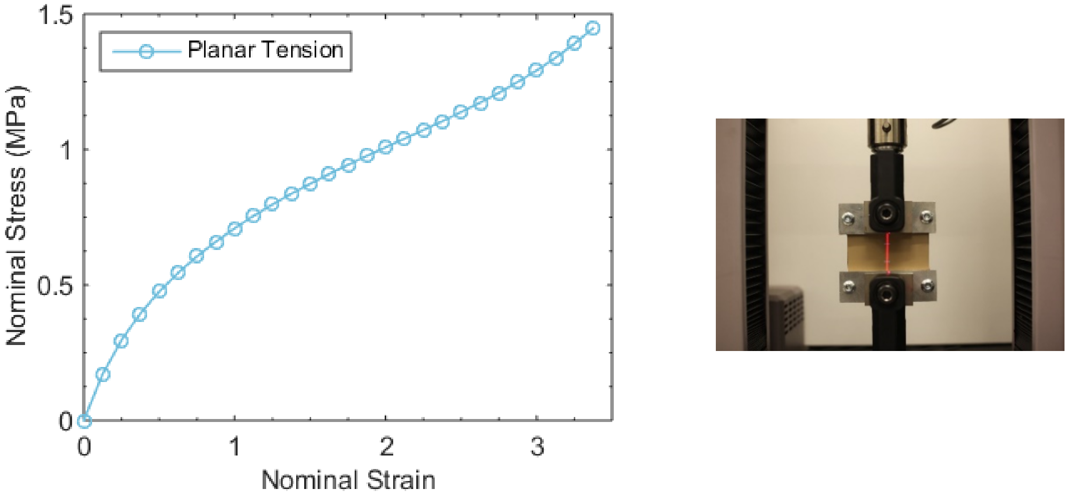

Fig. 5.2 (Left) Stress strain response for a planar test conducted at a test rate of 0.5/s. (Right) Planar sample during the test.

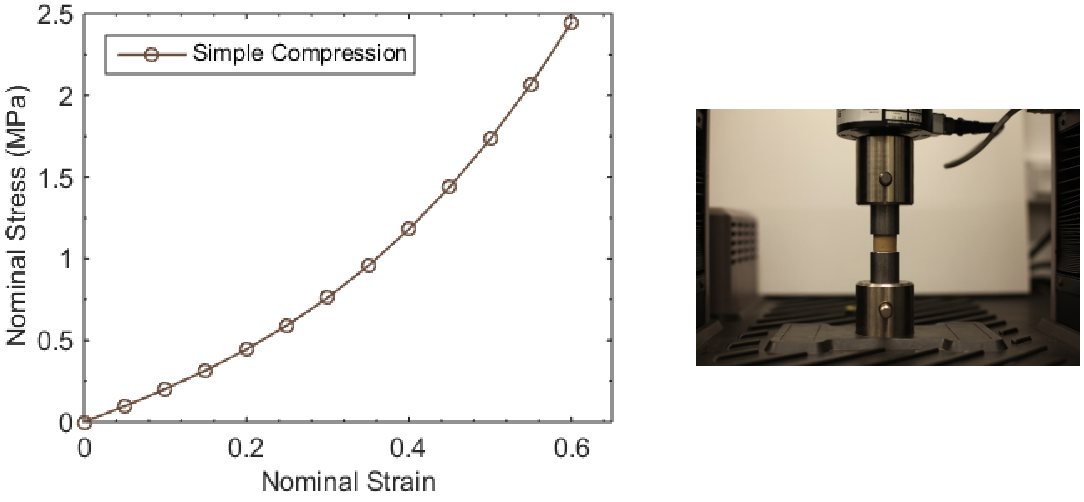

Fig. 5.3 (Left) Stress strain response for compresssion test conducted at a test rate of 0.5/s. (Right) Compression sample during the test

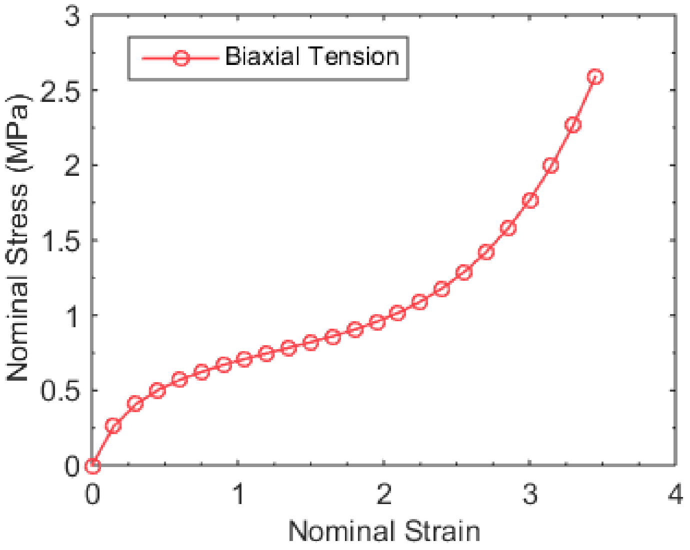

Fig. 5.4 Stress strain response for a biaxial test conducted at a test rate of 0.5/s.

5.2 High Strain Rate Testing of Elastomers

5.2.1 Theory of the Kolsky Bar

The working principle of a Kolsky bar is based on the one dimensional propagation of the compressive wave through the bars. This one dimensional compressive stress wave is related to the velocities that the particles experience at either ends of the specimen by the following equations:

$$v_1 = C_b(\varepsilon_i - \varepsilon_r) \tag{5.1}$$

$$v_2 = C_b(\varepsilon_t) \tag{5.2}$$

where ε_i, ε_r, ε_t , are the measured strain pulses recorded from the strain gages. C_b is the elastic wave speed of the bar material. Using these equations, the average engineering strain integrated over the pulse duration t in a specimen having length L_s is given as:

$$\varepsilon = \int_0^t \frac{(v_1 - v_2)}{L_s} dt = \frac{C_b}{L_s} \int_0^t (\varepsilon_i - \varepsilon_r - \varepsilon_t) dt \tag{5.3}$$

And the stresses at both of the interfaces of the specimen can be determined from:

$$\sigma_1 = \frac{A_b}{A_s} E_b(\varepsilon_i + \varepsilon_r) \tag{5.4}$$

$$\sigma_2 = \frac{A_b}{A_s} E_b \varepsilon_t \tag{5.5}$$

where, A_b and A_s are the bar and specimen cross section area and E_b is the Young's Modulus. One of the assumptions that is made while determining the stress-strain response, is that the specimen is in a state of equilibrated stress ($\sigma_1 = \sigma_2$). Making this assumption we can arrive at the following conclusion:

$$\varepsilon_r + \varepsilon_i = \varepsilon_t \tag{5.6}$$

Thus, Eq. 5.3 and Eq. 5.4 can be solved to yield the strain rate, strain and stress profile in the specimen.

$$\sigma = \frac{A_b}{A_s} . E_b \varepsilon_t \tag{5.7}$$

$$\dot{\varepsilon} = -2 \frac{C_b}{L_s} \varepsilon_r \tag{5.8}$$

$$\varepsilon(t) = -2 \frac{C_b}{L_s} \int_0^t \varepsilon_r \, dt \tag{5.9}$$

5.2.2 General Design of a Kolsky Bar

The design of the Kolsky bar apparatus is dependent on the choice of the specimen size and the maximum desired strain rate. The strain in the incident pulse can be determined by the impact velocity of the striker by the following relation:

$$\varepsilon_i = \frac{V}{2C_B} \tag{5.14}$$

where, V denotes the striker impact velocity. Using the stress equilibrium assumption on both surfaces of the specimen and by substituting Eq. 5.14 and Eq. 5.8 into Eq. 5.7, the overall specimen characteristic response equation is found:

$$\sigma_s = E_b \left(\frac{A_b}{A_s}\right)\left(\frac{V}{2C_b}\right) - E_b \left(\frac{A_b}{A_s}\right)\left(\frac{L_s}{2C_b}\right)\dot{\varepsilon}_s \tag{5.15}$$

The relation given in Eq. 5.15 relates the maximum attainable stress in the specimen as a function of strain and striking velocity. A particular striking velocity is chosen to achieve the desired strain rate Eq. 5.16 and stress Eq. 5.17:

$$\dot{\varepsilon}_{s(max)} = \frac{V}{L_s} \tag{5.16}$$

$$\sigma_s = E_b \left(\frac{A_b}{A_s}\right)\left(\frac{V}{2C_b}\right) \tag{5.17}$$

Higher levels of stress can be achieved by increasing the impact velocity or by increasing the area mismatch A_b/As. And similarly reducing specimen length and increasing the impact velocity would increase the maximum attainable strain rate.

When choosing the bar and specimen dimensions, certain design requirement have to be met for a valid Kolsky bar. A L_b/D_b ratio of at least 20 is required to allow one-dimensional wave propagation. Typically this ratio is in on the order of 100 [56]. The diameter of the bar should be around 2 to 4 times the diameter of the specimen. Choosing a large ratio for D_b/D_s is ideal to achieve high stress. This ratio should be kept such that the bar surface does not act like a plane for the specimen. The L_s/D_s ratio is usually selected between 0.6 and 1 [22]; this *Ls/Ds* ratio also depends on the type of material being tested. Soft materials have shown dependency on the length of the specimen which could result in axial and radial inertia. Thus, the striker bar is made up of the same material and diameter as of the incident and transmitter bars to avoid wave dispersion.

5.2.3 Kolsky Bar Testing For Low Impedance Materials

Uniform Deformation and Inertial Effects

When designing a Kolsky bar for soft materials, some considerations have to be taken into account. As discussed in the previous section, the measurements are based on the assumption of uniform deformation in the specimen. Due to the low strength, stiffness and acoustic impedance of soft materials, their mechanical response depends upon the compressive stress wave profile. The low wave speed in a specimen causes it to take non-zero time to achieve stress equilibration. The specimen can be considered to be in a state of stress equilibrium by allowing several reverberations of the stress wave inside the specimen. It requires almost thrice the amount of time taken for the wave to pass the specimen to achieve stress equilibrium [58]. The time for a one-way trip of a stress wave through the specimen can be calculated using the following equation:

$$T = \frac{L_s}{C_s} \tag{5.18}$$

where, L_s is the length of the specimen and C_s is the characteristic elastic wave velocity. As it can be seen from Eq. 5.18 the length of the specimen is the most important variable in achieving a uniform state of stress in the specimen. Reducing the length of the specimen would help achieve a state of stress equilibrium quickly, but on the contrary it has been observed that a small value of L_s could result in increased frictional effects between the specimen bar interfaces, creating distortion in the recorded signal. The non-uniform deformation also results in the axial and radial inertia which is evident when testing very soft materials like elastomeric foams and gels. The inertial and radial effect due to impact loading is studied in detail by Song *et al* 2007 [59]. They investigated that this radial inertia is not only dependent on the loading conditions, but also on the specimen geometry and density. These effects cannot be ignored when optimizing the specimen dimensions.

In addition, high strain rates can also produce inertia-induced stress, especially when the specimen is going through large deformation. This inertia induced stress can greatly affect the strain profiles recorded by the strain gauges [59].

Low Transmitted Signals

Another problem associated with testing softer materials using the Kolsky bar experiment is the very low amplitude of the transmitted pulse [31]. Because of the impedance mismatch between the specimen and bar material, almost the entire stress wave is reflected back and only a very small portion of it is transmitted. This weak signal becomes difficult to measure by regular strain sensors and more responsive and sensitive strain gages are required. One of the ways to address this problem is to use low impedance bars, such as polymer bars. Using polymer bars allows for greater wave dispersion and spectral analysis techniques are required to filter out the dispersion effect. Another technique of using a hollow transmitter bar also helps increase the amplitude of the transmitted signal up to several times [57].

Loading Profile

Elastomers also show dependency on the applied strain rate, generating different stress-strain responses for different loading rates. Therefore, when testing elastomers, care must be taken to ensure that the stress pulse profile is achieved at a constant strain rate with low rates of initial loading. A low initial rate of loading is required because the acceleration induced inertia is inevitable in the initial period of loading, when reaching a particular strain rate. A common way of avoiding this acceleration induced inertia is a constant loading pulse with extended rise time.

Specimen Size effect

The specimen size needs to be properly optimized to mitigate the effects of associated radial and axial inertial effects, achieving uniform deformation and attaining the desired strain rate. The specimen diameter has to be smaller than the bar diameters. Upon the assumption that the maximum diameter during deformation does not exceed the bar diameter under the desirable strain, the required diameter for the specimen can be calculated by Eq. 5.19 given below:

$$D_s = D_b\sqrt{1-\varepsilon} \tag{5.19}$$

For example, with a bar diameter of 20 *mm* and specimen diameter of 8 *mm* the maximum engineering strain that can be achieved is 0.7. After the selection of the specimen diameter, the appropriate length of the specimen can be selected, keeping in mind the dependency of inertial effect and the stress equilibration on the length of the specimen. Thinning the specimen helps in achieving a state of equilibrated stress quicker, but also produces visible frictional effects [61].

A specimen can be considered to be in equilibrated stress by comparing the stress profiles on both faces of the specimen. Previous researchers have determined that equilibrium is reached if the ratio of the difference between the stress from either end ‘$\Delta\sigma$’ and the mean stress in the specimen ‘σ_m’ is less than 0.05 [62].

$$R(t) = \left|\frac{\Delta\sigma}{\sigma_m}\right| \leq 0.05 \tag{5.20}$$

Song *et al* 2004 [61] investigated that a thin specimen maybe one of the requirements in a Kolsky bar experiment, but it is not sufficient to achieve equilibrium. Specimen design can also help avoid inertia in the radial direction. It was also investigated that this inertia is maximum at the centre and diminishes at the edges. So using a hollow specimen could also help address the problem [57].

5.2.4 Kolsky Bar Design and Setup

This section describes the guidelines for designing a modified Kolsky bar apparatus to characterize the behaviour of elastomer when subjected to high strain rates between 10^2 s^{-1} and 10^4 s^{-1}. For the experimental design of the Kolsky bar apparatus the specimen geometry was optimized to be D_s = 8 *mm* and L_s = 1.6 *mm*. The length and the diameter of the bars are L_b = 2000 *mm* and D_b = 20 *mm*. The selected values satisfy the design parameter ratios that were discussed in the Section 5.2.2. We get L_b/D_b = 100, D_b/D_s = 2.5 and L_s/D_s = 0.2. It can be noted that the L_s/D_s ratio is different than what was discussed in the previous section (between 0.6 - 1). The specimen geometry was optimized carefully by taking into account the effect of L_s on the uniform deformation, and equilibration of stress as discussed in the previous section. Using Eq. 5.19, the choice of D_b and D_s could achieve a strain level of up to 0.8. The striker diameter, D_{st}, is kept equal to the incident and the transmitter rods to avoid wave dispersions. The length of the striker is L_{st} = 500 *mm*. A Relatively longer L_{st} is to account for stress equilibration, as the loading pulse duration needs to be 3 times longer than the time it takes the wave to travel back and forth inside the specimen. By using the relation for the period of a loading wave$T = \frac{2L_{st}}{C_b}$, it can be seen that the choice of L_{st} would generate a loading pulse of duration 200 μs, which is more than enough for the specimen to attain uniform stress distribution and respond according to it.

From the available choices for the bar material, Aluminium 6061 Anodized (Igus®) was selected. It is apparent from Eq. 5.7 that to increase the transmitted strain, either Young's modulus, E_b, or A_b/A_s must be reduced. This is the main reason for choosing Aluminium as the bar material rather than other higher strength material bars that are reportedly used before in Kolsky setups. Another option for the bar material is polymeric bars. The use of these low strength bars provides a sufficiently high signal-to-noise ratio but this low impedance mismatch between the specimen and bar will delay the dynamic equilibrium process. Moreover, the use of polymeric bars also increases wave dispersion and attenuation. It is recommended that the striker, transmitter and incident bar are made up of the same material. The impedance mismatch causes the transmitted wave to be very weak. To address this problem a hollow transmitter bar was chosen. As demonstrated by *Chen* (1998) [57], hollow transmitter bars can be used to increase the amplitude of the transmitted wave. When using hollow bars, a modification needs to be made in Eq. 5.19. Accounting for the change in the cross-sectional area of the bars with the use of a hollow transmission bar, *Chen* formulated this relation to be:

$$\varepsilon = \frac{C_b}{L}\left(1 - \frac{A_h}{A_b}\right)\int_0^t \varepsilon_i dt - \frac{C_b}{L}\left(1 + \frac{A_h}{A_b}\right)\int_0^t \varepsilon_r dt \tag{5.21}$$

To ensure uniform deformation, a pulse shaping technique is adopted. A pulse shaper is attached in between the incident and striker bar so that it directly impacts the surface. Control and smoothness of the loading pulse can be achieved by using a pulse shaper as it absorbs the high frequency components of the pulse. Different choices of pulse shapers are used by researchers, such as polymer disks [57], brass [58], copper disks [59] [23] [60] [28] and tissue paper. Different geometries of pulse shapers can be tested to generate the desired pulse profile.

Another very important modification made to ensure the specimen achieves a state of stress equilibrium is to use Piezoelectric Quartz crystals as force transducers on either side of the specimen bar interface. Quartz crystals are chosen as force transducers because of the similar impedance of quartz and aluminium. Quartz crystals have been used in the Kolsky bar setup by Chen *et al* (1999) [61] to measure the relatively weak signal, by sandwiching the crystal in the middle of the transmitter bar, to measure the weak signals. These quartz crystals, functioning as force transducers, can also be attached to either side of the specimen to record the force profile. This force profile can be analysed to ensure the stress equilibrium condition in the specimen Eq. 5.20, which is one of the requirements for a valid Kolsky bar experiment [67]. *Casem et al* (2005) thoroughly studied the inertial effects of quartz transducers in a Kolsky bar [62]. *Casem* reported that using a single quartz crystal could induce inertial effects and instead three quartz crystals should be used to reduce this effect by a factor of 50.

The specimen is placed between the lubricated ends of the bar using a round collar to ensure alignment with the central axis of the metallic bars. The bars are gently pushed against the specimen and the collar is taken off. To record the strain profile from the bars, semiconductor strain gauges are recommended over a foil gauge. Semiconductor strain gauges have a gauge factor of 140 which is approximately 70 times larger than the foil gauges. Highly sensitive semi-conductor gauges are needed to measure the very weak transmitted signals.

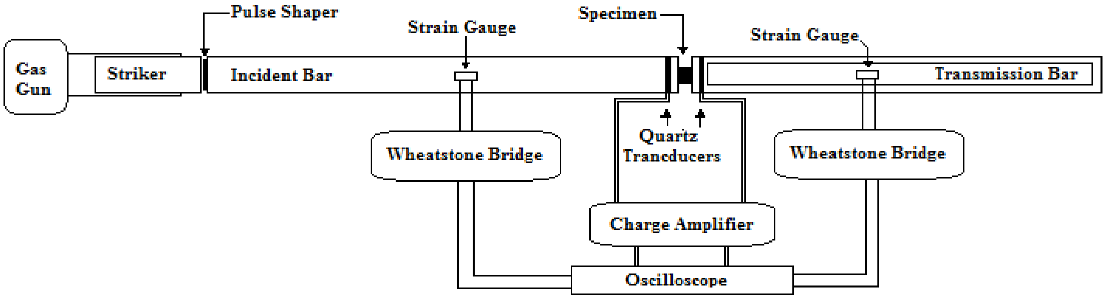

Fig. 5.5 Schematic of the Kolsky compression bar.

A very important constraint in successfully conducting the Kolsky bar experiment is the alignment of bars. It is known that misalignment could cause distortion in the recorded signal which in some cases cannot be differentiated from the actual strain signals. Because the goal is to record strain at micro levels, caution must be taken when setting up the apparatus. Kareem *et al* (2012) has investigated in detail and quantified the effect of misalignment on the recorded stress strain response of the specimen. It was experimentally verified that in order to minimize this distortion, the offset of the bars must be less than 0.08 *mm* per 205 *m*, centreless grinded to a target diameter with tolerance of ± 0.025 *mm* and finally perfectly perpendicular lubricated end face with tolerance of ± 0.03 degrees.

Gas-Gun Setup

As discussed before, the maximum achievable strain rate depends upon the impact velocity of the striker. The most common way of accelerating the striker is by using a compressed gas gun. The proposed design of the gas gun is a two-staged gas gun. The main supply of high pressure gas or a compressor is used to fill the reservoir. For the reservoir, a 1 *L* sampling cylinder with a pressure rating of up to 3000 *psi* was selected. Pressure is released using a solenoid valve, with a pressure rating of 750 *psi*. As the velocity of the striker depends upon the initial gas pressure, choosing a high pressure reservoir would generate a wide range of velocities in the striker. Having control over a wide range of velocities is also needed because the striking velocity relates to the strain rate achieved in the specimen. Using this system, it was calculated that the striker could be accelerated to speeds of up to 80 *m/s* upon exiting the barrel.

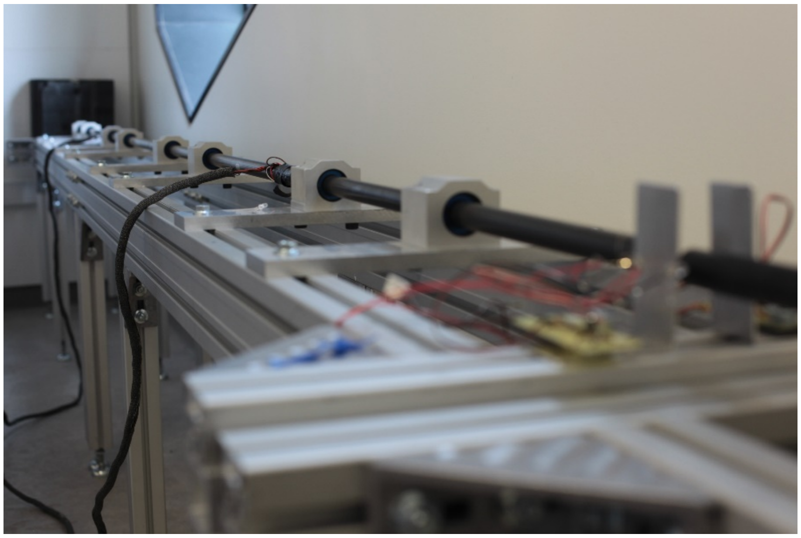

Fig. 5.6 Developed Kolsky bar for testing of elastomers

Calibration of the Kolsky Bar

Before the Kolsky bar is used to test a material at dynamic loading, it requires calibration. The purpose of calibration is to ensure the accurate setup of the apparatus and alignment of the bars. To verify alignment of the bars, the striker is launched on to the incident bar, without placing the specimen in between. A good alignment between the striker and incident bar would produce a trapezoidal pulse with no distortion in the signal and an amplitude which could be calculated analytically by using Eq. 5.14. Distortion in the signal is indicated by spikes in the baseline signal. After ensuring a good alignment between the bars, quantitative measurement can be made to calculate the elastic wave speed in the bar material. This is done by noting the time difference between the incident and the reflected pulse and using the relation: $C_b = 2l_{sg}/\Delta t$, where l_{sg} is the distance between the location of the strain gauge and the specimen end of the incident bar. The time difference between the two pulses in Fig. 5.7 was found to be 480 μ*s* and l_{sg} was 1250 mm. The value of C_b was calculated to be approximately 5200 m/s.

Fig. 5.7 illustrates the experimental and FEA results when the striker is launched with a velocity of 7.5 *m/s*. It can be noted from Fig. 5.7 that the amplitude of the incident wave is 0.75x10^{-4} strain. This can be confirmed using Eq. 5.14. The time period of the loading pulse can be calculated using the relation; $T = 2L_{st}/C_b$, which is calculated to be approximately 200 μs. Additionally, Fig. 5.7 show a very close agreement between the experimental and FEA results, meaning the test setup is well aligned and ready to produce dynamic loadings in the test specimen. The input file for the FEM calibration model can be found in Appendix-A.

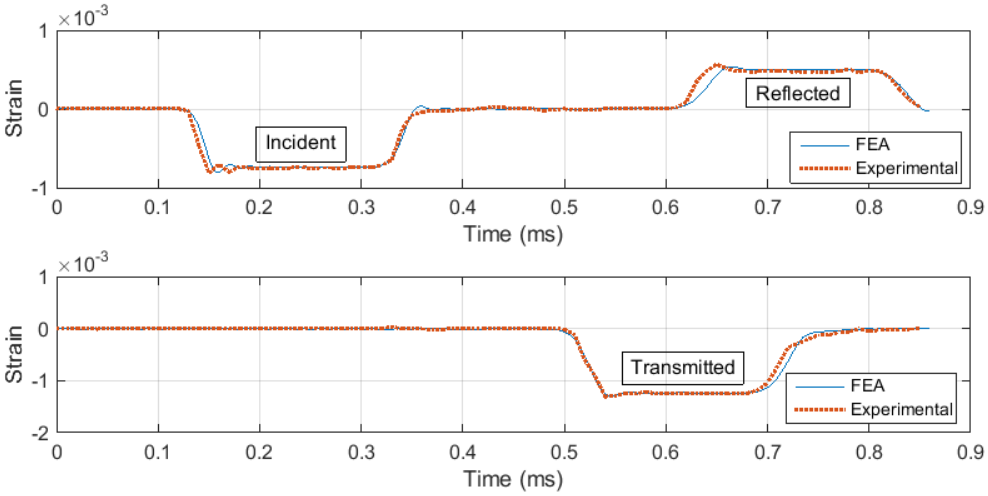

Fig. 5.7 Experimental and FEM calibration.

5.2.5 High Strain Rate Response of NBR

In this section we present Kolsky compression bar experiments performed on nitrile butadiene rubber (NBR) . The material came in the form of sheets 2.4 *mm* thick from which cylindrical specimen of diameter 8.5 *mm* were cut. Fig. 5.8 shows the incident, reflected and transmitted pulses in a Kolsky bar experiment performed at a strain rate of 3000 s^{-1}

under room temperature and pressure. An annealed copper disk (CU11000) was employed as the pulse shaper to characterize NBR specimens. The dimensions of the pulse shaper were selected to be 8.5 *mm* in diameter and 0.635 mm in thickness. This resulted in an incident pulse with an extended rise time that was long enough for the specimen to attain stress equilibrium and a constant strain rate of deformation for most part of the loading. Fig. 5.9 illustrates the incident pulses generated at different strain rates ranging from 3000 s^{-1} to 6500 s^{-1}.

The incident and reflected pulses were used to compute the strain history in the test specimen using Eq. 5.21 and the stress history was computed using Eq. 5.7. Fig. 5.10 illustrates the engineering strain versus stress curves for different dynamic strain rates varying between 3000 s^{-1} to 6500 s^{-1}. The response of the test specimen showed significant strain rate effects while exhibiting a similar trend in curves. The typical characteristics exhibited in the test sample includes a near linear behaviour at small strains followed by a nonlinear transition towards a strain hardening region and, lastly, the unloading of the specimen which is typical in rubber samples. During the unloading of the specimen, the viscoelastic characteristics of elastomers assist recovery of the sample with a very small stress amplitude.

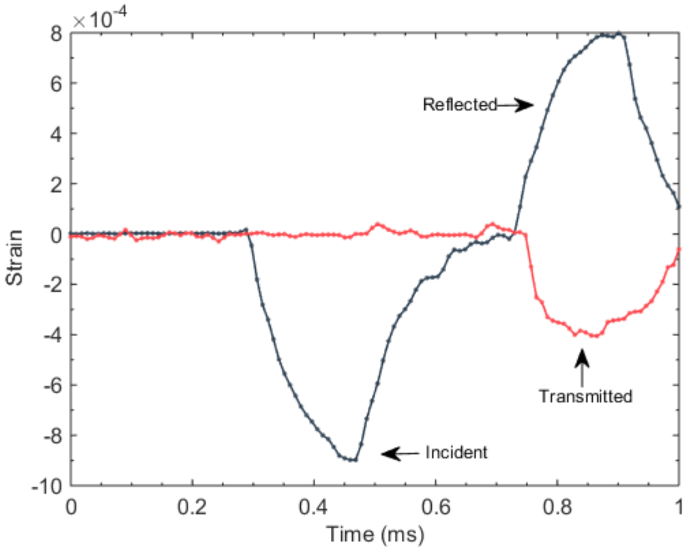

Fig. 5.8 Incident, reflected and transmitted pulses in a Kolsky bar experiment for NBR.

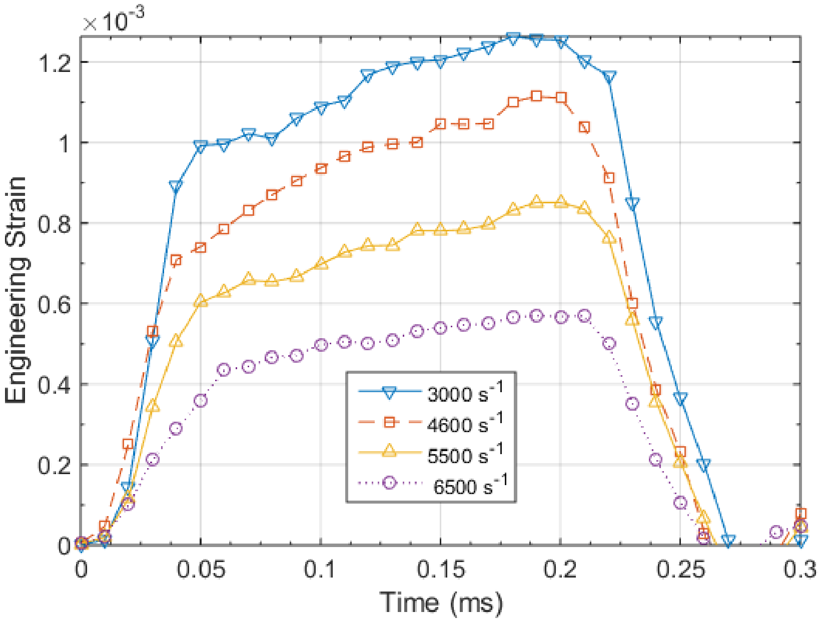

Fig. 5.9 Incident pulses at different strain rates.

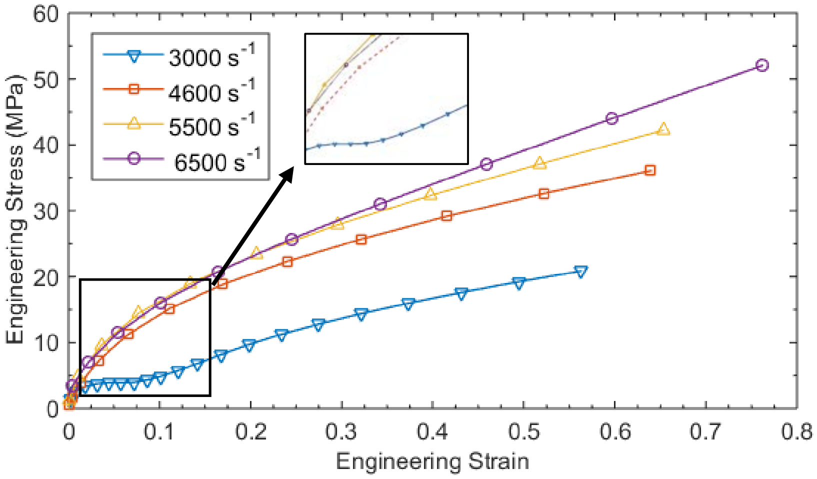

Fig. 5.10 Compressive stress strain curves for NBR at different strain rates.

Chapter 6 Case Studies

Summary: In this chapter, the methodology developed to test and characterize the response of elastomers under high-strain rate loading conditions using a modified Kolsky bar testing apparatus is employed to study two unique engineering materials. Firstly, we investigate the response of carbon nanotube-reinforced elastomers made using traditional manufacturing techniques. In the second application, we characterize a traditional and commonly used class of elastomers that was manufactured using new and emerging 3D printing techniques.

6.1 Effect of Nano Reinforcement in Engineered Elastomers at High Strain Rate

In this study, we investigate the response of nanoparticle reinforced elastomer composites under dynamic impact. The preparation, characterization and testing methodology of polydimethylsiloxane based elastomers reinforced with multi-walled carbon nanotubes is discussed in detail. Under quasi-static conditions, the presence of a CNT network resulted in an enhanced stiffness. When subjected to high strain rates under compressive loading the presence of CNTs influenced the stress – strain curve characteristics (e.g. the transition point from the strain hardening to softening regions) while greatly improving the energy storing capabilities of elastomer. To test under high strain rates, some necessary modifications were also made to the dynamic testing apparatus (Kolsky bar/Split Hopkinson bar).

6.1.1 Introduction

Elastomers are rubber-like materials exhibiting characteristics of viscoelastic nature, low elastic modulus, high strain at failure and weak inter-molecular interactions. Quite recently considerable attention has been devoted to developing multi-dimensional composite systems by introducing a nano-filler network. Some typical reinforcing fillers include cubic and spheroidal fillers (calcium carbonate, silica, carbon black), fibre fillers (glass, aramid fibres) and nanofillers (carbon nanotubes, nanoclays, nanosilica) [71]. Depending on their structural and geometric characteristics, nano-filler networks interacts with the polymer matrix differently, resulting in enhanced mechanical and electrical properties of the resulting composite system. The use of Carbon nanotubes to fabricate elastomer based composites has gained importance due to their high Young's modulus, superior electrical and thermal conductivity and large aspect ratio. These elastomeric nanocomposites, however, require a preparation procedure that is different than most polymer-based nanocomposites since their performance greatly depends on the rate of dispersion, and degree of alignment.

It is quite evident and well established that incorporating CNTs into an elastomer network improves stiffness over a large range of strain deformations. However, under moderate to high strain rates, the response of elastomers can vary from being purely rubber-like to exhibiting glassy behaviour [72]. Investigations on the performance of this reinforcement when subjected to high strain rates are still lacking. The main objective of this research is to characterise the effect of CNT filler loading on the stiffening of the elastomeric composite under quasi-static and dynamic impact conditions. The typical setup required to study the response of materials under impact is the Split Hopkinson bar/Kolsky bar. However, to test low impedance, and low strength materials, some modifications to the Kolsky bar are required.

6.1.2 Experimental Procedure

Fabrication

To fabricate the matrix network polydimethylsiloxane (PDMS) base (DOW SYLGARD 184) was used in a 10:1 ratio with a HR-C catalyst. First, the PDMS base was extensively mixed with multi-walled carbon nanotubes MWCNT (NC7000) having an average diameter and length of 9.5 *nm* and 1.5 *µm,* respectively. To achieve better dispersion of CNTs the solution was sonicated for 30 mins. After the addition of a catalyst, the CNT/PDMS solution was further mixed in a mechanical stirrer and degassed in a vacuum chamber (see Fig. 6.1). Before it was ready to be cured at 150 ^{o}C for 15 *mins,* the resulting paste was poured into a mold and vacuum bagged to ensure the removal of tiny air bubbles that may have been captured during the transfer to the mold. To characterize the stiffening effect due to the presence of a filler network, the CNT were added in varying weight percent (*% wt*) with the elastomer base.

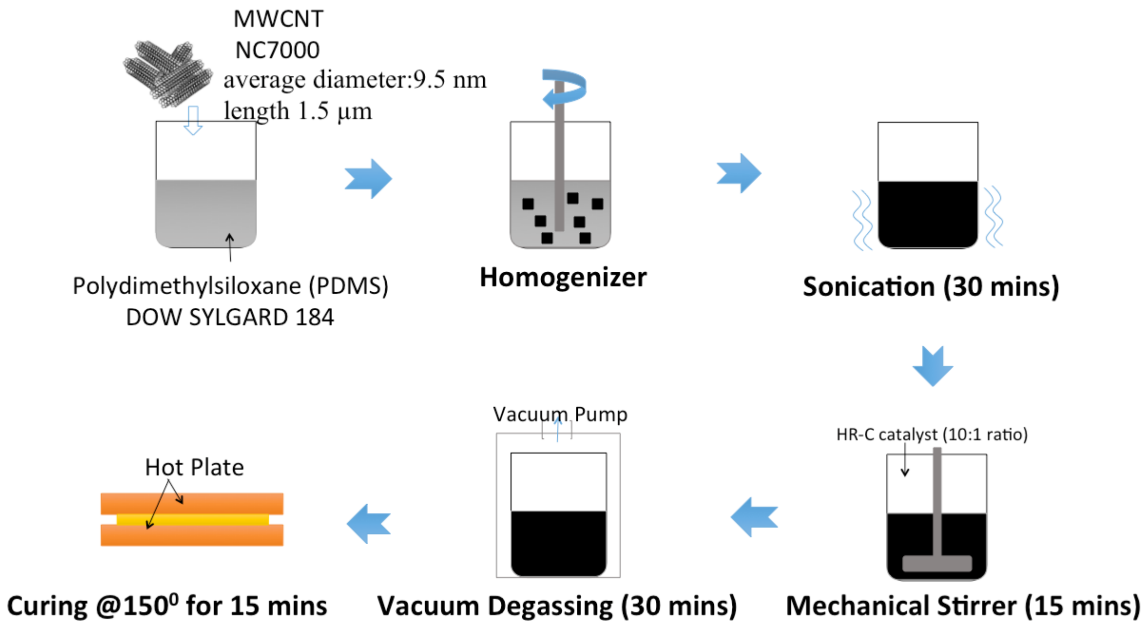

Fig. 6.1 Fabircation process for PDMS/CNT elastomer compistes.

Testing

Uniaxial tension tests were carried out in a MTS-43 electromechanical load frame using a dumbbell specimen with a thickness of 3.3 *mm* and width of 5.5 *mm* at a loading rate of 0.1 *mm/s*. For the dynamic impact test, a modified Kolsky bar was developed suitable to test low impedance soft materials, like rubbers was developed. In a Kolsky bar, a cylindrical sample is a sandwiched between an incident and transmission wave. Dynamic loading is produced in the form of an elastic wave when the incident bar is impacted using a striker of the same diameter. This is called the incident wave, upon reaching the bar specimen interface some of this wave is reflected back while the rest is transmitted through the specimen to the transmission bar. The incident, reflected and transmitted waves are recorded through strain gauges, to compute the response of the specimen. To avoid interfacial friction and inertial effects which may result in noise, the specimen geometry was optimized to be *8.5 mm* diameter and *2 mm* thickness. The trapezoidal incident wave was also shaped using pulse shaping techniques into a smoother pulse with an elongated rise time to avoid the effects of axial and radial inertia. The geometry of the pulse shaper (annealed C11000) was optimized to be cylindrical with a diameter of 3.5 *mm* and thickness of 1.6 *mm*. The incident and hollow transmission bars were 20 *mm* in diameter, and had a length of 2 *m* and 1.8 *m* respectively. The complete operational details of the testing apparatus can be found in references [57] and [73]. For each category 5 samples were fabricated and mechanically tested under quasi-static and dynamic loading.

6.1.3 Results and Discussion

Fig. 6.2 shows the stress-strain response until breaking point for samples with varying concentration of CNT filler under quasi-static uniaxial tension. Under quasi-static loading, the stress – strain response of PDMS as well as reinforced composites exhibit behaviour typical of elastomers; a linear elastic response under low strain followed by slightly non-linear behaviour. Increasing the CNT loading in the elastomer network results in enhanced stiffening. However, increasing the amount CNT also affects the maximum level of strain attained in the sample. This effect can be attributed to the existence of CNT agglomerates at higher weight percentages, which are not well dispersed. These bundles of CNTs acts as stress concentrators contributing to the origin of cracks.

Fig. 6.3 shows that under a constant strain rate (2500 s^{-1}), increasing the amount of CNT filler from 0 *wt %* to 2.0 *wt %* not only enhances the level of endured stresses but also increases the accumulated amount of strain. The stress increases linearly with the strain in the initial loading. After the yield point, the curve exhibits regions of strain hardening followed by strain softening region. This transition is also influenced by the amount of CNT nano-reinforcement present in the PDMS matrix. At a constant rate of loading the energy absorption is improved by ~ 33 % in samples containing *2 wt %* of CNT as compared to samples containing 0 *wt %* of CNT.

It can be seen from Fig. 6.4 that the mechanical response of composites under uniaxial compression exhibits great strain rate dependent characteristics. In comparison to the quasi-static testing, the high strain rate results show higher stress values at comparable strain.

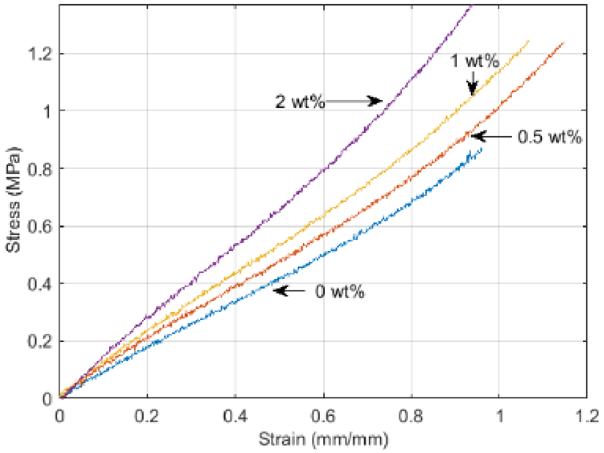

Fig. 6.2 Uniaxial tension results under quasi-static conditions for PDMS samples with varying CNT loading.

6.1.4 Conclusion

In this study, the quasi-static and high strain response of CNT based PDMS composites has been investigated. To test under impact conditions, a modified Kolsky bar apparatus was developed. The addition of CNT as nano-reinforcements has shown to enhance the stiffening and energy absorption characteristics of the material. In the high strain rate regime a more prominent effect is seen on the maximum level of stress (enhanced by 120%) and strain attained. The presence of CNT influence the strain related hardening and softening regions. Interestingly, the response of the composite also exhibited a strong strain rate dependency on the shock absorbing capability, an increase by 43 times in comparing tests performed at a strain rate of 2000 s^{-1} compared to similar tests performed at strain rates of 4300 s^{-1}.

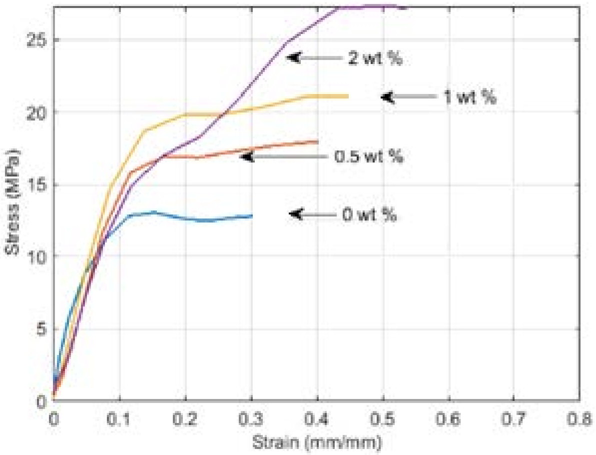

Fig. 6.3 Uniaxial compression results for the PDMS reinforced with 0 – 2 *wt%* CNT at a constant strain rate of 2500 s^{-1}.

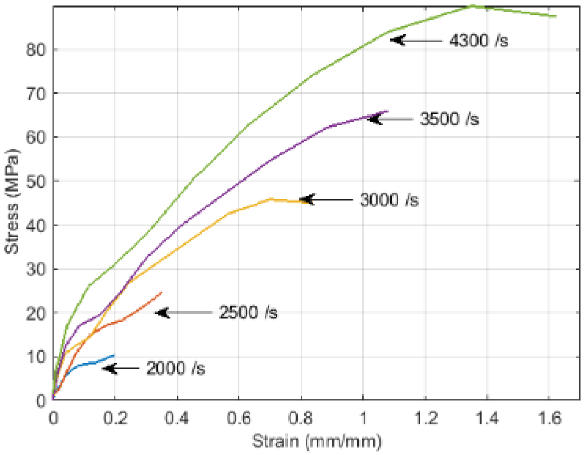

Fig. 6.4 Response of 2 *wt%* CNT reinforced PDMS samples under various strain rates.

6.2 The Effect of Strain Rate on the Response of 3-D Printed Materials

As 3-D printed materials are being embraced by the manufacturing industries, understanding the response mechanism to high strain rate events becomes a concern to meet the requirements for a specific application. In order to improve the mechanical performance of a 3-D printed part, it is necessary to quantify the impact of various printing parameters on the mechanical properties. Initial studies have shown that a difference in 3-D printed material is expected due to the effect of manufacturing parameters such as anisotropy relating to printing direction, infill pattern, infill percentage, layer height and the orientation of the part being printed. The main focus of the study is to characterize the effect of the previously mentioned printing parameters under quasit-static and high strain rate (100 – 1000 s^{-1}). In this strain rate regime, the most common apparatus used is the Split Hopkinson pressure bar (also known as the Kolsky bar).

6.2.1 Introduction

As additive manufacturing is laying the foundations for the third industrial revolution, 3-D printing (a technique in additive manufacturing) is set to revolutionize the way we make almost everything [74] . An upturn in corporate investment spending on Enterprise 3D printing is the reason why it is currently at the slope of enlightenment in the Hype Cycle [75]. 3-D printing has been used extensively in product development cycle to test kinematic functionality and design verification. Aerospace [76] and medical [77] [78] industries are also exploiting the advantages offered by additive manufacturing as it outgrows its roots of rapid prototyping.

Fused deposition modelling (by Stratasys Inc.) is a process of 3-D printing in which a thermoplastic material is extruded in layers to create a three dimensional object. In this process the design of the product is first realized within a computer aided design (CAD). From a solid model it is exported to STL tessellated format. This faceted model is then sliced into parallel horizontal cross-sections. In this process the build material, such as acrylonitrile butadiene styrene (ABS), is used is in the form of a flexible filament [79]. Through a temperature controlled extrusion nozzle each layer is melted and deposited on to the build plate in the form of fibres (Fig. 6.5a). The finished 3-D part takes the form of a vertically stacked laminated composite with a network of fibres and voids. Bonding between adjacent fibres is achieved by thermally driven diffusion welding [80]. The overall bond strength is strongly affected by the envelope temperature and variations in convective conditions within the building chamber [81]. During fabrication, bottom layers are susceptible to deformation due to residual stresses caused by uneven rapid heating and cooling cycles. This localized contraction and expansion affect not only the mechanical performance, but also causes distortions during processing [82]. Residual stress induced deformation has shown dependence on the stacking section length [83].

FDM process produces parts with unique characteristics. The material is deposited in a way that results in directional anisotropic behaviour. Moreover, overall quality and performance of a 3-D printed part are also affected by the build parameters such as printing direction, the percentage of infill amount and resolution/layer height (Fig. 6.5b). Recently, a huge amount of attention has been given to analysing and characterizing the effects of these parameters [84] [85]. Rayegani and Onwubolu [86] modelled a functional relationship between the build parameters and tensile strength using the group method of data handling (GMDH). The predicted values were a very close match for samples with different orientation, and build parameters. A similar study, done by Sood et al. [80], investigated the influence of layer thickness, raster angles, infill width and air voids on the bonding, distortion and mesostructural configuration of 3D prined parts. Furthermore, they investigated the effect of these parameters on the compressive strength of the specimens and concluded the importance of bead-to-bead bonding [87]. Compressive strength is also affected by the anisotropic behaviour due to build direction, showing a reduced strength in the transverse direction as compared to the axial direction. [88].

The most common thermoplastic polymers used in FDM-based 3D printers are Polylactic acid (PLA) and Acrylonitrile butadiene styrene (ABS). With the rapid growth of the consumer-based 3-D printing industry, new advanced materials for this process are being developed. One of the most interesting additions to the family of FDM-based printing material is a thermoplastic polyurethane (TPU), which demonstrates high flexibility and rubber-like characteristics. While a lot of attention has been devoted to understanding the performance of process parameters on popular polymers, new and game-changing materials are neglected in this aspect. Another important aspect that this study covers is the performance of build parameters under high strain rate impact like conditions. For compressive strength, quasi-static loading conditions were implemented in the literature, while the response at high strain has been neglected. Commercially available load frames cannot generate high strain rate loading as specialized testing equipment is required. This study aims to cover this knowledge barrier by incorporating non-linear hyperelastic materials under high strain rate.

6.2.2 Experimental Procedure

In this study build parameters including sample orientation and layer thickness are considered at different infill percentages. Thermoplastic polyurethane material used in this study was received in the form of filament rolls from NinjaFlex. This material is desirable due to its useful mechanical properties, such as high flexibility, high elongation at break, and chemical resistance as compared to traditional materials. A commercial entry level FDM-based 3D printer was used for fabricating the samples (Makerbot 2). Some modifications were made to the extruder to enable it to work with flexible filaments using the custom profiles settings. The extrusion temperature was kept constant for all the printed samples. Table 6.2 Extruder setting used to print TPU material.

Parameter	Values
Raster Direction	$0^o/90^o$, 45
Layer Thickness	200 µm, 400 µm
Infill%	80%, 100%

Table 6.1 Build parameters considered for the study.

Quasi-static tension tests were conducted using a commercial load frame (MTS Criterion 43) in accordance with the ASTM D638 Standard Test Methods for Tensile Properties of Plastic [89] . The tests were carried out at a crosshead speed of 0.5 mm/s and data was collected at 50 Hz. Extension values were recorded using an MTS Laser Extensometer having accuracy up to 0.001 *mm*. Non-contacting laser extensometer has the advantage to be used up to break without damage especially when testing specimen that exhibits whiplash. From the extension and load values recorded from the tension test, stress versus strain curves were generated. For each category, a total of 5 samples were fabricated and tested to assure consistency in the results.

FDM Process Parameter	Value
Infill pattern	Linear
Coarseness	0.0001 mm
Number of shells	3
Extruder temperature	220^{o} C
Extruder travel speed	50 mm/s
Print Speed	20 – 90 mm/s

Table 6.2 Extruder setting used to print TPU material

To test at high strain rates, a Kolsky bar (also known as Split Hopkinson Bar) was developed, as commercially available load frames are not able to achieve impact like conditions. This is the most common apparatus used to test at strain rates of 100 s^{-1}-10,000 s^{-1}. The principal of the Kolsky bar depends on the one-way elastic compressive wave propagation in bars. The samples are fixated between two cylindrical metallic bars and a striker is accelerated and impacted at one end to generate loading. This incident wave travels through the incident bar and upon reaching the sample/incident interface some part of the wave is reflected back while the rest is transmitted through the specimen into the transmitter bar. Strain histories are recorded in the incident and transmitter bar using strain gauges in a full bridge configuration (to compensate for bending and temperature). One important consideration while testing sample with a Kolsky bar is that the bars have to be concentrically aligned before running the tests, which can cause noise in the recorded signals and can compromise the quality of the results. As this apparatus is usually used to test height strength materials like metals, to test softer samples some modifications are required in the system. Due to major impedance mismatches between the reflecting boundaries, a wave with a small amplitude is transmitted to the transmitter bar. Using a hollow transmitter bar can increase the transmitted amplitude greatly due to amplification caused by the cross-sectional area mismatch between the bars.

Copper pulse shapers were attached between in the striker and the incident bar to (1) reduce the wave dispersion by physically filtering out the high frequency components in the generated pulse through elastic-plastic deformation, and (2) to facilitate stress equilibrium by increasing the rise time of the loading pulse. By using a pulse shaper, various loading pulse profile can be generated to characterize materials like elastomers, having characteristics which are effected by the loading shape of the pulse. For testing purposes the specimen geometry was selected to be D_s = 12 *mm* and L_s = 2.5 *mm*. A hollow transmitter tube with thickness of 2 *mm* was used and length and the diameter of this transmitter tube was selected to be, L_b = 2000 *mm* and D_b = 20 *mm*, respectively. The bars were made of aluminium AL6063, and the pulse shaper was copper CU11000. The striker is accelerated using a pressurized gas chamber. A schematic of the setup is illustrated in Fig. 5.1. The detailed design of such a testing system and parameter optimization process can be found in earlier works of the authors. [17] [18].

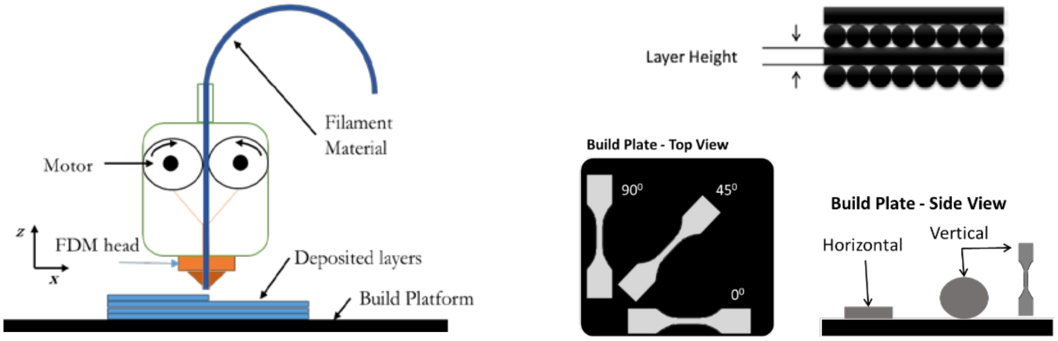

(a) (b)

Fig. 6.5 (a) Illustration of fused deopositon modelling process in 3-D printing. (b) Visualization of sample orientation and layer height.

6.2.3 Results and Discussion

Five tensile samples were printed for each category having different raster orientation, infill, and layer height. Fig. 6.7(a), illustrates the average tensile strength recorded for each category. From the figure, it can be depicted that raster orientation and percentage infill did not have any significant influence on the tensile strength of the printed TPU sample. This can also be seen in the stress-strain response of two samples with 80% infill and a layer height of 200 μm in Fig. 6.8(a) and Fig. 6.8(b) with $0/90^{o}$ raster orientation and 0.2 *mm* layer height. The small decrease associated with infill percentage is due to lower resistance present in the sample. However, layer height showed an influence in tensile strength of the sample. Increasing the layer height can also mean reducing the total number of air gaps formed due to micro distortions in the printing process. These air voids are the primary source of deformation under load. These gaps along the boundary of the shells cause separation between the fibres and fails to contribute to stiffening of the samples under loading. The stress-strain curve for such samples with different layer heights is given in Fig. 6.8(c). Since the two orientations ($0^{0}/90^{0}$ and 45^{0}) were printed with the sample lying flat on the flatbed, the anisotropic effects associated with the z-axis movement are not visible. The predominant mode of fracture line showed a dependence on the raster orientations. For $0/90^{o}$ the failure in the specimen occurred in transverse to the loading, while the 45^{o} raster orientated samples failed along the 45^{0} lines in a saw-tooth form. During solidification and cooling, residual stresses occurred as a result of volumetric shrinking that formed weaker inter-fibre bonds which serve as a possible fracture path. The non-uniform motion of the extruder on the surface of the layer increases the effect of residual stresses in some regions with respect to others. As discussed before, interlayer porosity and air voids formed due to distortion in printing and volumetric shrinking of polymers also reduces the load-bearing areas, providing a favourable fracture path.

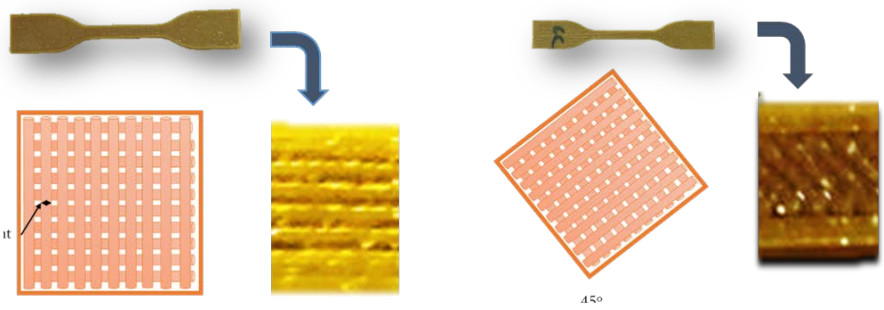

Raster orientation $0^{0}/90^{0}$

Raster orientation 45^{0}

Fig. 6.6 Illustration of build parameter, layer height, and raster orientation.

The 3-D printed TPU samples were subjected to various strain rates between the range of 2500-5000 /s under room temperature and pressure. For these tests, build parameters such as layer height, raster orientation, and percentage infill were taken into account. At high strain rates, the response of the material is very different as depicted by stress-strain curves for various samples as shown in Fig. 6.8(d-f). Strain rate not only affects the typical shape of a static stress-strain response curve, but also influences the initial modulus at low strains. This change in the resultant compressive strength associated with varying build parameters is quite prominent and exhibits extreme strain rate dependency. Compressive strengths higher than tensile strength are often observed in polymers. For this study, the tensile strength for TPU ranged from 20 to 30 MPa while the compressive strengths range from (35 to 120 MPa) for all the samples tested. The compressive strength was found to be the largest for the vertical orientation, as these samples provided aligned orientations of fibres as load carrying members as compared to increased interlayer boundaries in the horizontal orientation. This can be depicted by Fig. 6.9, while stress-strain curves for this test are presented in Fig. 6.8(d). Fig. 6.9 also illustrates the compressive strength for other build parameters such as layer height and percentage infill. Stress-strain curves for such samples are illustrated in Fig. 6.8 (e-f).

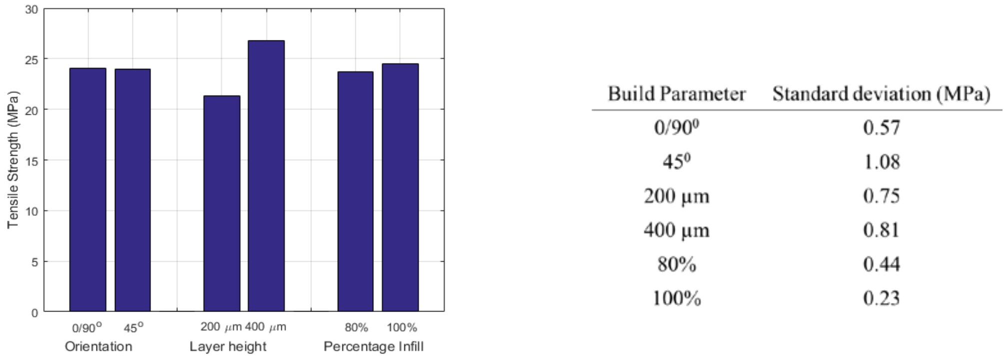

Build Parameter	Standard deviation (MPa)
0/90⁰	0.57
45⁰	1.08
200 µm	0.75
400 µm	0.81
80%	0.44
100%	0.23

(a) (b)

Fig. 6.7 (a) Tensile strength for different build parameters. (b) Standard deviation measured for each category of build parameter.

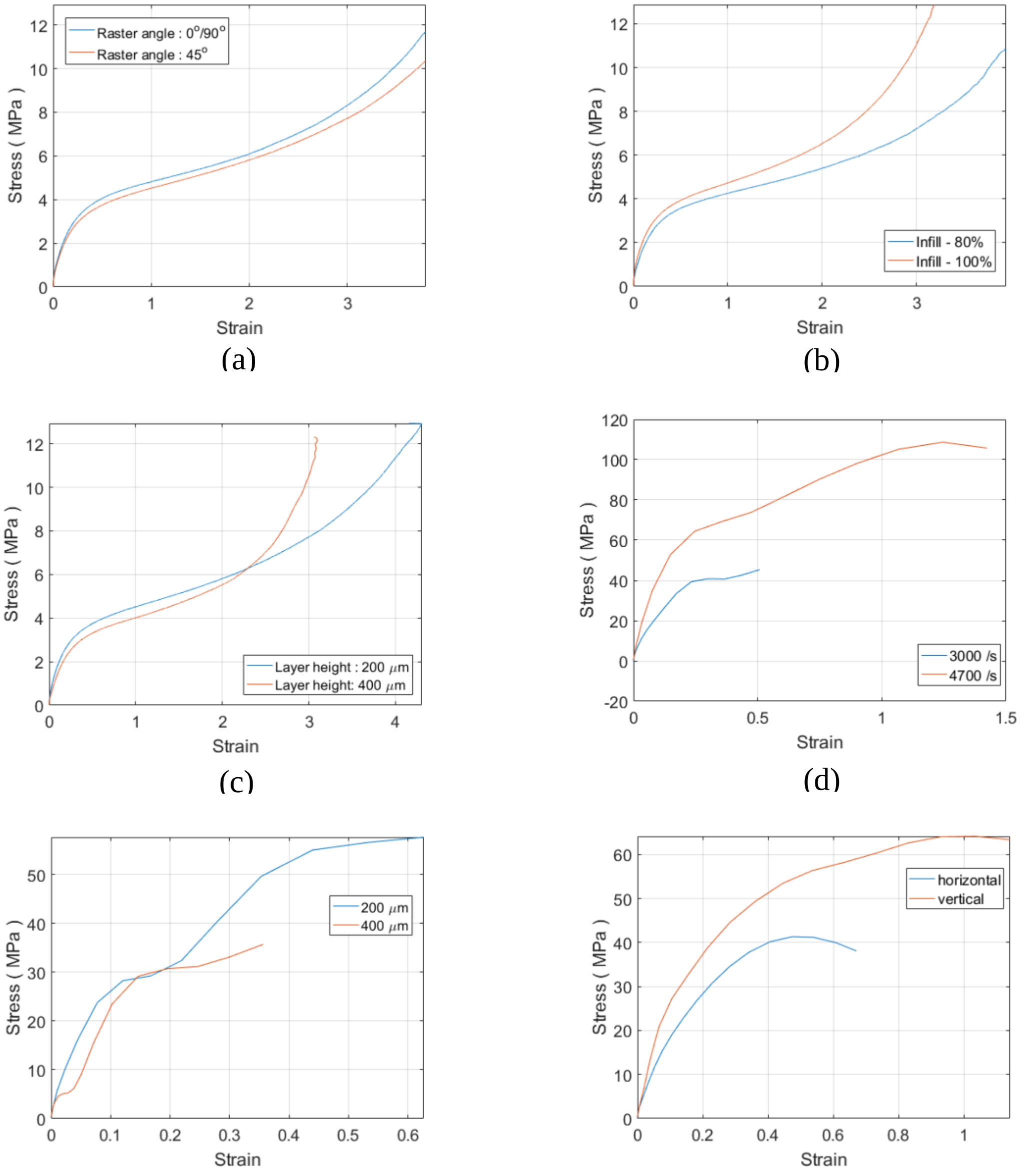

(a) (b) (c) (d) (e) (f)

Fig. 6.8 Tensile stress-strain response of samples with (a) 80% infill and 0.2 mm of layer height, (b) 0/90° raster orientation and 0.2 mm layer height, (c) 100% infill and 0/90° raster orientation, (d) 80% infill, 0.2 mm layer height, horizontal specimen, (e) 80%infill, vertical orientation, 3000 /s strain rate, (f) 80% infill, 0.2 mm layer height 3000 /s strain rate.

6.2.4 Conclusion

In this study, our focus was dedicated to exploring mechanical properties of TPU material available for 3-D printers based on fused deposition modelling technique. Quasi-static tension and high strain rate compression tests were performed to analyse the effect of various build parameters such as percentage infill, raster orientation and a layer height of the samples. In tension testing, the raster orientation did not show any influence on the tensile strength of the sample, however, percentage infill, and layer height did affect the tensile strength of the specimen. The effect of these build parameters is more evident at high strain rates. Under impact like compression, the material exhibited greater compressive strength than tensile strength. Furthermore, anisotropy related to the building direction showed a change of 30 percent in the compressive strength. This is due to the volumetric shrinkage of lower layers through residual stress accumulation. In designing a 3-D printed component, the effect of build parameters should be kept under consideration, especially while manufacturing components to perform under high-strain rate.

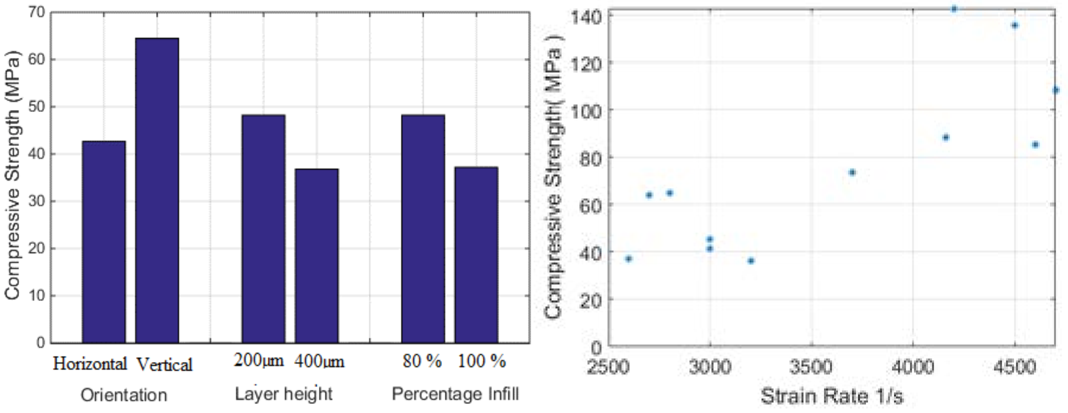

(a) (b)

Fig. 6.9 Compressive strength for various build parameters under high strain rates.

The effect of and interaction between printing parameters with respect to the tensile strength of the samples are analysed in Fig. 6.10. Results revealed that the most significant factor affecting the tensile strength is the resolution or layer width of the specimen Fig. 6.10(a). Furthermore, a significant multi-factor interaction exists between infill percentage and resolution followed by infill percentage and orientation, Fig. 6.10(b). Test samples were subjected to various strain rates ranging between 2500-5000 /s. Strain rate not only effects the typical shape of static stress-strain response curve, but also affects the initial modulus at low strains and the compressive strength, Fig. 6.9(b). The compressive strength was found to be the largest for the vertical orientation, as these samples provided aligned orientations of fibres as load carrying members as compared to increased interlayer boundaries in the horizontal orientation.

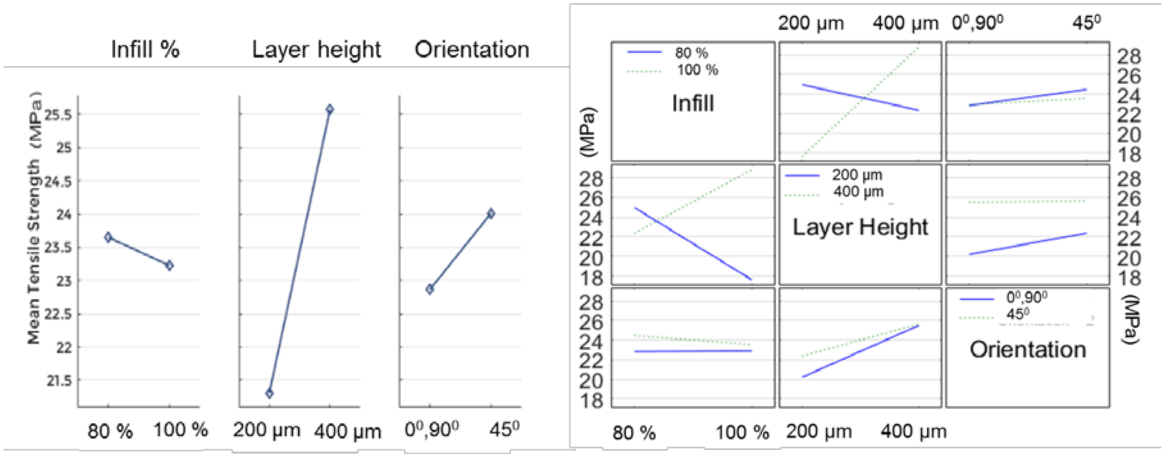

(a) (b)

Fig. 6.10 (a) Main effect plot for tensile strength, (b) Interaction plot build parameters.

Chapter 7 Conclusion and Future Work

Summary: In this chapter, we state the problem, identify the objectives of the study, and outline the contributions resulting from this work. Furthermore, a brief description is provided regarding areas that require additional work.

7.1 Statement of the Problem

To understand the behaviour of and to develop components for dynamic applications, the response of elastomers needs to be understood at different rates of loading. For instance, in collision-related scenarios, elastomeric components designed from an understanding of behaviours under quasi-static loading may fail prematurely under impact, thereby compromising the system's integrity and risking valuable human lives.

Hyperelastic theory is generally adopted to model and to predict the stress-strain behaviour of elastomeric materials. By conducting material testing under different modes of deformation, material parameters for such models are evaluated. The performance of the different available hyperelastic models varies in terms of accuracy and predictability, depending on the availability of material test data.

The mechanical response of an elastomer is dependent upon the rate of applied loading. The material parameters evaluated from a static testing condition cannot predict the behaviour when loading at high strain rates. To obtain the stress strain response of elastomers under impact-type loading, they need to be tested using a specialized testing apparatus that can reach strain rates of $10^2 – 10^4$ s^{-1}. The Kolsky compression bar is the testing apparatus most commonly used to generate high strain rates of loading. Since there are no standards available for such dynamic tests, the apparatus needs to be modified to test soft, low-impedance materials such as elastomers.

The finite element method can be used to model the deformation of elastomers under loading. Moreover, in designing the Kolsky bar, numerical modelling can be employed to model and to calibrate the testing apparatus. The testing parameters and specimen geometry can be optimized to ensure that the Kolsky compression bar works accurately.

In this study, the methodology for characterizing elastomers under high strain is presented. The three main aspects of the problem, constitutive modelling, experiment testing and numerical modelling, are discussed.

7.2 Objectives

The objective of this study was to develop and implement a comprehensive methodology for testing, characterization and modelling of elastomers at moderate to intermediate and high strain rates. Particular attention was devoted to:

(i) Implementation of hyperelastic models for elastomers. Furthermore, conducting a performance comparison study for various material models for different cases, where the amount of available test data may have been complete or limited.

(ii) Development of a high strain rate testing equipment for elastomers, and conducting quasi-static and dynamic testing at different strain rates to provide input data for material characterization,

(iii) Validation of the experimental design of and selecting appropriate testing parameters for the developed high strain rate testing equipment through finite element analysis, and

(iv) Application of the developed methodology to understand the effect of strain rate on the mechanical performance of newly engineered elastomers and materials made using modern manufacturing techniques such as 3-D fused deposition modelling.

7.3 General Conclusions

In this study, we provided a framework incorporating the three most important areas of material engineering; mechanical characterization, numerical modelling, and mechanical testing of elastomers. The outcomes of these three areas of study were then used to explore another important aspect, which is related to the manufacturing techniques for elastomers.

Hyperelastic model calibration

To find a suitable hyperelastic material model, we compared and analysed the performance of various available models in commercial finite element software. Model validation was conducted by simulating elastomer samples using finite element analysis. Comparison was made in terms of accuracy and stability in predicting the stress-strain response of elastomers under two cases, (i) having access to uniaxial, planar, biaxial and volumetric test data, and (ii) having access to limited test data (uniaxial tension only).

Kolsky bar design optimization

To test soft and low-impedance materials, the traditional Kolsky compression bar needs to be modified. To satisfy the necessary working conditions, we present a modified Kolsky bar that is able to generate loading of strain rates up to 10,000 s^{-1}. Using this apparatus, NBR samples were tested and the results were used to evaluate material parameters for numerical modelling.

Numerical Modelling

The newly built testing apparatus was modelled using finite element methodology to calibrate and optimize the design. Moreover, a detailed pulse shaper analysis and specimen geometry selection criteria were presented and discussed. Some critical alignment requirements in the Kolsky bar were investigated in order to guarantee accurate testing results were evaluated and presented.

Case studies

Finally, the methodology developed to test and characterize the response of elastomers under high-strain rate loading conditions using a modified Kolsky bar testing apparatus is employed to study two unique engineering materials. Firstly, we investigate the response of carbon nanotube-reinforced elastomers made using traditional manufacturing techniques. In the second application, we characterize a traditional and commonly used class of elastomers that was manufactured using new and emerging 3D printing techniques.

7.4 Thesis Contributions

The main contributions of the current work can be summarised as follows:

(i) Implemented and conducted a performance comparison study of hyperelastic material models for elastomers,

(ii) Developed a high strain rate testing equipment for elastomers, and conducted quasi-static and dynamic testing at different strain rates to provide input data for material characterization,

(iii) Validated the experimental design of Kolsky bar and selected appropriate testing parameters for the developed high strain rate testing equipment through finite element analysis, and

(iv) Applied the developed methodology to understand the effect of strain rate associated with the mechanical performance of newly engineered elastomers and of modern manufacturing techniques.

7.5 Future Work

The following areas require additional future research:

(i) Extend the dynamic characterization of elastomers to account for temperature dependence,

(ii) Development and Implementation of constitutive laws able to predict the material behaviour at different strain rates from quasi-static data, and

(iii) Accommodating the time-dependant viscoelastic effect in the numerical modelling of elastomers.

It is well known that, in dynamic applications, elastomeric components are subjected to various extreme working environments. For example, when designing shock absorbers for the automotive industry, one needs to take into account not only the rate of applied loading, but also temperature. This dependence on the nonlinear characteristic of stress/strain needs to be explored and studied in detail.

In this study, only the high strain rate response for uniaxial compression is taken into account. We have also discussed that in order to have a more reliable material definition, more than one form of deformation data is required. This can be done by extending and developing the Kolsky bar to generate high strain rate loading under uniaxial tension and pure shear deformation.

Typically, developed hyperelastic material models are static in nature. They may be used to generate a family of stress strain curves as a reference for materials with some mathematical relation, defining the changes with strain rate. As the hyperelastic theory can be used to predict the behaviour at only one constant strain rate, there is a need to develop and analyse truly strain rate dependant modelling strategies. One such strategy is to include the viscoelastic material definition. Again, to evaluate time related viscoelastic material coefficient, mechanical testing is required. By doing this, material response at one specific strain rate may be used to predict the responses at other strain rates.

References

[1] Ceresna, “Market Study: Synthetic Rubber (2nd edition),” 2012. [Online]. Available: http://www.ceresana.com/en/market-studies/plastics/synthetic-rubber/market-study-synthetic-rubber.html.

[2] “Crashworthiness,” Enhance-Eng, [Online]. Available: http://www.nhance-eng.com/products/lsdyna_env/lsdyna/crashworthiness.html. [Accessed 18 05 2016].

[3] “http://www.dowcorning.com/content/auto/autointerior/airbag-coating-sealing.aspx?e=What+Is+Your+Application%3f&wt.svl=FS_readmore_auto_TPOA,” DOW Corning. [Online].

[4] “Safety Tested 16 Helmets One Toughest RD Labs,” Transworld, [Online]. Available: http://snowboarding.transworld.net/videos/safety-tested-16-helmets-one-toughest-rd-labs/#gksKFuFUt3WPgutA.97. [Accessed 18 05 2016].

[5] “Elasotmer Applications,” Covestro, [Online]. Available: http://www.elastomers.covestro.com/en/Applications/Automotive. [Accessed 18 05 2016].

[6] H. Kolsky, “An Investigation of the Mechanical Properties of Materials at very High Strain Rates of Loading,” *Proc. Phys. Soc,* 1949.

[7] M.C. Shaw and E. Young, “Rubber Elasticity and Fracture,” *Jounral of Engineering Materials and Technology,* vol. 110, no. 3, pp. 258-265, 1988.

[8] I Fried and A. R. Johnson, “A Note on Elastic Energy Density Functions for Largely Deformed Compressible Rubber Solids,” *Computer Methods in Applied Mechanics and Engineering,* vol. 69, no. 1, pp. 53-64, 1988.

[9] Mooney M., “A theory of elastic deformation,” *Journal of Applied Physics,* vol. 11, no. 9, pp. 582-592, 1940.

[10] Treloar and L.R.G., “Stress Strain Data fir Vulcanised Rubber Under Various Types of Deformation,” *Transactions of the Faraday Society,* vol. 40, pp. 59-70, 1944.

[11] Rivlin R.S., “Large Elastic Deformation of Isotropic Materials I, Fundamental Conncepts,” *Philosophical Transactions of Royal Society of London*, vol. A, pp. 459-490, 1948a.

[12] Rivilin R. S. , “Large Elastic Deformations of Istropic Materials IV, Further Development of the General Theory,” *Philosophical Transcations of the Royal Society of London*, vol. 241, no. 835, pp. 379-397, 1948b.

[13] Yeoh, O.H., “Some Form of Strain Energy Function for Rubber,” *Rubber Chemistry and Technology*, vol. 66, pp. 754-771, 1993.

[14] Ogden, R.W., “Large Deformation Isotropic Elasticity - On the Correlation of Theory and Experiment for Incompressible Rubber-Like Solids,” *Proceedings of the Royal Society,* vol. 326, no. A, pp. 565-584, 1972.

[15] Forni M., A. Martelli and A. Dusi, “Implementation and Validation of Hyperelastic Finite Element Models of High Damping Rubber Bearings,” in *Constitutive Models for Rubber, A1 Dorfmann,* UL , AA Balkema Publishers, 1999, pp. 237-247.

[16] Arruda, E. M. and Boyce, M.C., “A Three Dimensional Constitutive Model for the Large Stretch Behaviour of Rubber Elastic Materials,” *Journal of the Mechanics and Physics of Solids,* vol. 41, pp. 389-412, 1993.

[17] Hopkinson B., “A Method of Measuring the Pressure Produced in the Detonation of High Explosives or by Impact of Bullets,” *Trans. R. Sco. (London),* vol. A, no. 213, p. 437456, 1914.

[18] Davies and R. M, “A Critical Study of the Hopkinson Pressure Bar,” *Proc. R. Soc. London* , vol. A240, pp. 375-457, 1948.

[19] G. T. G. III, “Classic Split-Hopkinson Pressure Bar Testing,” in *ASM Handbook: Mechanical Testing and Evaluation*, 2000, pp. 1027-1036.

[20] Kolsky, H, “Stress Wave in Solids,” *Dover, New York*, 1983.

[21] Krafft J. M, Sullivan A. M and Tipper C. F, “The Effect of Static and Dynamic Loading and Temperature on the Yield Stresses of Iron and Mild Steel in Comparison,” *Proc. Roy. Soc. London*, vol. A221, pp. 114-127, 1954.

[22] Follansbee, P.S , “The Hopkinson Bar,” in *Mechanical Testing, ASM Handbook (9th edition)*, Metals park, Ohio, 1995, pp. 198-217.

[23] Nemat-Nasser, S., Isaacs, J.B. and Starrett, J.E., “Hopkinson Techniques for Dynamic Recovery Experiments. Pro.,” *Pro. Royal Soc. London,* vol. 435, pp. 371-391, 1991.

[24] Gray, G.T and Blumenthal, W.R., “Split Hopkinson pressure bar testing of Soft materials,” in *ASM Handbook, Mechanical Testing and Evaluation*, Materials Park, Ohio, ASM, 2000, pp. 488-496.

[25] Field, J.E., Walley, S.M., Proud, W.G., Goldrein, H.T. and , Siviour, C.R., “Review of Experimental Techniques for High Rate Deformation and Shock Studies,” *Int. J. Impact Eng,* vol. 30, pp. 725-775, 2004.

[26] R. W. Chen, “Dynamic Compressive Behaviour of a Glass ceramic Under Lateral Confinement,” *J. Mech. Physical Solids,* vol. 45, pp. 1303-1328, 1997.

[27] B. Song, M. Forrestal and W. Chen, “Dynamic and quasi-static propagationof compaction waves in a low-density epoxy foam,” *Experimental Mechanics,* vol. 46, pp. 127-136, 2006.

[28] J. T. L. Ninan and C. Sun, “Use of Split Hopkinson Pressure Bar for Testing off-axis Composites,” *Int Journal of Impact Engineering,* vol. 25, pp. 291-313, 2001.

[29] W. Chen, Q. Wu, J. Kang and N. Winfree, “Compressive superelastic behavior of a NiTi shape memory alloy at a strain rates of 0.001/s to 750/s,” *Int. J. Solids Struct.,* vol. 38, pp. 8989-8998, 2001.

[30] Wang , L. L, Foundations of Stress Waves, Elsevier, 2007.

[31] C. W.W. and S. Bo, Split Hopkinson (Kolsky) Bar: Design, Testing and Aplications, 233 Spring Street, New York: © Springer Science+Business Media,, 2011.

[32] Pochhammer L, “On the propagation velocities of small oscillations in an unlimited isotropic circular cylinder,” *J. fur die Reine und Angewandte Mathematik,* vol. 81, pp. 324-326, 1876.

[33] Chree C, “The equations of an isotropic elastic solid in polar and cylin- drical coordinates, their solutions and applications,” *Tans. Cambridge Phil. Soc,* vol. 14, pp. 250-369, 1889.

[34] Gorham, D.A., “A Numerical Method for the Correction of Dispersion in Pressure Bar Signals.,” *J. Phys. E: Sci. Instru,* vol. 16, pp. 477-179, 1983.

[35] Gong, J.C., Malvern, L.E. and Jenkins, D.A., “Dispersion investigation in the split Hopkinson pressure bar,” *Trans. ASME, J. Eng. Mater. Technol.,* vol. 112, pp. 309-314, 1990.

[36] Follansbee, P.S. and Frantz, C., “Wave Propagation in the Split Hopkinson Pressure Bar,” *Trans. ASME, J. Eng. Mater. Technol.,* vol. 1983, pp. 61-66, 1983.

[37] Zencker, U. and Clos, R., “Limiting Conditions for Compression Testing of Flat Specimens in the Split Hopkinson Pressure Bar,” *Exp. Mech.,* vol. 39, pp. 343-348, 1998.

[38] Song, B., , Forrestal, M.J., Chen, W. and Montgomery, S, “Mechanical Properties of an Alumina-filled Epoxy at Various Strain Rates,” *J. Com- posite Mater.,* vol. 43, pp. 1519-1536 , 2009.

[39] Trautmann, A., Siviour, C.R., Walley, S.M. and Field, “Lubrication of Polycarbonate at Cryogenic Temperatures in the Split Hopkinson Pressure Bar,” *Int. J. Impact Eng,* vol. 31, pp. 523-544, 2005.

[40] “Dynamic Mechanical Response of Bovine Gray Matter and White Matter Brain Tissues Under Compression,” *J. Biomech.,* vol. 42, pp. 731-735, 2009.

[41] Samanta, S.K, “Dynamic deformation of aluminum and copper at ele- vated temperatures,” *J. Mech. Phys. Solids,* vol. 19, pp. 117-135, 1971.

[42] Forrestal, M. J., Wright, T. W. and Chen, W., “The Effect of Radial Inertia on Brittle Samples During The Split Hopkinson Pressure Bar Test,” *International Journal of Impact Engineering,* vol. 34, pp. 405-411, 2007.

[43] Warren, T. L. and Forrestal, M. J., “Comments on the Effect of Radial Inertia in the Kolsky Bar Test for an Incompressible Material,” *Experimental Mechanics,* vol. 50, pp. 1253-1255, 2010.

[44] Duffy, J., Campbell, J.D. and Hawley, R.H., “On the Use of a Torsional Split Hopkinson Bar to Study Rate Effects in 1100-0 Aluminum,” *ASME, J. Appl. Mech.,* vol. 37, pp. 83-91, 1971.

[45] Christensen, R.J., Swanson, S.R. and Brown, W.S.:, "Split-Hopkinson-Bar Tests on Rocks Under Confining Pressure.," *Exp. Mech.,* pp. 508-513, 1972.

[46] Parry, D.J., Walker, A.G. and Dixon, P.R., "Hopkinson Bar Pulse Smoothing," *Measur. Sci. Technol.,* vol. 3, pp. 443-446, 1995.

[47] Bragov, A.M. and Lomunov, A.K., "Methodological Aspects of Studying Dynamic Material Properties Using the Kolsky Method," *Int. J. Impact Eng,* vol. 16, pp. 321-330, 1195.

[48] W. Chen and B. Song, "Chapter1: Dynamic Characterization of Soft Materials," in *Dynamic Failure of Materials and Structures,* Springer, 2009, pp. 1-28.

[49] Mary C. Boyce and Ellen M. Arruda, "Constitutive Models of Rubber Elasticity," *Jouranl of Biomechanics,* vol. 73.

[50] L. Treloar, "Stress-Strain Data for Vulcanized Rubber Under Various Types of Deformation," *Transactions of the Faraday Society,* vol. 40, 1944.

[51] Chagnon G, Marchkmann G and Verron E, "A cComparison of the Hart-Smith model with Arruda-Boyce and Gent Formulations for Rubber Elasticity," *Rubber Chemistry and Technology,* vol. 77, no. 4, pp. 724-735, 2004.

[52] D. Systemes, "Abaqus User Guide and Manual," Abaqus Simulia, 2012.

[53] Kaliske, M. and H. Rothert, "On the Finite Element Implementation of RUbber-Like Materials at Finite Strains," *Engineering Computation,* vol. 14, no. 2, pp. 216-232, 1997.

[54] R. C. A. C. M.S. Chaudhry, "Design of Kolsky Bar to Characterize the Dynamic Respoonse of Elastomers Under High Strain Rate," *CANCAM,* 2015.

[55] Duncan BC, Crocker LE, Hunt R and Maxwell AS, "Verification of HyperElastic Test Methods," Teddington:NPL, NPL report CMMT(A) 226, 1999.

[56] X. Wu and D. Gorham, "Stress Equilibrium in Split Hopkinson Bar Testq," *J. Phys,* vol. IV, pp. 91-96, 1997.

[57] W. Chen, B. Zhang and M. J. Forrestal, "A Split Hopkinson Bar Technique for Low-impedance Materials," *Experimental Mechanics,* p. 5, 1998.

[58] Frantz C.E, P.S. Follasnbee and W.J. Wright, “New Experimental Techniques with the Split Hopkinson Pressure Bar,” in *Proc 8th Int Conf High Energy Rate Fabrication,*, San Antonio, 1984.

[59] W. Chen, B. Song, D.J. Frew and M.J. Forrestal, “Dynamic Small Strain Measeurements of a Metal Specimen with a Split Hopkinson Pressure Bar,” *Experimental Mechanics,* vol. 43, no. 1, pp. 20-23, 2003.

[60] D.J. Frew, M. J. Forrestal and W, Chen, “Pulse Shaping Techniques for Testing Brittle Materials with a Split Hopkinson Bar.,” *Experimental Mechanics,* vol. 42, no. 1, pp. 93-106, 2002.

[61] W. Chen, F. Lu and B. Zhou, “A Quartz Crystal Embedded Split Hopkinson Pressure Bar for Soft Materials,” *Experimental Mechanics,* vol. 40, no. 1, pp. 1-6, 2000.

[62] D. Casem, “Inertial Effects of Quartz Force Transducers Embedded in a Split Hopkinson Pressure Bar,” *Experimental Mechanics,* vol. 45, no. 4, pp. 368-376, 2008.

[63] R. A. M.S. Chaudhry, “Finite Element Modelling anf Validation of a Modififed Kolsky Bar Developed for High Strain Rate Testing of Elastomers.,” *IEMECE,* 2015.

[64] “A Third industrial Revolution,” The Economist, 2012.

[65] “Gartner Hype Cycle.,” Gartner, 2014b.

[66] Rochus P, Plesseria JY, Van Elsen, Kruth JP, Carrus R and Dormal T, “New Appications of Rapid Prototyping and Rapid Manufacturing (RP/RM) Technologies for Space Instrumentation,” *Acta Astrounaut,* vol. 61, no. 1-6, pp. 352-359, 2007.

[67] Lohfeld S, McHugh P, Serban D, Boyle D, O’Donnell G and Peckitt, “Engineering Assisted Surgery: A Route for Digital Design and Manufacturing of Customised Maxillofacial Implants,” *J. Mater Process Technol,* vol. 183, no. 2-3, pp. 333-338, 2007.

[68] Colombo G, Filippi S, Rizzi C and Rotini F, “A New Design Paradigm For the Development of Custom-Fit Sockets for Lower Limb Prostheses,” *Comp Ind,* vol. 61, no. 6, pp. 513-523, 2010.

[69] Upcraft S and Fletcher R., “The Rapid Prototyping Technologies,” *Assembly Automat,* vol. 23, no. 4, pp. 318-330, 2003.

[70] Sood AK, Ohdar RK and Mahapatra SS, “Parametric Appraisal of Fused Deposition Modelling Process Using the Grey Taguchi,” *Proc Inst Eng B J Eng Manuf*, vol. 224, no. 1, pp. 135-145, 2010.

[71] Q. Sun, “Effect of Processing Conditions on The Bonding Quality of FDM Polymer Filaments,” *Rapid Prototyping Journal,* vol. 14, no. 2, pp. 72-80, 2007.

[72] Zhang Y and Chou K, “A Paramteric Study of Part Distortion in Fused Deposition Modelling Using Three-Dimensional Finite Element Analysis,” *J Eng Manuf*, vol. 228, no. 8, pp. 959-967, 2008.

[73] Wang TM, Xi JT and Jin Y, “A Model Research for Prototype Warp Deofrmation in the FDM Process,” *Int J Adv Manuf Technol*, vol. 33, no. 11-12, pp. 1087-1096, 2007.

[74] Constance Ziemian, Mala Sharma and Sophia Ziemian, “Anisotropic Mechanical Properties of ABS Parts Fabricated by Fused Deposition Modelling,” in *Mechanical Engineering*, InTech.

[75] Lee B.H., Abdullah J. and Khan Z., “Optimization of Rapid Prototyping Parameters for Production of Flexible ABS Object,” *Journal of Materials Processing Technology,* vol. 30, no. 10, pp. 54-61, 2005.

[76] Rayegani F. and Onwubolu G.C., “Fused Deposition Modelling (FDM) Process Parameter Prediction and optimization Using Group Method for Data Handling (GMDH) and Differential Evolution (DE),” *The International Journal Of Advanced Manufacturing Technology,* 2014.

[77] Anoop K. Sood, Raj K. Ohdar and Siba S. Mahapatra, “Experimental Investigation and Empirical Modeling of FDM Process for Compressive Strength Improvement,” *Jouranl of Advanced Research*, vol. 3, pp. 81-90, 2012.

[78] Lee C, Kim S, Kim H and Ahn S, “Measurement of Anisotropic Compressive Strength of Rapid Prototyping Parts,” *Journal of Materilas Processing Technology,* vol. 187, pp. 627-630, 2007.

[79] ASTM Standard D638, “Standard test methods for tensile properties of plastics,” *ASTM International, West Conshohocken, PA,* 2010.

Appendix A: Input File

```
*Heading
** Job name: calibration Model name: 111
** Generated by: Abaqus/CAE 6.14-2
*Preprint, echo=NO, model=NO, history=NO, contact=NO
**
** PARTS
**
*Part, name=INCIDENT
*Node
      1, -0.00382683426, 0.00923879538,           2.
      2,           0., 0.00999999978,           2.
      3,           0., 0.00999999978,           0.

*Element, type=C3D8R
   1,  434, 2728, 2776, 1144,    1,   11,  550,  214
   2, 2728, 2729, 2777, 2776,   11,   12,  551,  550

*Nset, nset=PART, generate
    1,  5151,     1
*Elset, elset=PART, generate
    1,  4000,     1
** Section: Aluminum
*Solid Section, elset=PART, material=ALUMINUM
,
*End Part
**
*Part, name=STRIKER
*Node
```

```
      1, -0.00382683426, 0.00923879538,          0.5
      2,            0., 0.00999999978,          0.5
      3,            0., 0.00999999978,           0.

*Element, type=C3D8R
   1,  230, 1072, 1104,  680,    1,   11,  288,  116
   2, 1072, 1073, 1105, 1104,   11,   12,  289,  288
   3, 1073, 1074, 1106, 1105,   12,   13,  290,  289

*Nset, nset=PART, generate
    1,  1887,     1
*Elset, elset=PART, generate
    1,  1500,     1
** Section: Aluminum
*Solid Section, elset=PART, material=ALUMINUM
,
*End Part
**
*Part, name=TRANSMITTER
*Node
      1, -0.00344415079, 0.00831491593, 0.00999999978
      2,            0., 0.00899999961, 0.00999999978
      3,            0., 0.00899999961,   1.79999995

*Element, type=C3D8R
  1,    8,  226,  875,  330,    1,   17,  479,  222
  2,  226,  225,  876,  875,   17,   18,  480,  479

*Element, type=C3D6
556,  15, 429,   9,  16, 436,  12
557, 431, 430,  15, 434, 435,  16
```

```
*Nset, nset=PART, generate
   1,  1346,     1
*Elset, elset=PART, generate
  1,  560,    1
** Section: Aluminum
*Solid Section, elset=PART, material=ALUMINUM
,
*End Part
**
**
** ASSEMBLY
**
*Assembly, name=Assembly
**
*Instance, name=INCIDENT-1, part=INCIDENT
*End Instance
**
*Instance, name=STRIKER-1, part=STRIKER
 -1.73472347597681e-18,           0.,         -0.5
*End Instance
**
*Instance, name=TRANSMITTER-1, part=TRANSMITTER
          0.,           0.,           2.
*End Instance
**
*Nset, nset=ASSEMBLY, instance=INCIDENT-1, generate
   1,  5151,     1
*Nset, nset=ASSEMBLY, instance=STRIKER-1, generate
   1,  1887,     1
*Nset, nset=ASSEMBLY, instance=TRANSMITTER-1, generate
```

```
    1,  1346,     1
*Elset, elset=INCI_750, instance=INCIDENT-1
 3752,
*Nset, nset=INCI_MID, instance=INCIDENT-1
 64,
*Elset, elset=INCI_MID_ELEMENT, instance=INCIDENT-1
 204,
*Nset, nset="STRIKER VELOCITY SURFACE", instance=STRIKER-1
    3,    4,    6,    7,    9,   64,   65,   66,   67,  170,  171,  172,  173,  223,  224,  225
  226,  231,  232,  233,  234, 1088, 1089, 1090, 1091, 1092, 1093, 1094, 1095, 1096,
1097, 1098
 1099, 1100, 1101, 1102, 1103
*Elset, elset="STRIKER VELOCITY SURFACE", instance=STRIKER-1
  246,  247,  248,  249,  250,  496,  497,  498,  499,  500,  746,  747,  748,  749,  750,
996
  997,  998,  999, 1000, 1246, 1247, 1248, 1249, 1250, 1251, 1252, 1253, 1254,
1255
*Elset, elset=TRANS_450, instance=TRANSMITTER-1
 128,
*Nset, nset=TRAN_MID, instance=TRANSMITTER-1
 277,
*Elset, elset=TRAN_MID_ELE, instance=TRANSMITTER-1
 250,
*Nset, nset=TRASN_END, instance=TRANSMITTER-1
   3,   4,   6,   7, 120, 121, 122, 123, 326, 327, 328, 329
*Elset, elset=_IN_PS_S1, internal, instance=INCIDENT-1, generate
 3601,  3604,     1
*Elset, elset=_IN_PS_S5, internal, instance=INCIDENT-1
  397,  398,  399,  400,  797,  798,  799,  800, 1197, 1198, 1199, 1200, 1597, 1598,
1599, 1600
```

```
 1997, 1998, 1999, 2000, 2397, 2398, 2399, 2400, 2797, 2798, 2799, 2800, 3197, 3198, 3199, 3200
 3597, 3598, 3599, 3600
*Elset, elset=_IN_SP_S2, internal, instance=INCIDENT-1, generate
 3997,  4000,     1
*Elset, elset=_IN_SP_S3, internal, instance=INCIDENT-1
    1,    2,    3,    4,  401,  402,  403,  404,  801,  802,  803,  804, 1201, 1202, 1203, 1204
 1601, 1602, 1603, 1604, 2001, 2002, 2003, 2004, 2401, 2402, 2403, 2404, 2801, 2802, 2803, 2804
 3201, 3202, 3203, 3204
*Elset, elset=_LOAD_S1, internal, instance=STRIKER-1, generate
 1251,  1255,     1
*Elset, elset=_LOAD_S5, internal, instance=STRIKER-1
  246,  247,  248,  249,  250,  496,  497,  498,  499,  500,  746,  747,  748,  749,  750,  996
  997,  998,  999, 1000, 1246, 1247, 1248, 1249, 1250
*Elset, elset=_ST_MT_S1, internal, instance=STRIKER-1, generate
 1251,  1255,     1
*Elset, elset=_ST_MT_S5, internal, instance=STRIKER-1
  246,  247,  248,  249,  250,  496,  497,  498,  499,  500,  746,  747,  748,  749,  750,  996
  997,  998,  999, 1000, 1246, 1247, 1248, 1249, 1250
*Elset, elset=_ST_PS_S2, internal, instance=STRIKER-1, generate
 1496,  1500,     1
*Elset, elset=_ST_PS_S3, internal, instance=STRIKER-1
    1,    2,    3,    4,    5,  251,  252,  253,  254,  255,  501,  502,  503,  504,  505,  751
  752,  753,  754,  755, 1001, 1002, 1003, 1004, 1005
*Elset, elset=_TR_SP_S2, internal, instance=TRANSMITTER-1, generate
 556,  560,    1
*Elset, elset=_TR_SP_S5, internal, instance=TRANSMITTER-1, generate
```

```
 501,  555,    1
*Elset, elset=_IN_PS_S1_1, internal, instance=INCIDENT-1, generate
 3601,  3604,     1
*Elset, elset=_IN_PS_S5_1, internal, instance=INCIDENT-1
  397,  398,  399,  400,  797,  798,  799,  800, 1197, 1198, 1199, 1200, 1597, 1598, 1599, 1600
 1997, 1998, 1999, 2000, 2397, 2398, 2399, 2400, 2797, 2798, 2799, 2800, 3197, 3198, 3199, 3200
 3597, 3598, 3599, 3600
*Surface, type=ELEMENT, name=IN_PS
_IN_PS_S1_1, S1
_IN_PS_S5_1, S5
*Elset, elset=_IN_SP_S3_1, internal, instance=INCIDENT-1
    1,    2,    3,    4,  401,  402,  403,  404,  801,  802,  803,  804, 1201, 1202, 1203, 1204
 1601, 1602, 1603, 1604, 2001, 2002, 2003, 2004, 2401, 2402, 2403, 2404, 2801, 2802, 2803, 2804
 3201, 3202, 3203, 3204
*Elset, elset=_IN_SP_S2_1, internal, instance=INCIDENT-1, generate
 3997,  4000,     1
*Surface, type=ELEMENT, name=IN_SP
_IN_SP_S3_1, S3
_IN_SP_S2_1, S2
*Elset, elset=_ST_MT_S1_1, internal, instance=STRIKER-1, generate
 1251,  1255,     1
*Elset, elset=_ST_MT_S5_1, internal, instance=STRIKER-1
  246,  247,  248,  249,  250,  496,  497,  498,  499,  500,  746,  747,  748,  749,  750,  996
  997,  998,  999, 1000, 1246, 1247, 1248, 1249, 1250
*Surface, type=ELEMENT, name=ST_MT
_ST_MT_S1_1, S1
```

```
_ST_MT_S5_1, S5
*Elset, elset=_ST_PS_S3_1, internal, instance=STRIKER-1
    1,    2,    3,    4,    5,  251,  252,  253,  254,  255,  501,  502,  503,  504,  505,  751
  752,  753,  754,  755, 1001, 1002, 1003, 1004, 1005
*Elset, elset=_ST_PS_S2_1, internal, instance=STRIKER-1, generate
 1496,  1500,     1
*Surface, type=ELEMENT, name=ST_PS
_ST_PS_S3_1, S3
_ST_PS_S2_1, S2
*Elset, elset=_TR_SP_S2_1, internal, instance=TRANSMITTER-1, generate
 556,  560,    1
*Elset, elset=_TR_SP_S5_1, internal, instance=TRANSMITTER-1, generate
 501,  555,    1
*Surface, type=ELEMENT, name=TR_SP
_TR_SP_S2_1, S2
_TR_SP_S5_1, S5
*End Assembly
**
** MATERIALS
**
*Material, name=ALUMINUM
*Density
2700.,
*Elastic
 7e+10,0.
*Material, name=COPPER
*Density
8790.,
*Elastic, type=SHEAR
 4.5e+10,
*Eos, type=USUP
```

```
3933.,  1.5, 1.99
*Plastic, hardening=JOHNSON COOK
 9.2e+07, 2.92e+08,     0.31,    0.025,       0.,       0.
*Material, name=TRELOAR
*Density
1000.,
*Hyperelastic, ogden, test data input
*Biaxial Test Data
      92057., 0.02
     155979., 0.06
     236293., 0.11
     257218., 0.14
     326084.,  0.2
     434367., 0.31
     508452., 0.42
     647695., 0.68
     763159., 0.94
     959977., 1.49
  1.2395e+06, 2.03
 1.44015e+06, 2.43
 1.70694e+06, 2.75
 1.97238e+06, 3.07
 2.20236e+06, 3.26
 2.41846e+06, 3.45
*Planar Test Data
      58860.,  0.069
     156960., 0.1034
     235440., 0.1724
     329616., 0.2828
     412020., 0.4276
     588600., 0.8483
```

```
    765180., 1.3862
    941760.,     2.
1.09087e+06, 2.4897
1.27138e+06, 3.0345
1.45973e+06, 3.4483
 1.6265e+06, 3.7793
1.78542e+06, 4.0621
*Uniaxial Test Data
    152114., 0.1338
    239040., 0.2675
    304238., 0.3567
    412893., 0.6242
    521549., 0.8917
    586736., 1.1592
    673663., 1.4268
    869244.,  2.051
1.04309e+06,  2.586
1.21694e+06, 3.0318
1.58637e+06, 3.7898
1.95579e+06, 4.3694
2.30349e+06, 4.8153
2.69465e+06,  5.172
3.04235e+06, 5.4395
3.39004e+06,  5.707
3.75947e+06, 5.9299
4.12889e+06, 6.0637
4.47659e+06, 6.1975
4.84601e+06, 6.3312
5.21545e+06,  6.465
5.58487e+06, 6.5541
6.30199e+06, 6.6433
```

```
*Volumetric Test Data
   5.886e+06, 0.9703
 1.15954e+07, 0.9412
 1.71871e+07, 0.9127
 2.26709e+07, 0.8847
**
** INTERACTION PROPERTIES
**
*Surface Interaction, name=CONTACT
*Friction
0.,
*Surface Behavior, pressure-overclosure=HARD
**
** BOUNDARY CONDITIONS
**
** Name: Pinned Type: Symmetry/Antisymmetry/Encastre
*Boundary
TRASN_END, ENCASTRE
**
** PREDEFINED FIELDS
**
** Name: Velocity   Type: Velocity
*Initial Conditions, type=VELOCITY
STRIKER-1.PART, 1, 0.
STRIKER-1.PART, 2, 0.
STRIKER-1.PART, 3, 10.
** ----------------------------------------------------------------
**
** STEP: Step-1
**
*Step, name=Step-1, nlgeom=YES
```

```
*Dynamic, Explicit
, 0.005
*Bulk Viscosity
1.5, 1.
**
** BOUNDARY CONDITIONS
**
** Name: Limit_X Type: Symmetry/Antisymmetry/Encastre
*Boundary
ASSEMBLY, XSYMM
** Name: Limit_Y Type: Symmetry/Antisymmetry/Encastre
*Boundary
ASSEMBLY, YSYMM
**
** INTERACTIONS
**
** Interaction: ST_IN-1
*Contact Pair, interaction=CONTACT, mechanical constraint=PENALTY, cpset=ST_IN-1
ST_PS, IN_PS
** Interaction: ST_TR
*Contact Pair, interaction=CONTACT, mechanical constraint=PENALTY, cpset=ST_TR
IN_SP, TR_SP
**
** OUTPUT REQUESTS
**
*Restart, write, number interval=1, time marks=NO
**
** FIELD OUTPUT: F-Output-1
**
```

```
*Output, field, number interval=1000, time marks=YES
*Node Output
AT, U, V
*Element Output, directions=YES
E, ER, LE, MISESONLY, NE, S
**
** HISTORY OUTPUT: INCI_750
**
*Output, history, time interval=5e-06
*Element Output, elset=INCI_750
ER33, ERV, LE33, NE33, S33
**
** HISTORY OUTPUT: TRANS_450
**
*Element Output, elset=TRANS_450
LE33, NE33, S33
*End Step
```